

NUMERICAL INVESTIGATIONS OF THE BLADE-TIP VORTEX OF A ROTOR WITH AXIAL INFLOW

Von der Fakultät für Maschinenbau
der Gottfried Wilhelm Leibniz Universität Hannover
zur Erlangung des akademischen Grades
Doktor-Ingenieur
genehmigte Dissertation

von
Andreas Thabo Goerttler, M.Sc.
geboren am 25.08.1989
in Heidelberg

2020

1. Referent: Prof. Dr.-Ing. Markus Raffel
2. Referent: Prof. Giuseppe Gibertini

Tag der Promotion: 7. Februar 2020

Abstract

Numerical computations using DLR's finite-volume compressible-flow solver TAU are conducted to investigate the tip vortex of a helicopter blade. The computations comprise unsteady Reynolds-averaged Navier-Stokes (URANS) simulations and detached-eddy simulations (DES).

In all computations, a rotor with a radius of $R = 0.65$ m is simulated with a constant flow perpendicular to the rotor axis. The chord length $c = 0.072$ m of the DSA-9A airfoil leads to a Mach number of $M_{\text{tip}} = 0.28$ and a Reynolds number of $Re_{\text{tip}} = 470\,000$ at the tip. Both two-bladed and four-bladed configurations under various constant and sinusoidal pitch conditions are examined. In the expected path of the blade-tip vortex, a fine resolution of a hexahedral block is implemented to reduce numerical dissipation. The URANS simulations using the shear-stress transport (SST) turbulence model on the two-bladed configuration demonstrate good prediction regarding the generation and early development of the blade-tip vortex. The numerical dissipation, however, inhibits realistic results at more advanced wake ages. Therefore, a zonal approach with a large-eddy simulations (LES) model is employed on the four-bladed configuration to reduce numerical dissipation and to improve physical modeling of the vortex development.

Algorithms deriving the vortex position, shape, swirl velocity, circulation, and core radius are implemented. The analysis shows that the position of the rotor-blade trailing-edge mainly drives the vertical location of the vortex core. Furthermore, the high cyclic pitch case predicts a strong hysteresis between up- and downstroke and a very elliptic vortex core. This elliptical vortex shape rotates with approximately half the solid-body rotation speed of the core. The vortex of the attached pitching case can be modeled as an assembly of the static vortex states. Additionally, the vorticity in the vortex is well predicted by the maximum circulation on the blade.

The simulations are validated by wind tunnel experiments featuring a complete pitching cycle at the rotor test facility in Göttingen (RTG). Thrust trimmed comparisons show a qualitative and quantitative agreement in the swirl velocity.

Key words: blade-tip vortex, rotor, numerical simulations

Kurzfassung

Numerische Untersuchungen des Blattspitzenwirbels an einem Rotor mit axialer Zuströmung

In dieser Arbeit werden numerische Simulationen mit dem Finite-Volumen Löser TAU des DLR durchgeführt um den Blattspitzenwirbel eines Hubschrauberblattes zu untersuchen. Dabei werden *unsteady Reynolds-averaged Navier-Stokes* (URANS)-Simulationen und *detached eddy-simulations* (DES) verwendet.

Die Simulationen eines Rotors mit einem Radius von $R = 0.65$ m werden mit einer konstanten, senkrecht auf der Rotorachse stehenden Anströmung durchgeführt. Die Blatattiefe von $c = 0.072$ m des DSA-9A Profils führt zu einer Machzahl von $M_{\text{tip}} = 0.28$ und einer Reynoldszahl von $Re_{\text{tip}} = 470\,000$ an der Blattspitze. Sowohl eine Zweiblatt- als auch eine Vierblatt-Konfiguration werden unter bestimmten konstanten und sinusförmigen Nickbedingungen untersucht. Im erwarteten Bereich des Blattspitzenwirbels ist ein feiner aufgelöster strukturierter Block eingesetzt, um die numerische Dissipation zu reduzieren. Die URANS Simulationen, die das *shear-stress transport* (SST) Turbulenzmodell verwenden, zeigen bei der Zweiblatt-Konfiguration gute Vorhersagen der Entstehung und frühen Entwicklung des Blattspitzenwirbels auf. Jedoch verhindert numerische Dissipation realistische Ergebnisse bei älteren Wirbeln. Eine zonale Betrachtungsweise mit einem *large-eddy simulations* (LES) Modell bei der Vierblatt-Konfiguration hingegen reduziert die numerische Dissipation und verbessert die physikalische Modellbildung der Wirbelentstehung.

Algorithmen, welche die Position, die Tangentialgeschwindigkeit, die Zirkulation und den Kernradius des Blattspitzenwirbels extrahieren, werden implementiert. Dabei zeigt sich, dass die vertikale Position des Wirbelkerns hauptsächlich von der Position der Rotorblatthinterkante abhängt. Eine starke Hysterese tritt bei hohen Nickschwingungen zwischen Auf- und Abnicken auf. Die elliptische Gestalt des Wirbels rotiert ungefähr mit der halben Starrkörperbewegung des Kerns. Der instationäre Wirbel kann mit stationären Ergebnissen angenähert werden und die Vortizität des Wirbels wird gut von der maximalen Zirkulation auf dem Blatt vorhergesagt.

Die Simulationen werden mit existierenden Daten aus Windkanalexperimenten

am Rotorteststand in Göttingen (RTG) validiert. Diese Daten beinhalten einen kompletten Nickzyklus. Schub-getrimmte Vergleiche zeigen sowohl eine qualitative als auch eine quantitative Übereinstimmung der Tangentialgeschwindigkeit.

Stichwörter: Blattspitzenwirbel, Rotor, Numerische Simulationen

Publications

Following articles have already been published in journals and conference proceedings within the scope of this work:

1. K. Richter, S. Koch, A. Goerttler, B. Lütke, C.C. Wolf, and A. Benkel, "Unsteady Boundary Layer Transition on the DSA-9A Rotor Blade Airfoil", 41st European Rotorcraft Forum, Munich, Germany, 1–4 Sept., 2015.
2. C.C. Wolf, A.D. Gardner, A. Goerttler, and K. Richter "Instationäre Transitionsmessung mit neuartigen Messmethoden, [Engl: Unsteady Transition Measurement with New Measurement Techniques]", Deutscher Luft- und Raumfahrtkongress, Braunschweig, 13-15 September, 2016.
3. A. Goerttler, A. D. Gardner, and K. Richter, "Unsteady Boundary Layer Transition Detection by Automated Analysis of Hot Film Data", STAB 2016, Braunschweig, 8-9 Nov., 2016.
4. A. Goerttler, A. D. Gardner, and K. Richter, "Unsteady Boundary Layer Transition Detection by Automated Analysis of Hot Film Data", in: New Results in Numerical and Experimental Fluid Mechanics XI, Notes on Numerical Fluid Mechanics and Multidisciplinary Design 136, Springer International Publishing, 2018, pp. 387–396, DOI: [10.1007/978-3-319-64519-3_35](https://doi.org/10.1007/978-3-319-64519-3_35)
5. A. Goerttler, J. N. Braukmann, T. Schwermer, A. D. Gardner, and M. Raffel, "Tip-Vortex Investigation on a Rotating and Pitching Rotor Blade", 43rd European Rotorcraft Forum, Milan, Italy, 12–15 Sept., 2017.
6. A. Goerttler, J. N. Braukmann, T. Schwermer, A. D. Gardner, and M. Raffel, "Tip-Vortex Investigation on a Rotating and Pitching Rotor Blade", *Journal of Aircraft*, Vol. 55, No. 5, 2018, pp. 1792-1804, DOI: [10.2514/1.C034693](https://doi.org/10.2514/1.C034693)

7. J. N. Braukmann, A. Goerttler, C. C. Wolf, and M. Raffel, "Blade-Tip Vortex Characterization of a Rotor Under Static and Cyclic Pitch Conditions Using BOS and PIV", *57th AIAA Aerospace Sciences Meeting*, San Diego, California, Italy, 7–11 Jan. 2019.
8. A. Goerttler, J. N. Braukmann, C. C. Wolf, A. D. Gardner, and M. Raffel, "Blade Tip-Vortices of a Four-Bladed Rotor in Hover and Unsteady Conditions", *VFS 75th Annual Forum*, Philadelphia, Pennsylvania, 13–16 May, 2019.

Acknowledgments

I would like to thank my doctoral advisor Prof. Dr.-Ing. Markus Raffel for giving me the opportunity to be part of the research community, for a productive environment with the possibility to develop own ideas, and for the numerous feedback in the course of this dissertation. I also want to thank Prof. Giuseppe Gibertini from the University of Milano and Prof. Dr.-Ing. Gerhard Poll from the Gottfried Wilhelm Leibniz University Hannover for their commitment as members of my dissertation committee.

Special thanks goes to Tony Gardner for all his technical advice in numerous short and long meetings, for challenging my ideas, for giving me new inputs, and for putting me back on track when needed. Thank you for all the support in the past years. Many thanks also to Kai Richter for mentoring me with his outside perspective and fresh input on my work.

Also, I would like to thank my colleagues of the helicopter group: Christian Wolf, Till Schwermer, Kurt Kaufmann, Armin Weiss, Johannes Braukmann, Clemens Schwarz, and Felix Wienke. The private and work related discussions helped to focus on the important parts of work and life. Furthermore, I would like to thank Christian Schnepf and Patrice Touré, who shared their ideas during lunch breaks.

Additionally, I am very thankful towards the DLR project FAST-Rescue for funding this work. I gratefully acknowledge the Gauss Centre for Supercomputing e.V. (GCS, www.gauss-centre.eu) for providing computing time on the GCS Supercomputer SuperMUC at Leibniz Supercomputing Centre (LRZ, www.lrz.de) under project pr53fi.

Also, I want to thank all medical staff who reestablished my health and ability to accomplish this work. Finally, special thanks goes to my family for raising me to the person I am today, and for all their support in difficult times. Thank you Stephan for your great proofreading. The biggest thanks goes to my girlfriend Simone. Your contagious enthusiasm helped me to finish this dissertation.

Contents

	Page
Contents	xi
List of Figures	xiii
List of Tables	xvii
Nomenclature	xix
1 Introduction	1
2 State of the art - Blade-tip vortices	5
2.1 Vortex theory	5
2.2 Vortex models	8
2.3 Blade-tip vortices of a helicopter rotor	14
2.4 Finite wing investigations	17
2.5 Oscillating wing investigations	19
2.6 Rotating blade investigations	21
2.7 Scope of this work	27
3 Tools and methods	31
3.1 Finite-volume solver	31
3.2 Experimental setup	33
3.3 Coordinate systems	38
3.4 Vortex analysis	39
3.5 Error analysis	43

4	Blade-tip vortices of a two-bladed rotor	47
4.1	Numerical setup of the two-bladed rotor	47
4.2	Grid and time-step sensitivity	49
4.3	Load characteristics	51
4.4	General aspects of blade-tip vortices	51
4.5	Circulation	53
4.6	Radius	56
4.7	Azimuthal analysis of the vortex core	58
4.8	Position	60
4.9	Pressure inside the vortex core	63
4.10	Effect of rotation	65
5	Blade-tip vortices of a four-bladed rotor	67
5.1	Numerical setup of the four-bladed rotor	67
5.2	Thrust polar of static cases	72
5.3	Effect of DES compared to URANS	75
5.4	Vortex generation	79
5.5	Vortex propagation	82
5.6	Vortex-core position	83
5.7	Unsteady vortex	84
5.8	Variation of the Reynolds number	90
6	Conclusion	93
	References	97
	Curriculum Vitae	109

List of Figures

Figure 1.1: Isosurface of λ_2 highlights the vortex system of an unsteady pitching motion $\Theta_r = 24^\circ \pm 6^\circ$	2
Figure 2.1: Streamtraces over a wing tip.	6
Figure 2.2: Generic circulation distribution over a finite wing.	7
Figure 2.3: Generic swirl velocity and circulation of a blade-tip vortex. . .	8
Figure 2.4: Generic swirl-velocity profiles for different vortex models of a blade-tip vortex.	9
Figure 2.5: Generic swirl-velocity profiles for different vortex models of a blade-tip vortex (arrows depict increase in β and Re_v).	11
Figure 2.6: Generic circulation and frequency profiles for different vortex models of a blade-tip vortex.	12
Figure 2.7: Visualization of a fully developed blade-tip vortex with three zones from Ramasamy et al. [79].	13
Figure 2.8: Velocity vectors on a blade in hover and in forward flight ($\mu = 0.2$).	14
Figure 2.9: Typical flow phenomena during forward flight, from Leishman & Bagai [57].	16
Figure 2.10: Generic circulation distribution over a rotating blade.	16
Figure 2.11: Initial roll-up of a wing-tip vortex from Chow et al. [22].	18
Figure 2.12: Plan view of the Ω -shaped dynamic stall vortex from Spentzos et al. [101].	19
Figure 2.13: DES (left) and URANS (right) λ_2 isosurfaces around NACA0015 from Mohamed et al. [68].	20
Figure 2.14: Instantaneous axial velocity fields of a tip vortex from Wolf et al. [118].	21
Figure 2.15: Sketch of helical vortex pattern of a single-bladed hovering helicopter from Gray [34].	22
Figure 2.16: Visualization of blade-tip vortices from Leishman & Bagai [57].	24

Figure 2.17: Laser sheets in the 40- by 80-foot wind tunnel from Yamauchi et al. [119].	25
Figure 2.18: Visualization of Q isosurfaces from Potsdam & Jayaraman [74].	26
Figure 2.19: Radial lift distribution on the blade for different pitch angles during the upstroke motion for two and four-bladed configuration with similar thrust.	28
Figure 3.1: Overview of the RTG.	34
Figure 3.2: The RTG at the DLR in Göttingen (adapted from Schwermer et al. [91]).	35
Figure 3.3: DSA-9A airfoil with experimental sensor positions.	35
Figure 3.4: Schematic sketch of the rotor-blade geometry.	36
Figure 3.5: Twist distribution of the rotor blade.	37
Figure 3.6: PIV planes at the RTG at the DLR in Göttingen.	37
Figure 3.7: Coordinate systems employed in this study.	38
Figure 3.8: Example slices for vortex analysis.	40
Figure 3.9: Visualization of different vortex analysis methods.	42
Figure 3.10: Extracted vortex core with two different center positions. . . .	43
Figure 3.11: Influence of offset in center position on radius.	44
Figure 3.12: Resulting error of swirl velocity due to wrong center position.	45
Figure 3.13: Azimuthal variation of swirl velocity ($\Theta_r = 24^\circ$; $\Psi_V = 10^\circ$). . .	46
Figure 3.14: Discrepancy due to two orthogonal cuts (— = maximum; --- = minimum)	46
Figure 4.1: Planform of the rotor blade.	48
Figure 4.2: Numerical grid of the two-bladed rotor.	48
Figure 4.3: Swirl velocity of the blade-tip vortex at $\Psi_V = 2.6^\circ$ ($x/c = 0.39$) behind the blade for different grids, $\Theta_r = 29.55^\circ$	50
Figure 4.4: Thrust coefficient of CFD simulations with different temporal resolution.	50
Figure 4.5: Dimensionless coefficients at $r/R = 0.77$	51
Figure 4.6: Isosurfaces of λ_2 criterion, colored with rotationwise vorticity. .	52
Figure 4.7: Slices at the blade tip, colored with rotationwise vorticity. . . .	52
Figure 4.8: Circulation of the blade-tip vortex at $\Psi_V = 2.6^\circ$ ($x/c = 0.39$) behind the blade for CFD simulation and experiment [15], $\Theta_r = 29.55^\circ$	53
Figure 4.9: Circulation of CFD simulation at constant radial distance $r_v = 0.2c$ for different wake ages.	54

Figure 4.10: Comparison between tip vortex circulation and lift coefficient at $r/R = 0.77$ of CFD simulation.	55
Figure 4.11: Circulation of the experiment [15] and CFD simulation at two different radial stations for $\Psi_V = 2.6^\circ$	56
Figure 4.12: Vortex radius for experiment [15] and CFD simulation at two different wake ages.	56
Figure 4.13: Vortex radius for experiment [15] and CFD simulation with a DES approach at two different wake ages.	57
Figure 4.14: Vortex core shape of CFD simulation for several time instants during upstroke at $\Psi_V = 2.6^\circ$	58
Figure 4.15: Parameters of the ellipse fitted to the vortex core of CFD simulation.	59
Figure 4.16: Position of the vortex core of CFD throughout a full cycle. . . .	61
Figure 4.17: Vortex behavior of CFD simulation at different wake ages and time instants during upstroke motion visualized by λ_2 criterion. . . .	62
Figure 4.18: Pressure of CFD simulation inside the vortex tube over the period.	63
Figure 4.19: Pressure of CFD simulation inside the vortex tube over a complete period at several constant wake ages.	64
Figure 4.20: Axial velocity of CFD simulation inside the vortex tube over a complete period at several constant wake ages.	65
Figure 4.21: Circulation of experiment [15] and CFD simulations, nonrotational data after Kaufmann et al. [47], $\Psi_V = 2.6^\circ (x/c = 0.41)$. . .	66
Figure 5.1: Visualization of examined cases.	68
Figure 5.2: Cuts displaying hexahedral cells at $y/R = 0.9$ and $z/c = 0$	69
Figure 5.3: Numerical grid of the four-bladed rotor.	70
Figure 5.4: Density residual of different parameter settings.	71
Figure 5.5: Thrust coefficient of experiment and CFD simulations.	72
Figure 5.6: Phase-averaged downwash velocity against the radial position in two planes close to the rotor.	73
Figure 5.7: Close up view on the blade-tip vortex for five different static cases.	74
Figure 5.8: Normalized swirl velocity of blade-tip vortex over radial distance for different constant pitch angles at $\Psi_V = 15^\circ$	75
Figure 5.9: Normalized swirl velocity of blade-tip vortex over radial distance with different settings.	76

Figure 5.10: Normalized swirl velocity of blade-tip vortex over radial distance for different constant pitch angles at $\Psi_V = 20^\circ$	77
Figure 5.11: Normalized swirl velocity of the blade-tip vortex over radial distance for five different constant pitch angles at $\Psi_V = 20^\circ$ and two fits after Vatisstas et al. [111].	78
Figure 5.12: Normalized circulation of blade-tip vortex over radial distance for different constant pitch angles at $\Psi_V = 20^\circ$	78
Figure 5.13: Normalized radius of blade-tip vortex for different constant pitch angles over the wake age.	79
Figure 5.14: Radial circulation distribution on the blade for different constant pitch angles.	80
Figure 5.15: Ratio of tip vortex circulation $\Gamma_{0.5c}$ and maximum circulation on the blade Γ_{\max} for different constant pitch angles over the wake age.	81
Figure 5.16: Normalized swirl velocity and normalized circulation of blade-tip vortex over radial distance ($\Theta_r = 24^\circ$, $\Psi_V = 15^\circ$).	81
Figure 5.17: Ratio of the axes of the ellipse of the vortex core for different angles of incidence.	82
Figure 5.18: Position angle of ellipse.	83
Figure 5.19: Vertical and horizontal position of the blade-tip vortex for different angles of incidence over the wake age (Static and unsteady cases).	84
Figure 5.20: Close up view of the blade-tip vortex for eight different cases during an unsteady pitch motion.	85
Figure 5.21: Blade circulation throughout a complete period.	86
Figure 5.22: Vertical position of blade-tip vortex against wake age.	87
Figure 5.23: Vertical (a), horizontal (b) position, normalized circulation (c) and radius (d) of unsteady blade-tip vortex against wake age.	88
Figure 5.24: Normalized swirl velocity of blade-tip vortex over radial distance for different angles of incidence at $\Psi_V = 40^\circ$	89
Figure 5.25: Normalized axial velocity inside the blade-tip vortex for different instants of time in the pitching cycle over the wake age.	89
Figure 5.26: Normalized radius of blade-tip vortex throughout an entire pitching cycle for two wake ages.	90
Figure 5.27: Normalized circulation and radius of blade-tip vortex for different instants of time in the pitching cycle over the wake age.	91

List of Tables

Table 2.1:	Coefficients for analytical vortex model after Ramasamy & Leishman [81].	11
Table 2.2:	Root angle Θ_r of investigated CFD cases.	28
Table 3.1:	Parameters of experiment and simulation.	36
Table 3.2:	Conversion of vortex age.	39
Table 4.1:	Parameters of the background grid.	49
Table 5.1:	Residual values of different cases.	71
Table 5.2:	Fitting factor β for static cases with different weighting parameters.	77

Nomenclature

Latin symbols

a, b	(m)	Major and minor axis of an ellipse
a_n, b_n	(-)	Coefficients for analytical vortex model
c	(m)	Blade chord length ($c = 0.072$ m)
c_l	(-)	Local lift coefficient
c_t	(-)	Local thrust coefficient
C_T	(-)	Blade thrust coefficient ($C_T = F_z/(\rho_\infty(\Omega R)^2\pi R^2)$)
c_m	(-)	Local pitching moment coefficient
\hat{d}	(-)	Equivalent downstream distance ($\hat{d} = \Psi\Gamma_v/\Omega c^2$)
ds	(m)	Line integral
f	(Hz)	Frequency
F_z	(N)	Thrust in z -coordinate
i	(°)	Inclination of an ellipse
k	(-)	Turbulent kinetic energy
L'	(N/m)	Lift per unit length of span
M	(-)	Mach number
n	(-)	Vatistas swirl shape parameter
N_{inner}	(-)	Total number of inner iterations
N_{iter}	(-)	Inner iterations
N_Ψ	(-)	Number of time steps per period
Q	(-)	Ratio between $\Gamma_{0.2c}$ and $c_t M^2$ ($Q = \Gamma_{0.2c}/c_t M^2 \cdot c_t M^2(\Theta_{\min})/\Gamma_{0.2c}(\Theta_{\min})$)
r	(m)	Radial distance
\bar{r}	(-)	Normalized radial distance ($\bar{r} = r/r_c$)
r_c	(m)	Vortex core radius
\bar{r}_c	(-)	Normalized vortex core size ($\bar{r}_c = r_c/c$)
r_v	(m)	Vortex coordinate in radial direction
\bar{r}_v	(-)	Normalized radial distance ($\bar{r}_v = r_v/c$)

R	(m)	Rotor blade radius ($R = 0.65$ m)
Re	(-)	Reynolds number based on chord
Re_v	(-)	Vortex Reynolds number ($Re_v = \Gamma_v/\nu$)
$R_{\rho, \text{start}}$	(-)	Density-residual at the start of a time step
$R_{\rho, \text{end}}$	(-)	Density-residual at the end of a time step
s	(m)	Edge length of cells
t	(s)	Time
T	(s)	Period time
u_p	(m/s)	Axial velocity along x_p
U	(m/s)	Velocity
v	(m/s)	Flight velocity
v_r	(m/s)	Radial velocity
v_ϕ	(m/s)	Swirl Velocity
\bar{v}_ϕ	(-)	Normalized swirl velocity ($\bar{v}_\phi = v_\phi/U_{\text{tip}}$)
\hat{v}_ϕ	(-)	Equivalent swirl velocity ($\hat{v}_\phi = v_\phi c/\Gamma_v$)
w	(-)	Weighting parameter
x	(m)	Curved distance between measurement position and blade tip trailing edge
x_p	(m)	PIV plane coordinate in axial direction
y^+	(-)	Dimensionless wall distance
y_p	(m)	PIV plane coordinate in outboard direction
z	(m)	Coordinate in downward direction
z_p	(m)	PIV plane coordinate in downward direction

Greek symbols

α_L	(-)	Lamb's constant ($\alpha_L = 1.256$)
β	(-)	Vatistas turbulence parameter
Γ	(m^2/s)	Circulation
Γ_0	(m^2/s)	Total circulation
Γ_v	(m^2/s)	Circulation of the vortex
$\bar{\Gamma}$	(-)	Normalized circulation ($\bar{\Gamma} = \Gamma/(c \cdot U_{\text{tip}})$)
δ	(-)	Partial derivative
Δ	(-)	Difference
Δb	(-)	Order of magnitude drop of density-residual
ϵ	(-)	Dissipation rate of K

η	(-)	Kolmogorov length scale
Θ_r	(°)	Blade pitch angle at the root
λ_2	(1/s)	λ_2 vortex criterion
μ	(-)	Advance ratio ($\mu = v/U_{\text{tip}}$)
ν	(-)	Kinematic viscosity
ν_t	(-)	Eddy viscosity
ρ_∞	(kg/m ³)	Free stream flow density
σ	(-)	Solidity
ϕ_v	(°)	Vortex coordinate in azimuthal direction
Ψ	(°)	Azimuth angle
Ψ_V	(°)	Vortex age
ω	(1/s)	Turbulence frequency
$\omega_{x,p}$	(1/s)	Vorticity perpendicular to wake plane
Ω	(Hz)	Rotational speed ($\Omega = 23.6$ Hz)

Subscripts

\uparrow	During upstroke motion
\downarrow	During downstroke motion
$0.2c$	At $r_v = 0.2c$
$0.5c$	At $r_v = 0.5c$
707	Condition at radial distance $r/R = \sqrt{2}/2$
core	Edge of vortex core
max	Maximal value
min	Minimal value
TTE	Blade-tip trailing-edge
tip	Condition at the tip of the blade
∞	Farfield condition

Abbreviations

2C	two-component
2D	two-dimensional
3C	three-component
AHS	American Helicopter Society (1943-2018), now VFS
AIAA	American Institute of Aeronautics and Astronautics
BOS	Background Oriented Schlieren
BVI	Blade vortex interaction
CENTAUR TM	Grid Generator
CFD	Computational Fluid Dynamics
DDES	Delayed Detached-Eddy Simulation
DES	Detached-Eddy Simulation
DLR	German Aerospace Center e.V.
DNS	Direct Numerical Simulation
DSA-9A	Airfoil profile with 9% thickness
ERF	European Rotorcraft Forum
HART-2	HHC Aeroacoustic Rotor Test-2
HHC	Higher Harmonic Pitch Control
HELIOS	Helicopter Overset Simulations Tool
LES	Large-Eddy Simulation
NACA	National Advisory Committee for Aeronautics
LDV	Laser Doppler Velocimetry
LD2	Low-Dissipation Low-Dispersion
PIV	Particle Image Velocimetry
RANS	Reynolds-Averaged Navier-Stokes
RSM	Reynolds-Stress Model
RTG	Rotor Test Facility Göttingen
SGS	Sub-grid Scale Model
SPP8	Blade-tip shape
SST	Shear-Stress Transport
TAU	DLR's Finite-Volume Solver
UH-60A	Four-bladed helicopter by Sikorsky Aircraft
URANS	Unsteady Reynolds-Averaged Navier-Stokes
VC	Vortex Center
VFS	Vertical Flight Society (up to 2018: AHS)

1 Introduction

Blade-tip vortices are still a challenging flow phenomenon in helicopter aerodynamics since they induce drag and, thus, influence the performance of the rotor. Furthermore, they strongly affect the wake of the helicopter and result in a complex vortex form due to the rapidly varying lift with time. These vortices arise due to pressure differences between the lower and upper surfaces, driving the flow around the tip from the pressure side to the suction side. Depending on the shape of the tip, several vortices can arise. Blade-tip vortices occur both in fixed-wing aerodynamics and helicopter aerodynamics. However, fixed-wing aircraft leave their blade-tip vortices behind, whereas helicopters re-ingest the blade-tip vortices in multiple flight conditions, resulting in blade-vortex interaction (BVI). These interactions, in turn, result in a limitation of the flight envelope of the helicopter due to dynamic stall on the highly loaded rotor.

Additionally, the vortices can strike the tail or be ingested by the tail rotor. The rapidly changing velocity in the vortex leads to high impulsive loads on the structure and, thus, an increase in vibration. Moreover, all interactions between vortices and structures generate impulsive aeroacoustic noise. This noise impact of helicopters on areas surrounding flight paths and landing platforms is relevant as it influences the social acceptance of helicopter operations. Therefore, the understanding how blade-tip vortices are generated and propagated is of great interest.

The vortex roll-up is a challenging numerical problem due to a tendency toward unphysical dissipation if the computation is under-resolved or uses particular numerical models. Therefore, the vortex roll-up and changes in swirling strength and core radius are important calibration parameters for computational fluid dynamics (CFD) codes attempting to reproduce vortex interactions.

Thus, four questions arise from the numerical and aerodynamic point of view:

Is the vorticity that is required by the lift distribution correctly transported to the vortex?

Are convection and decay of the mature vortex correct?

How does the blade loading relate to the vortex strength?

How do the time-varying vortices of a pitching blade compare with the constant vortices of a hovering blade?

The first two questions are related to the prediction capability of the code through experimental validation, whereas the last two questions focus on the aerodynamic and physical behavior of the blade-tip vortices.

This study analyzes the blade-tip vortex of a rotor at high cyclic pitch. In contrast with earlier investigations, the rotor test facility in Göttingen (RTG) is capable of a very fine particle image velocimetry (PIV) scan of the blade-tip vortex. This scan allows a direct comparison of experiment and numerical simulations concerning the evolution of the vortex. Previously, this comparison could only be made at a single azimuthal point. The focus of this study is a thorough numerical investigation of the evolution and convection of the blade-tip vortex complete with a comparison to experimental results by Wolf et al. [117] and Braukmann et al. [14].

Figure 1.1 shows a visualization of the numerical simulations for the pitching cycle ($\Theta_r = 24^\circ \pm 6^\circ$). The highest angle of incidence at the root of $\Theta_r = 30^\circ$ is reached in the upper left corner. For simplicity, only vortices up to a wake age of $\Psi_V = 90^\circ$ are displayed. A variation in both the blade flow and the generated vortex structures can be seen.

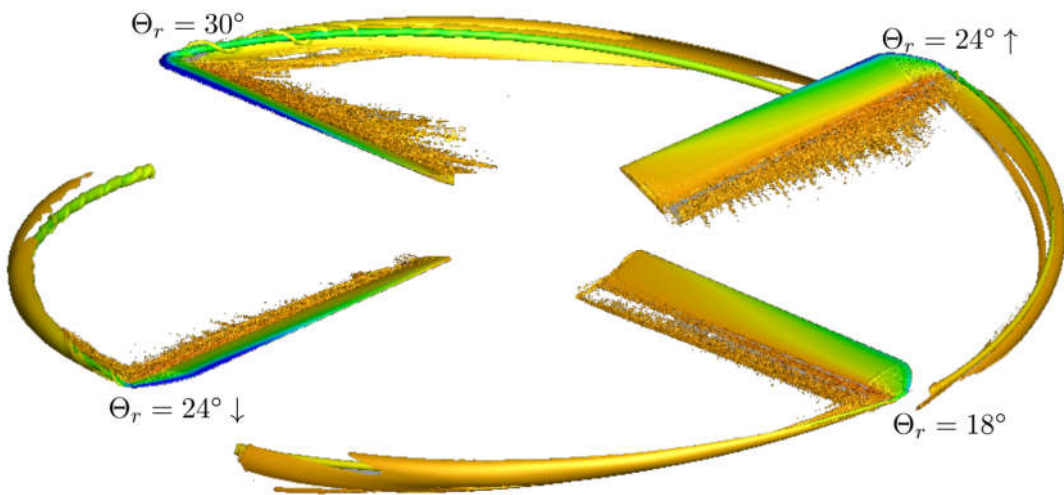


Figure 1.1: Isosurface of λ_2 highlights the vortex system of an unsteady pitching motion $\Theta_r = 24^\circ \pm 6^\circ$.

Overview

The subsequent chapters of this thesis are organized as follows: The upcoming chapter covers the theory, models, and prior investigations of vortices, followed by a description of the applied tools and methods in chapter 3. It contains the numerical solver, the experimental setup, the implemented algorithms, and an error estimate. After that, the main chapters 4 and 5 describe the numerical analysis of a two-bladed and a four-bladed rotor, respectively. Among other parameters, this analysis includes position, shape, swirl-velocity, and circulation distribution of the vortex core. In addition to these results, a grid, a time step, and a convergence study are described. Comparisons to experimental results complement these investigations. The last chapter of this thesis gives a summarized conclusion.

2 State of the art - Blade-tip vortices

This chapter presents the theory of a vortex, analytical vortex models, and in particular blade-tip vortices of a helicopter rotor. Additionally, the most relevant experimental and numerical works in the field of blade-tip vortices of finite and oscillating wings are presented. The last section then highlights some of the main contributions regarding experimental and numerical rotor investigations.

2.1 Vortex theory

A vortex is a rotating movement of fluid elements around an arbitrary line in three-dimensional space. The fluid elements do not need to rotate around themselves. In contrast to the simplicity of this intuitive description, a rigorous mathematical definition is challenging.

Already in the middle of the 19th century, Stokes [104] and Helmholtz [38] performed mathematically motivated research on viscosity. Helmholtz published his findings being unaware of the earlier work of Stokes; see [105]. The study on the vortex-filaments led to the well-known Helmholtz's theorems [38]:

- The strength of a vortex tube remains constant along its length.
- Vortex tubes form either a closed path or extend to boundaries since they cannot end in a fluid.
- Only external rotational forces can produce vorticity.

The order of the theorems is not uniform in the literature. As an example, the theorems can explain the stability of smoke rings. Helmholtz postulated these theorems for inviscid flows, but they are still valid to some extent for viscous flows, where viscous effects result in dissipation of enstrophy and diffusion of vorticity.

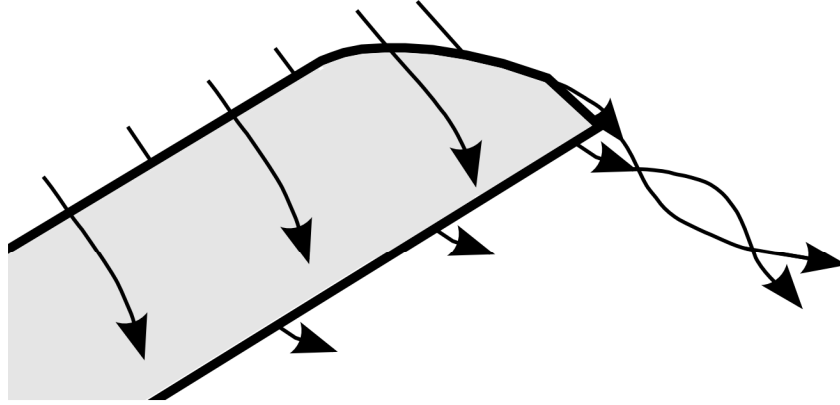


Figure 2.1: Streamtraces over a wing tip.

Wing-tip vortex

Figure 2.1 shows three-dimensional streamtraces over a wing tip. The driving force acting on an airfoil in a surrounding flow is the aerodynamic lift, which is perpendicular to the incoming flow. Lift emerges due to the pressure difference between the upper (suction) and the lower (pressure) side. In the case of a positively inclined structure, lower pressure emerges on the upper and higher pressure on the lower side. The airflow always tends to restore pressure equality, which means that the flow is driven towards lower pressure. On a finite end of every wing, the flow, therefore, curls from one side to the other side. As a result, the flow on the pressure side has a spanwise component towards the root. On the lower side, the streamlines bend towards the tip. These three-dimensional circular motions will eventually establish the formation of a trailing vortex. The vortex induces a downward component on the inboard of the surface, which reduces the effective angle of attack.

Lifting-line theory

Every slice of a wing or blade generates lift, depending on the chord length c , the geometric twist Θ , the angle of incidence, the density ρ_∞ , and the incoming flow velocity v . The lift per unit length of span L' then is:

$$L' = \rho_\infty / 2 v^2 c_l c \quad (2.1)$$

Consequently, the lift distribution differs in the radial direction. Due to the pressure equalization at the tips, the lift goes down to zero at all ends. In the early 20th century, Prandtl developed the classical lifting-line theory; see Anderson [3]. This

theory replaces the wings with a bound vortex and attaches perpendicular potential vortices at the ends in a “horseshoe vortex” system; see Fig. 2.2. The lift distribution is replaced by the circulation distribution, applying the Kutta-Joukowski theorem. This theorem links the circulation Γ with the lift per unit length of span L' ; see Betz [6]:

$$L' = \rho_{\infty} v \Gamma \quad (2.2)$$

Smaller vortices are added between the two outer vortices since the singularity of the potential vortices leads to unphysical downwash values. Instead of two single free vortices, a continuous vortex sheet is obtained. The vortex with all bound vorticity remains on the line of the wing. The strengths of the free vortices correspond to the change or gradient of the circulation distribution ($d\Gamma/dy$) on the wing.

The shape of the wing defines the lift distribution. An elliptical lift distribution is favorable, as it leads to the least possible amount of unwanted induced drag. Additionally, a constant downwash occurs. The theory of Prandtl further explains that the aspect ratio has a significant effect on the induced angle and drag. Wings with a higher aspect ratio have lower induced drag coefficients, as the effect of the ends diminishes with increasing aspect ratio. The favorable lift distribution can be achieved purely by a twisted blade or by an elliptical shape, which is hard to manufacture.

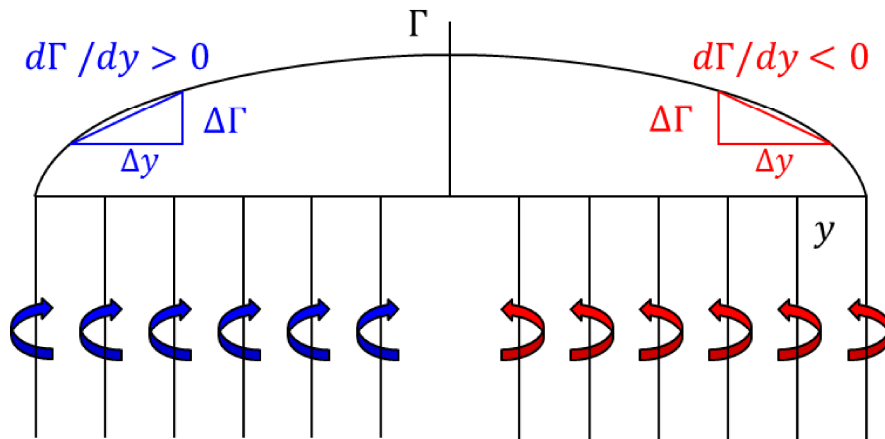


Figure 2.2: Generic circulation distribution over a finite wing.

The particular case of an elliptic, clean wing is illustrated in Fig. 2.2 by showing the circulation distribution. The circulation is zero on both ends. On the left-hand side, there is only a positive gradient ($d\Gamma/dy > 0$) with the maximum in the middle. The distribution is symmetrical, with a negative gradient ($d\Gamma/dy < 0$) occurring on the right-hand side. The change in circulation is transported away in the vortex sheet. The sign of the gradient determines the sense of rotation of the shed vortices.

2.2 Vortex models

Several vortex models have been established in the past. These mostly algebraic formulations model the swirl-velocity distribution of a trailing vortex. First, a generic distribution is discussed, followed by essential vortex models in the literature.

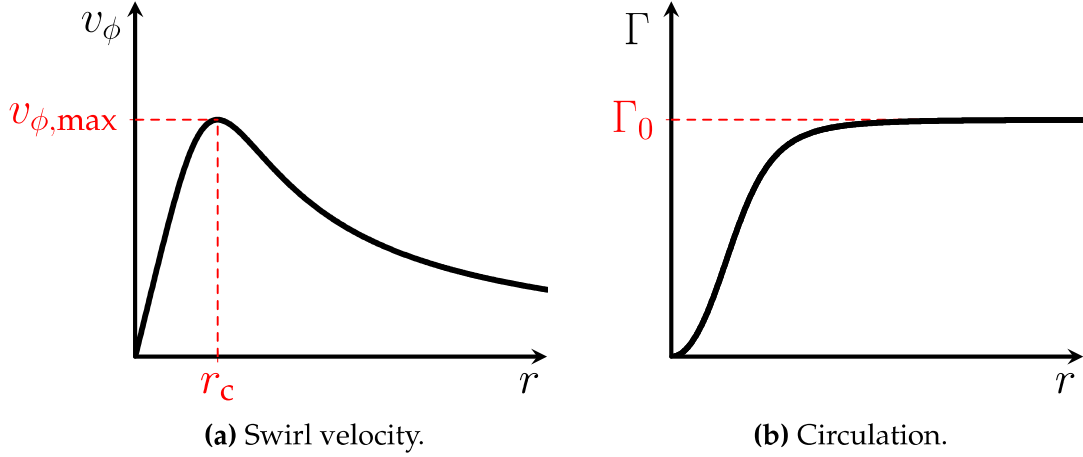


Figure 2.3: Generic swirl velocity and circulation of a blade-tip vortex.

Figure 2.3 shows the swirl velocity and circulation of a generic blade-tip vortex. There is an approximately linear growth of the swirl velocity towards the peak, which defines the vortex core. Outside this core, the swirl velocity decreases and asymptotically approaches zero. The circulation Γ , see equation (2.3), of the blade-tip vortex is proportional to the product of the swirl velocity v_ϕ and the radius r if rotational symmetry is assumed. The line integral ds via a closed curve of the velocity field v can then be simplified to:

$$\Gamma = \oint v ds = 2\pi v_\phi r. \quad (2.3)$$

Figure 2.3(b) shows the circulation distribution of a blade-tip vortex starting at zero in the center. Then the distribution steadily increases towards the total circulation Γ_0 .

The most straightforward model is the potential approach, which assumes a constant circulation and, therefore, an anti-proportional formulation of the swirl velocity. The resulting formula of the potential vortex model is:

$$v_\phi(\bar{r}) = \left(\frac{\Gamma_v}{2\pi r_c} \right) \frac{1}{\bar{r}}, \quad (2.4)$$

where $\bar{r} = r/r_c$ is the nondimensional radial distance normalized by the core radius r_c .

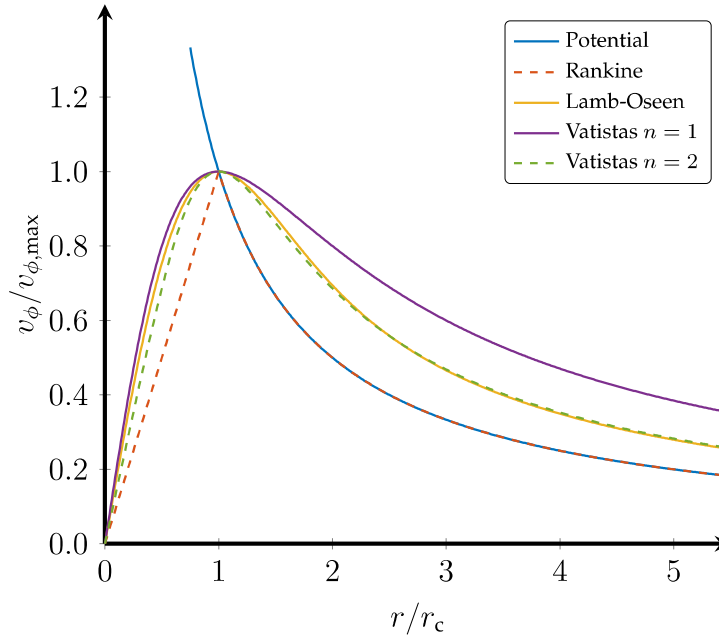


Figure 2.4: Generic swirl-velocity profiles for different vortex models of a blade-tip vortex.

The values of the nondimensionalized swirl velocity decrease on the outside of the vortex core, whereas infinite velocities occur at the vortex core, which can be seen in Fig. 2.4. An easy solution is named after Rankine [83], which separates the formulation in two regions. The inner part is replaced by a solid-body rotation, which is represented by a linear velocity increase. Outside of the vortex core, the potential regime remains. The swirl velocity is then:

$$v_{\phi}(\bar{r}) = \begin{cases} \left(\frac{\Gamma_v}{2\pi r_c} \right) \bar{r}, & \bar{r} < 0, \\ \left(\frac{\Gamma_v}{2\pi r_c} \right) \frac{1}{\bar{r}}, & \bar{r} \geq 0. \end{cases} \quad (2.5)$$

Lamb [54] and Oseen [71] came up with an exponential expression. The Lamb-Oseen vortex employs the empirical constant $\alpha_L = 1.256$ with the subsequent swirl-velocity distribution:

$$v_{\phi}(\bar{r}) = \frac{\Gamma_v}{2\pi r_c} \left(\frac{1 - e^{-\alpha_L \bar{r}^2}}{\bar{r}} \right). \quad (2.6)$$

Squire [102] further developed the result of Lamb-Oseen by adding an effective turbulent viscosity coefficient, which describes a higher diffusion due to the turbulence generation instead of molecular diffusion alone. However, this effects only the core growth and not the swirl-velocity distribution itself.

Vatistas [110] derived a more general vortex formulation with an integer variable n , which is given by:

$$v_\phi(\bar{r}) = \frac{\Gamma_v}{2\pi r_c} \left(\frac{\bar{r}}{(1 + \bar{r}^{2n})^{1/n}} \right). \quad (2.7)$$

If the integer variable of the Vatistas model is chosen to be one ($n = 1$), it is equal to the vortex model of Kaufmann [48] and Scully & Sullivan [92]. Due to its algebraic velocity profile, it does not have any singularities. The model is given by:

$$v_\phi(\bar{r}) = \frac{\Gamma_v}{2\pi r_c} \left(\frac{\bar{r}}{1 + \bar{r}^2} \right). \quad (2.8)$$

The Bagai & Leishman [5] vortex is equal to the model of Vatistas with $n = 2$ and is given by:

$$v_\phi(\bar{r}) = \frac{\Gamma_v}{2\pi r_c} \left(\frac{\bar{r}}{\sqrt{1 + \bar{r}^4}} \right). \quad (2.9)$$

The swirl-velocity distributions of all mentioned models are shown in Fig. 2.4. All distributions are normalized by the peak swirl-velocity and the radius at this point. Inside the vortex core ($r < r_c$), most models predict a slightly concave increase of the swirl velocity, whereas the Potential and the Rankine model predict a linear increase. Differences become more pronounced outside of the vortex core ($r > r_c$), where the swirl-velocity decrease differs significantly. The swirl velocities of the already mentioned simple models (Potential and Rankine) are inversely proportional to the radial distance and decrease the fastest. The Lamb-Oseen model is very similar to the Vatistas $n = 2$ model. The Vatistas $n = 1$ model has the shallowest decrease. Further, more sophisticated models with more than one parameter are shown in Fig. 2.5 and will be mentioned below.

So far, the models of Vatistas account only for laminar effects. Therefore, Vatistas et al. [111] extended the vortex model due to turbulent effects by introducing a new parameter β :

$$v_\phi(\bar{r}) = \frac{\Gamma_v}{2\pi r_c} \bar{r} \left(\frac{1 + \beta}{1 + \beta \bar{r}^{2n}} \right)^{\frac{(1+\beta)}{(2n\beta)}}. \quad (2.10)$$

Setting $\beta = 1$, the formula collapses to the original laminar vortex model. When $\beta > 1$, a turbulent vortex type is modeled. The extended vortex model is depicted in Fig. 2.5 for $n = 2$ with $\beta = 1.0, 1.2$ and 1.3 . Increasing the parameter β results

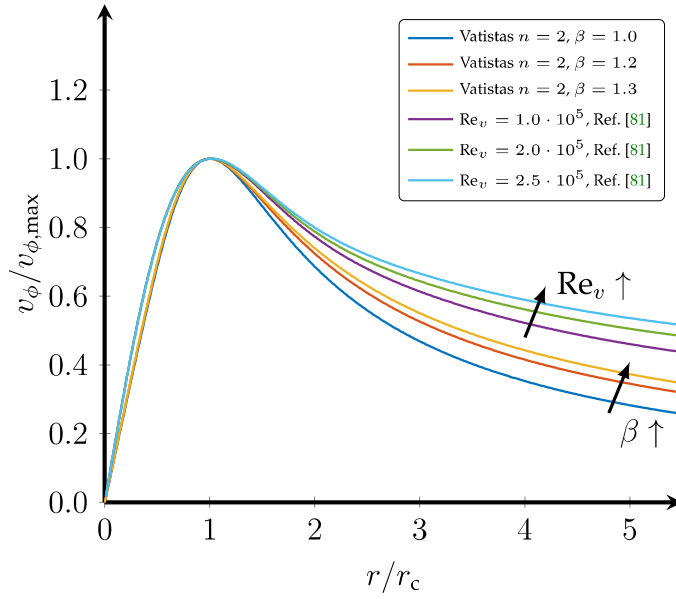


Figure 2.5: Generic swirl-velocity profiles for different vortex models of a blade-tip vortex (arrows depict increase in β and Re_v).

in a shallower decrease in swirl velocities, due to turbulent effects that enhance the mixing of the layers.

Ramasamy & Leishman [80, 81] proposed a new vortex model that considers the influence of the vortex Reynolds-number ($\text{Re}_v = \Gamma_v/\nu$) on the swirl-velocity distribution. First, they formulated a differential equation accounting for a laminar, a transitional, and a turbulent region in the radial direction. In a second step, they fitted an analytical function to their numerical solutions, resulting in a generalized model for the swirl velocity based on the vortex Reynolds-number. This analytical function is given by the following expression:

$$v_\phi(\bar{r}) = \frac{\Gamma_v}{2\pi\bar{r}} \left[1 - \sum_{n=1}^3 a_n \cdot e^{-b_n \cdot \bar{r}^2} \right]. \quad (2.11)$$

The corresponding coefficients for some example vortex Reynolds-numbers are listed in Tab. 2.1.

Table 2.1: Coefficients for analytical vortex model after Ramasamy & Leishman [81].

Re_v	a_1	a_2	a_3	b_1	b_2	b_3
100	1.0000	0.0000	0.0000	1.2515	0.0000	0.0000
$4.8 \cdot 10^4$	0.4602	0.3800	0.1598	1.3660	0.0138	0.1674
$1.0 \cdot 10^5$	0.3021	0.5448	0.1531	1.4219	0.0122	0.1624
$2.5 \cdot 10^5$	0.1838	0.6854	0.1308	1.4563	0.0083	0.1412

The distribution for the vortex Reynolds-number at $Re_v = 4.8 \cdot 10^4$ corresponds to the extended Vatistas model with $n = 2$ and $\beta = 1.38$; see Vatistas et al. [111]. The laminar Lamb-Oseen vortex is predicted with a very low vortex Reynolds-number of $Re_v = 100$. Three customized distributions with different vortex Reynolds-number are plotted in Fig. 2.5, showing a similar trend as the β -extension of Vatistas. The higher the vortex Reynolds-number, the more turbulent effects have an influence on the swirl velocity and widen the distribution towards lower gradients on the outboard of the vortex core. The customized model by Ramasamy & Leishman predicts the highest swirl velocity at $r/r_c = 5$ for $Re_v = 2.5 \cdot 10^5$.

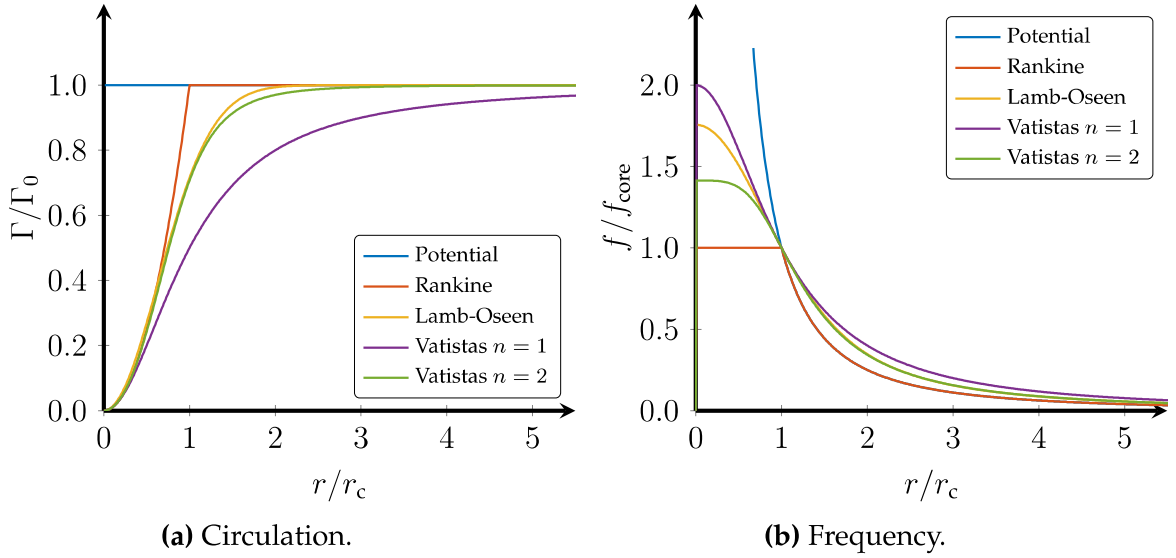


Figure 2.6: Generic circulation and frequency profiles for different vortex models of a blade-tip vortex.

On the other hand, Fig. 2.6(a) shows the circulation of the simpler vortex models. All vortices with an equal swirl velocity at an arbitrary distance have the same dimensionalized circulation. However, the circulation in this plot is normalized by the total circulation Γ_0 at infinity, which is different for each model. Both two models by Vatistas have a different ratio between the circulation within the vortex core and the total circulation. The model by Vatistas with $n = 1$ converges far slower towards the total circulation Γ_0 than the other models. Figure 2.6(b) shows the rotational frequency of the vortex core, which is derived by dividing the swirl velocity with the circumference of the vortex core resulting in the frequency $f = v_\phi / 2\pi r_c$. Those values give an insight into the inherent rotation of the vortex, and a comparison with the rotation of the vortex core shape can be drawn. Apart from the Rankine model, the inner part of the swirl velocity is not linear. These models lead to even higher rotational frequencies inside the vortex core and lower frequencies outside of the vortex core.

So far, all the vortex models have been normalized with their peak swirl-velocity. However, different scaled rotors lead to various vortex Reynolds-numbers and models. The vortex circulation of an ideal rotor operating in hover, see Ref. [56], can be approximated as:

$$\Gamma_v = 2\Omega R c \left(\frac{C_T}{\sigma} \right). \quad (2.12)$$

Consequently, most sub-scale rotors matching C_T/σ and the aspect ratio R/c have a lower vortex Reynolds-number $Re_v = \Gamma_v/\nu$ than their equivalent full-scale rotor. These differences result in different aging processes. Therefore, an equivalent downstream distance instead of the azimuthal angle should be used when comparing rotors of different scales.

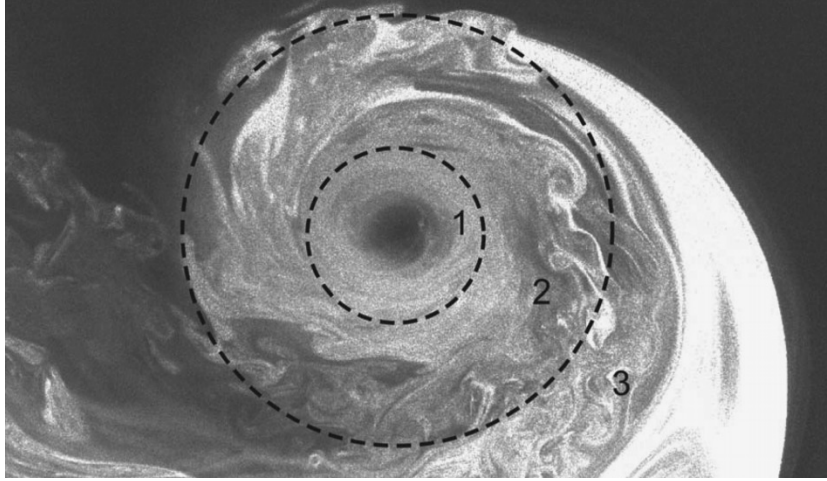


Figure 2.7: Visualization of a fully developed blade-tip vortex with three zones from Ramasamy et al. [79].

Iversen [40] divided the regime of a vortex into a laminar, intermediate, and turbulent region. The region in which the eddy and molecular viscosity are of the same order of magnitude describes the intermediate region. He already distinguished the swirl-velocity profile in these regions. Ramasamy et al. [79] visualized those three zones in a fully developed blade-tip vortex in Fig. 2.7. They divided the vortex in an inner zone ① free of large turbulent eddies, an outer zone ③ with a potential flow, and the transitional region ② in between with eddies of different scales, as shown in Fig. 2.7. Turbulent vortex cores both expand and dissipate quicker than laminar vortex cores. One reason for the different aging processes is the asymptotic decrease of the velocity peaks. Laminar vortices have molecular diffusion alone, whereas turbulent vortices have much higher turbulent diffusion. The swirl velocity decreases faster due to this diffusion. In CFD, vorticity is spread due to numerical diffusion. Therefore, peak velocities are reduced. The use of a detached-eddy simulation (DES) takes

advantage of the above conclusion as the models artificially reduce the turbulence in this area. The smaller eddy viscosity ensures that momentum is mostly transferred by molecular diffusion.

Bhagwat & Leishman [7, 8] followed the approach of Iversen [40] and introduced new nondimensional parameters \hat{v}_ϕ and \hat{d} for the velocity and distance (vortex age), respectively, which can be used as an equivalent downstream distance for vortices:

$$\hat{v}_\phi = \left(\frac{v_\phi}{\Omega R} \right) \left(\frac{\Omega R c}{\Gamma_v} \right) = \frac{v_\phi c}{\Gamma_v}, \quad (2.13)$$

$$\hat{d} = \left(\frac{\Psi R}{c} \right) \left(\frac{\Gamma_v}{\Omega R c} \right) = \frac{\Psi \Gamma_v}{\Omega c^2}. \quad (2.14)$$

These formulations contain the wake age Ψ , the swirl velocity v_ϕ , the chord length c , the rotational speed Ω , and the circulation of the vortex Γ_v . Stronger, more turbulent vortices are characterized to be older by these formulations, whereas a larger chord length or higher rotational speed results in younger vortices which persist longer. With the above-mentioned equivalent formulation, a comparison between a sub-scale and a full-scale test can be drawn.

2.3 Blade-tip vortices of a helicopter rotor

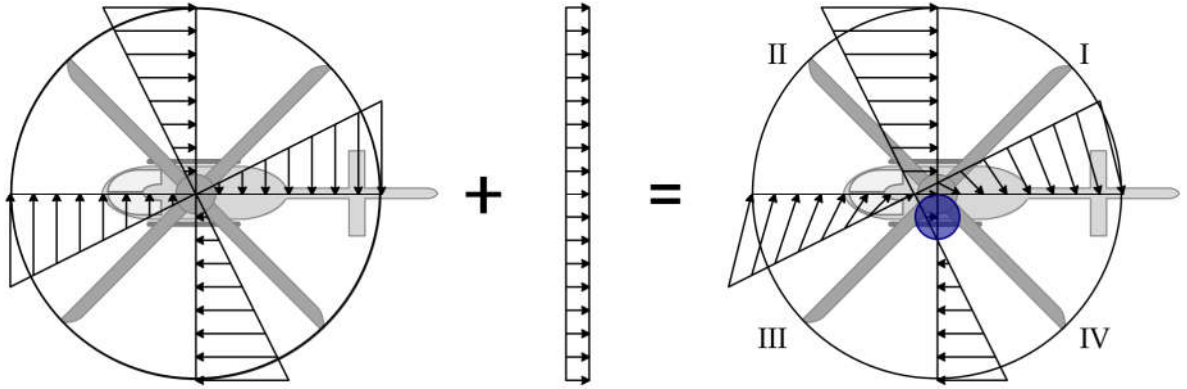


Figure 2.8: Velocity vectors on a blade in hover and in forward flight ($\mu = 0.2$).

The significant difference between helicopters and fixed-wing aircraft is the mechanism by which they generate lift and the consequences thereof. The engines of aircraft produce thrust to maintain a high velocity, which is necessary for the passive lift production with an incoming flow over the fixed-wings. In other words, the thrust and lift production is separated. Helicopters, on the other hand, produce active lift

and forward thrust by rotating blades, which has advantages and disadvantages. For example, the effective cost per weight is much higher than with fixed-wing aircraft; see Ref. [114]. However, one of the advantages is that multiple new flight conditions can be realized with a rotor. For instance, helicopters do not need a long runway since they can take-off and land vertically. Additionally, they can hover. Maneuvering is achieved by tilting the swashplate, which controls the pitch of the blades. The thrust vector tilts accordingly to the varying pitch and flapping of the blades, and the helicopter changes direction. These capabilities outline the field of application. Helicopters are used in areas where the operation of an aircraft is not possible or feasible, which primarily includes rescue or surveillance missions.

Figure 2.8 presents the velocity vectors which impact the blades. The illustration on the left-hand side depicts the situation in hover when the blade experiences an incoming velocity depending only on the distance to the rotational axis. While there is a linear distribution in the radial direction, every profile section encounters only one specific incoming flow without any change in time. The velocity distribution changes if the helicopter performs a forward flight or any other horizontal movement. The right-hand side of Fig. 2.8 illustrates a forward flight with an advance ratio of $\mu = v/U_{\text{tip}}$ of $\mu = 0.2$. Given the depicted counter-clockwise rotation, the blade in the upper half (I + II) is on the advancing side, whereas the lower half (III + IV) is on the retreating side. The effective velocity is higher on the advancing side since the flight velocity has to be added vectorially to the velocity due to the rotation. On the retreating side, the velocities are reduced, even leading to a region (blue circle) with reversed flow as the flight velocity is higher than the rotational velocity close to the rotor hub. Additionally, the forward flight leads to crossflow on the blade. In the front half (II + III), a flow towards the root emerges with the highest cross angle at the root when the blade is pointing in flight direction. On the back half (I + IV), the flow is pushed towards the tip.

The helicopter has to be free of any remaining torque to fulfill a stationary flight. Therefore, to compensate the different incoming velocities and the dynamic pressure the effective angle of attack has to be changed over the azimuth. In addition to the flapping of the blades a cyclic pitch motion changes the angle of incidence of the rotating blades sinusoidally over the azimuth by tilting the swashplate.

Possible compression shocks occurring on the advancing side restrict the maximum advance ratio of the helicopter. However, separation due to the high angle of incidence, which compensates for the low stagnation pressure on the retreating side, additionally restricts the envelope of the helicopter. Figure 2.9 sums up possible flow phenomena during forward flight. Transonic flow on the advancing blade and blade

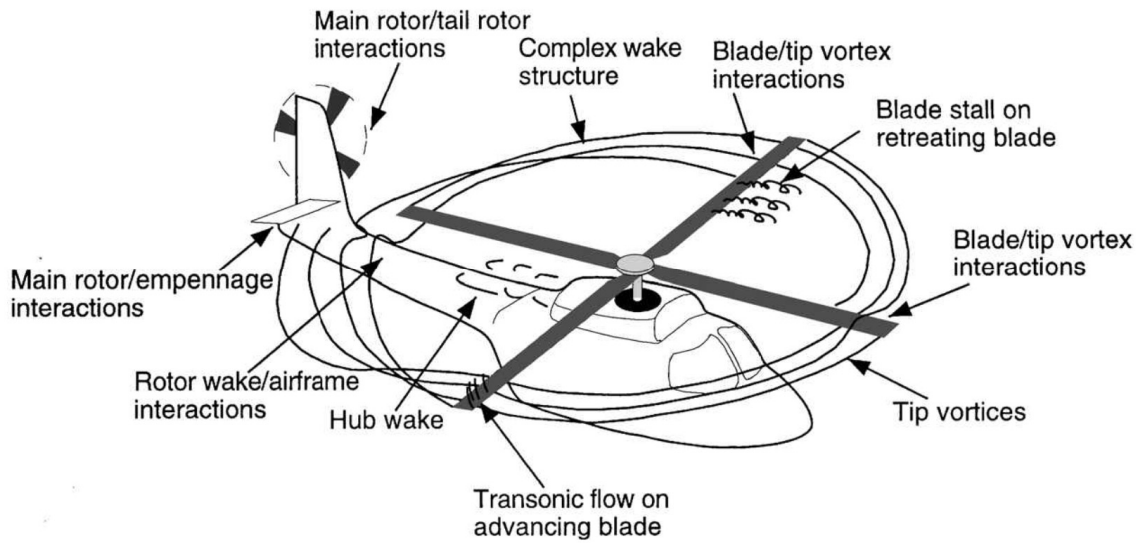


Figure 2.9: Typical flow phenomena during forward flight, from Leishman & Bagai [57].

stall on the retreating blade occur due to the pitch motion of the blade. Interactions between blades and tip vortices can happen in specific flight situations, e.g., slow descent flight. Moreover, several interactions like main- and tail-rotor interactions or wake and airframe interactions take place.

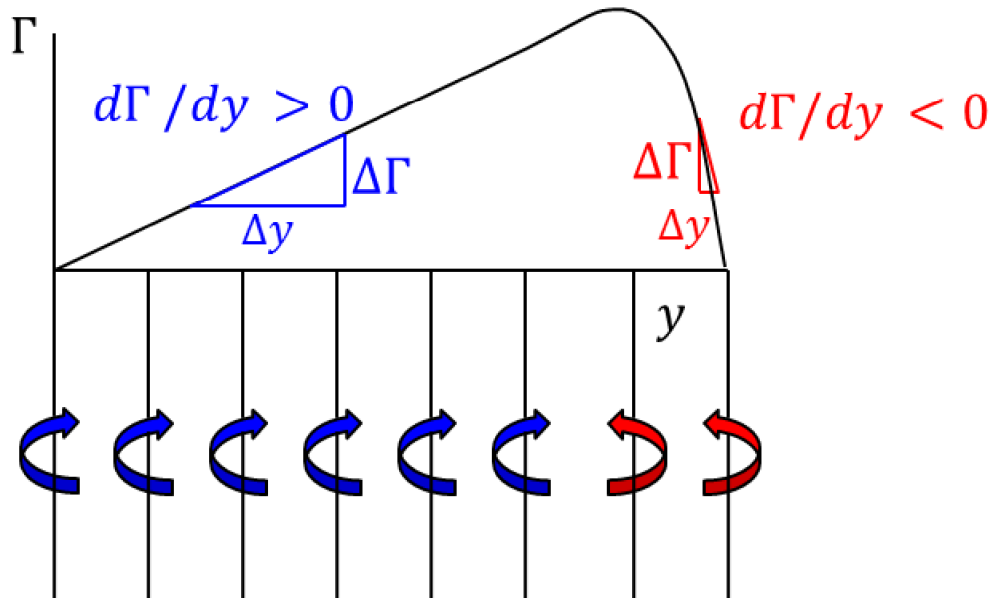


Figure 2.10: Generic circulation distribution over a rotating blade.

In contrast to the distribution over a finite wing, Fig. 2.10 shows the generic circulation distribution over a rotating blade. No lift and circulation is produced at the rotational axis $y = 0$ and at the finite end due to the pressure equalization. The exact distribution depends on several aspects, such as the geometric and aerodynamic twist and the rotational speed. The maximum value occurs close to the end. The almost approximately increase starting at $y = 0$ is due to the linearly varying incoming flow. The gradient in the inner part is positive ($d\Gamma/dy > 0$). The tip vortex is fed by the outer part with the negative gradient $d\Gamma/dy < 0$. Both root and tip vortices have the same circulation strength since the integrated gradients on both sides equal the peak value. However, the rotational senses are reversed due to the different signs of the slopes.

2.4 Finite wing investigations

Significant contributions on blade-tip vortices started with finite wing investigations since the complexity of the experimental setup is lower than with rotating blades. Here, finite wing means that every spanwise section experiences the same constant inflow condition along the span as there is no rotation around the yaw axis. Particularly, the experiment of Chow et al. [22] is still widely used by other numerical researchers [23, 24, 62] for validation purposes. Extensive comparisons between numerical and experimental results were carried out by Dacles-Mariani et al. [24], who compared their numerical findings with a finite wing-tip experiment, which was later separately published by Chow et al. [22]. The authors found good agreement with their structured mesh and stated numerical guidelines of their Reynolds-averaged Navier-Stokes (RANS) simulations.

The experimental work in the near field of a trailing vortex was carried out by Chow et al. [22], who used a pressure probe to investigate the wing-tip vortex of a NACA0012 blade with rounded tips; see Fig. 2.11. The results indicate an almost complete roll-up after one chord length downstream. In particular, secondary and tertiary vortices dependent on specific blade-tip geometries merge into the primary vortex within a short distance. The data of the roll-up of the wing-tip vortex and their turbulence measurements with a triple-wire probe by Chow et al. [22] serves as validation for numerical investigations. However, the analysis of vortices with a probe is subject to several systematic errors, particularly regarding the probe positioning. The static measurements were conducted up to $x/c = 0.678$ downstream of the trailing edge, showing a jet-like behavior of the vortex as the core axial velocity reached values 1.77 times the velocity outside the vortex.

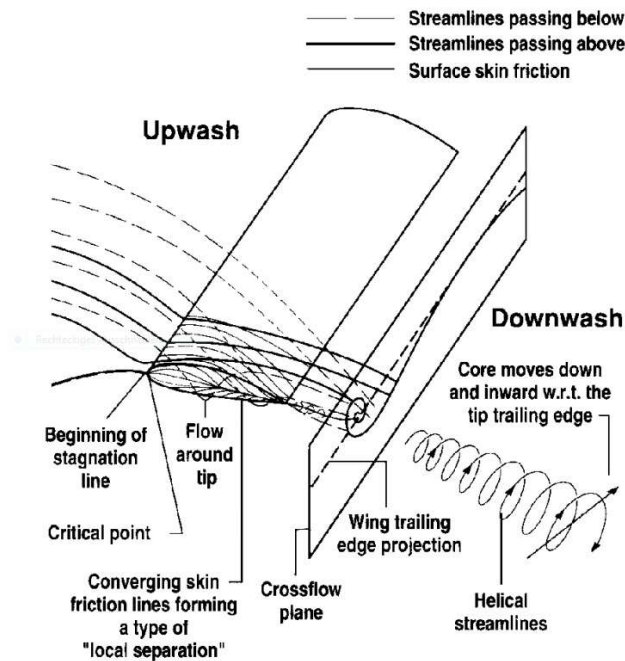


Figure 2.11: Initial roll-up of a wing-tip vortex from Chow et al. [22].

Likewise, Churchfield & Blaisdell [23] performed numerical simulations of the experiment of Chow et al. [22] using RANS equations. Following the numerical guidelines of Dacles-Mariani et al. [24], they implemented a grid with 21 points across the estimated core and 5.3 million grid points in total. All investigated turbulence models had deficiencies, with the Spalart-Allmaras turbulence model with rotational correction [94, 98] matching the experimental pressure in the vortex core within 10%. The Menter [64] shear-stress transport (SST) model showed a diffuse behavior in this RANS computation. Next, Uzun et al. [109] performed the first large-eddy simulation (LES) on a tip vortex by computing the experiment of Chow et al. [22]. LES is a useful tool to study blade-tip vortices, as large structures are resolved directly, and only small scales need to be modeled. Due to increasing computational performance, such computations have become more feasible, though the requirements are still very high for Reynolds numbers of practical applications. For that reason, the authors reduced the Reynolds number by almost an order of magnitude to keep the simulation on a feasible level with 29.4 million grid points. Another difference is the natural numerical transition to turbulence. Some comparisons showed good agreement, but viscous effects were higher in the LES simulation due to the reduced Reynolds number resulting in differences. Employing the results by Chow et al. [22], Lombard et al. [62] validated their LES of the NACA0012 profile recently. The Reynolds number was only four times lower than in the experiment, and they corrected the wind tunnel effect with an increase of 2° of the angle of incidence. Their 243 000 elements had

around 16.7 million degrees of freedom. However, this coarse grid leads to noisy results. Nevertheless, they matched both the jetting velocity and the vortex spanwise location well.

2.5 Oscillating wing investigations

Consequently, investigations on pitching wings were the subsequent step. Extending prior studies, Spentzos et al. [101] performed investigations on high aspect ratio twisted wings. They analyzed the interaction of the dynamic stall vortex with the tip vortex numerically. The unsteady Reynolds-averaged Navier-Stokes (URANS) simulations matched the available experimental data with good accuracy. The Ω -shaped vortex in Fig. 2.12 was observed at any investigated planform shape once dynamic stall conditions were achieved even though the formation and evolution differed according to the tip geometry.

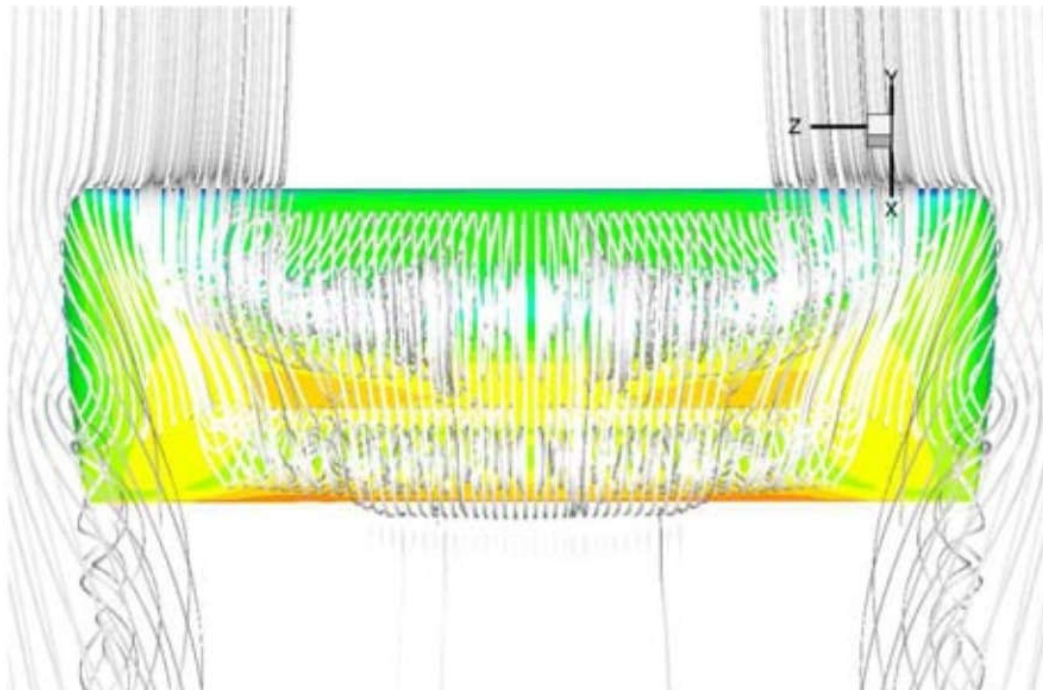


Figure 2.12: Plan view of the Ω -shaped dynamic stall vortex from Spentzos et al. [101].

Similarly, Zanotti & Gibertini [120] and Nilifard et al. [69] did experimental and numerical investigations on the three-dimensional effects on a pitching airfoil. The comparison of the dynamic stall case showed good agreement when 3D numerical models were employed. With these methods, the three-dimensional effects of dynamic

stall could be obtained.

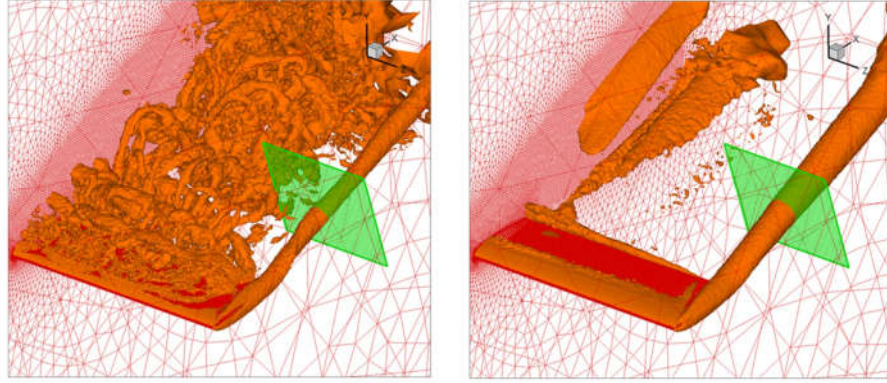


Figure 2.13: DES (left) and URANS (right) λ_2 isosurfaces around NACA0015 from Mohamed et al. [68].

Contrary to the RANS simulations, Mohamed et al. [68] employed DES on a stationary as well as on a pitching airfoil; see Fig. 2.13. They investigated the wing-tip vortex at static and dynamic stall conditions reporting DES outperforming the RANS models in matching the jetting velocity and the vortex spanwise location. The vortex swirl-velocity and core radius were far more precisely matched with the experimental data of Birch & Lee [11] when DES was used. The RANS method predicted vortex radii twice as large. In the pitching case, the DES results exhibited the variation of vortex parameters, which was found in the experimental data, more clearly, whereas the plain URANS results almost did not show any hysteresis at all. Correspondingly, Birch & Lee [9–11] investigated oscillation wings, noting that the overall vortex structure did not significantly differ compared to a vortex of a static wing. The similarity was more prominent during the upstroke motion. The unsteady vorticity distribution appeared even more organized and less diffusive, whereas the circulation distribution varied considerably. Nevertheless, they showed self-similarity up to $r/r_c = 1.4$. Additionally, they addressed a solution to the phase-lag problem by assuming the convection velocity of the propagated flow structure to be constant and equal to the free-stream speed. This assumption is justified by neglecting any streamwise distortion. Thus, the angle of attack can be compensated by the past angle of attack the wing or blade had once the vortex was generated. The reference position is commonly the trailing edge in the literature.

Wolf et al. [118] analyzed the wing-tip vortex of a finite pitching wing with the DSA-9A airfoil and SPP8 blade tip. Figure 2.14 shows the instantaneous particle image velocimetry (PIV) flow fields in the oscillation cycle. A wake-like vortex occurred with strong separation in the downstroke. Additionally, they observed that the tip vortex continued becoming stronger with increasing angle of attack even after

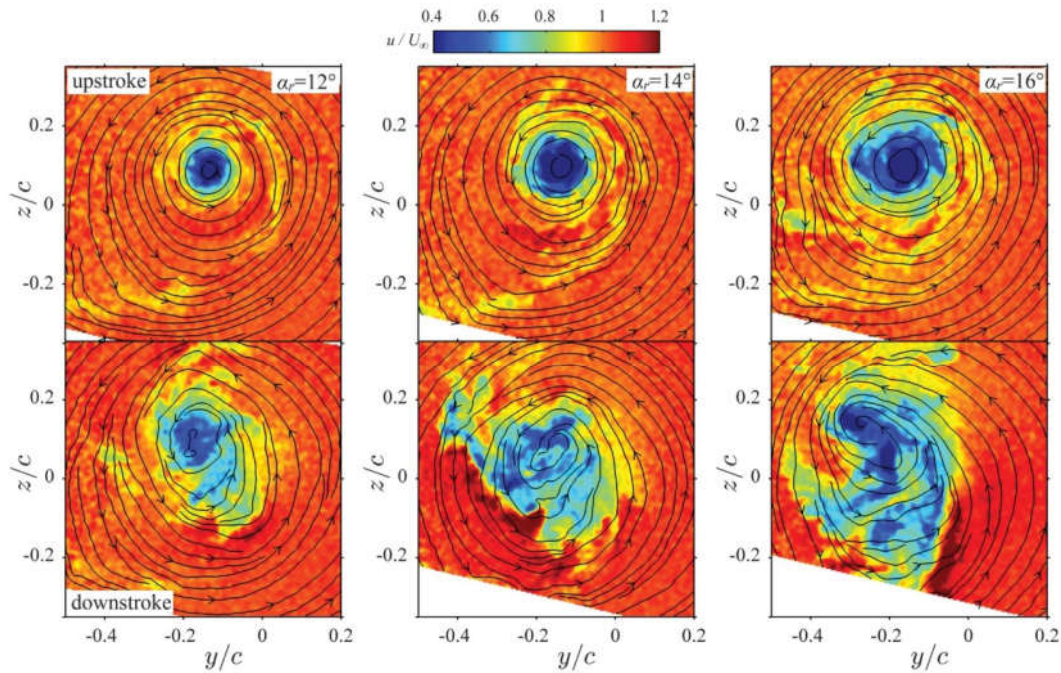


Figure 2.14: Instantaneous axial velocity fields of a tip vortex from Wolf et al. [118].

the flow on the wing stalled. The corresponding numerical investigation has been carried out by Kaufmann et al. [47], who reproduced the experimental results for the very young vortex using RANS equations with a sufficiently fine grid. Both studies provided experimental and numerical data of circulation as well as swirl velocity. Other investigations of the same nonrotating wing with the focus on dynamic stall have been carried out by Merz et al. [66] and Kaufmann et al. [46].

Lately, Garmann & Visbal [29–31] performed extensive numerical LES of the NACA0012 profile. They compared the vortex at fixed and various oscillating conditions at up to three chord lengths downstream, observing an orbital rotation of the vortex core. Furthermore, they found out that the vortex appearance (wake- or jet-like) is not driven by wake interactions.

2.6 Rotating blade investigations

Blade-tip vortices evolve in a highly complex three-dimensional process. Consequently, the rotating blade is a further step towards the aerodynamics of a helicopter. The pitching motion, necessary for any translational flight, complicates the aerodynamic situation even more. The requirements for experimental and numerical investigations of blade-tip vortices in a rotating setup are therefore far higher. For example, a larger refined area is needed as the rotor moves through a much bigger domain during one period. Simulations with these finer requirements became only

feasible in the last years with the emergence of massive parallelization. Simulations with URANS equations have been widely used to investigate blade-tip vortex flows. As computational performance is still increasing, higher fidelity approaches are becoming more common. This section is dedicated to the prior numerical and experimental research of wing-tip vortices. Validation of the numerical methods with experimental results is still necessary. Therefore, investigations, including both methods and their comparison, are favored.

Early smoke studies by Gray [34] visualized the vortex pattern of a helicopter rotor, leading to the sketch of the vortex pattern of a single-bladed hovering helicopter in Fig. 2.15.

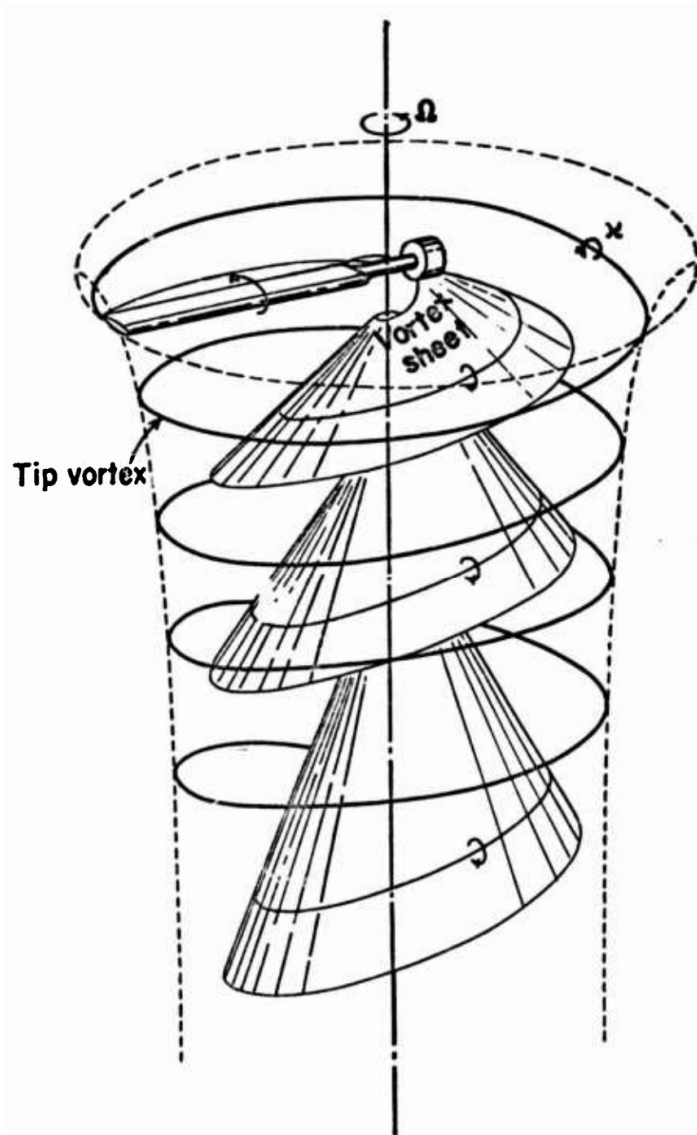


Figure 2.15: Sketch of helical vortex pattern of a single-bladed hovering helicopter from Gray [34].

In contrast to earlier investigations, Caradonna & Tung [18] obtained the blade loading and wake characteristics simultaneously. For this, the authors used hot-wire measurements and pressure transducers to analyze the vortex geometry and strength of a two-bladed rotor in hover. They acquired the data by traversing the hot-wire probe beneath the rotor and gathered data at various points along the vortex trajectories. To deal with the unsteadiness of the flow and the probe location, they only used data when a vortex hit the probe. Furthermore, the authors noted that the trajectory and strength are independent of the tip speed. Srinivasan & McCroskey [103] solved the thin-layer Navier-Stokes equations in a rotor coordinate system to compare with Caradonna & Tung [18]. They accounted for the induced wake effect with a correction of the geometric angle of attack and reached a good comparison. Furthermore, they transferred the obtained circulation distribution on an equivalent fixed-wing to calculate a simulated hovering flow field. The surface pressure showed that the centrifugal forces seem to have only a minimum influence.

Likewise, Joulain et al. [44] constructed a fixed-wing equivalent configuration to accelerate tip vortex computations. A comprehensive rotor code was used for the induction of the wake, and a CFD solver accurately simulated the tip region. Their results were also validated with the experimental data of Caradonna & Tung [18]. The agreement with the database of Gray et al. [35] was strong, with some differences due to the missing of centrifugal effects. Non-intrusive measurement techniques, on the other hand, have advantages over probes when characterizing the flow. Thompson et al. [106], for example, measured the tip vortex core with three-component (3C) Laser Doppler Velocimetry (LDV). They reported that cycle-to-cycle fluctuations made it difficult to extract the size of the vortex core. However, the particle void helped in finding the vortex locations. Furthermore, they obtained axial- and swirl-velocity profiles along the radial coordinate and found considerable differences in structure from a fixed-wing vortex. Likewise, Leishman et al. [58] investigated the tip vortex of a single-bladed hovering rotor with 3C LDV. They obtained a tangential velocity profile, which agreed well to the Vatistas vortex model. They stated that the tip vortex gained its maximum strength within 90° . Leishman & Bagai [57] reported on the challenges occurring in vortex studies. They focused mainly on LDV and flow visualization methods, which are shown in Fig. 2.16.

A further development was the additional use of PIV. Raffel et al. [77], for example, examined the flow field at one rotor azimuth location of a helicopter rotor model in forward flight with LDV and PIV. They reported a good agreement; however, LDV was superior in measuring all three components, whereas the faster data acquisition of PIV allowed capturing the unsteadiness of the flow. Heineck et al. [37] expanded the

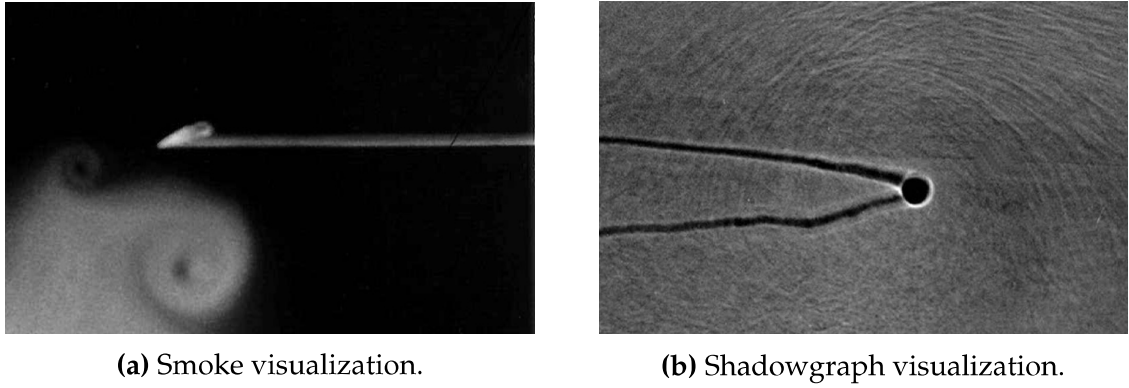


Figure 2.16: Visualization of blade-tip vortices from Leishman & Bagai [57].

conventional PIV arrangement with a stereoscopic approach. This technique enabled extracting all three velocity components of the flow field of a two-bladed hovering rotor. Bhagwat & Leishman [7] performed 3C-LDV of single and two-bladed sub-scale rotors in hover. They found self-similar vortices with an almost constant strength. Burley et al. [17] examined the forward flight of a scaled rotor with the PIV technique in the HART-II test campaign. The authors thoroughly scanned the resulting wakes to investigate their evolution, starting from their creation. Furthermore, they defined new processing methods, which ignore velocity fields with peak vorticity values not exceeding 20% or 80% of the overall maximum value. These methods exclude noisy images and isolate the vortex. Also, they discovered a range of different swirl-velocity shapes over the rotor disk. Richard & van der Wall [84] investigated the vortices with two-component (2C) and three-component (3C) PIV. They used a scaled rotor with different revolutions per minute in hover conditions. By following the vortex half a revolution, they optimized the correlation window size and the overlap. They also confirmed that a high resolution is necessary to capture young vortices. Furthermore, they found that swirl velocity and core radius are independent of the tip speed. Kindler et al. [50] performed hover studies of a full-scale rotor observing eccentricity effects only up to $\Psi_V = 1^\circ$, at later wake ages the vortex relaxes. A thorough numerical and experimental study was performed by Duraisamy et al. [26], who examined the on-blade formation of the tip vortex of a single-bladed hovering rotor at $Re_{tip} = 272\,000$. They identified multiple vortex structures merging into a single coherent vortex in simulations and experiments.

Ramasamy et al. [78] introduced a new method to account for aperiodic experimental data and found only elliptical shapes of the vortex core. They corrected the centers by collocating them based on their helicity. In a subsequent study, Ramasamy et al. [79] compared PIV and LDV results and found a good correlation between those two measurement techniques.

Full-scale studies of the UH-60A helicopter have been analyzed experimentally by Yamauchi et al. [119] and numerically by Potsdam et al. [72]. Yamauchi et al. [119] performed a full-scale study on the UH-60A rotor tip vortices in forward flight, investigating the vortex on the advancing side over several wake ages observing a constant change of circulation and core size; see Fig. 2.17. Milluzzo & Leishman [67] investigated the twist of the blade by comparing an untwisted and linearly twisted blade of a hovering rotor. With the twisted blade, a more uniform load was formed, leading to more uniform convection of the wake sheet. However, the vortex sheet was more intense with the twisted blade, and it contained almost as much vorticity as the tip vortex. According to the authors, the characteristics of the tip vortex are affected by the radial lift distribution.



Figure 2.17: Laser sheets in the 40- by 80-foot wind tunnel from Yamauchi et al. [119].

Using several methods, Chaderjian & Buning [21] performed high-resolution simulations with plain URANS, hybrid URANS, and LES approaches on the tilt-rotor aeroacoustics model at several collective angles. They focused on grid resolution and time accuracy, concluding that at least a drop of 2.2 orders in residual for each time step is considered converged. The numerical parameters of $\Delta\Psi = 0.25^\circ$ and 20 inner iterations sufficed to reach the desired order drop and have been continued by other researchers like Ahmad et al. [1] and Potsdam & Jayaraman [74]. Subsequent studies by Ahmad et al. [1] showed that $\Delta\Psi = 0.25^\circ$ and 18 inner iterations are sufficient for convergence.

Gardner & Richter [27] studied the effect of rotation on dynamic stall. The single-bladed rotor was investigated with and without rotation and compared with 2D computations. A reduction in the strength of the dynamic stall vortex was observed.

To compare with the experimental results by Yamauchi et al. [119], Potsdam & Jayaraman [74] performed coupled CFD simulations (Fig. 2.18) of the UH-60A. They used a weak coupling method for this forward flight configuration and achieved a drop of 2.5 orders in the residual, employing 40 inner iterations. The available PIV data on the advancing blade was compared with the simulated wake, allowing the origin of vortical structures to be effectively traced with good agreement. Furthermore, the authors state that with sufficient grid resolution wake ages up to a rotor radius ($\Psi \approx 60^\circ$) can be well computed. With adaptive mesh refinement, they had a grid with up to 1.7 billion grid points.

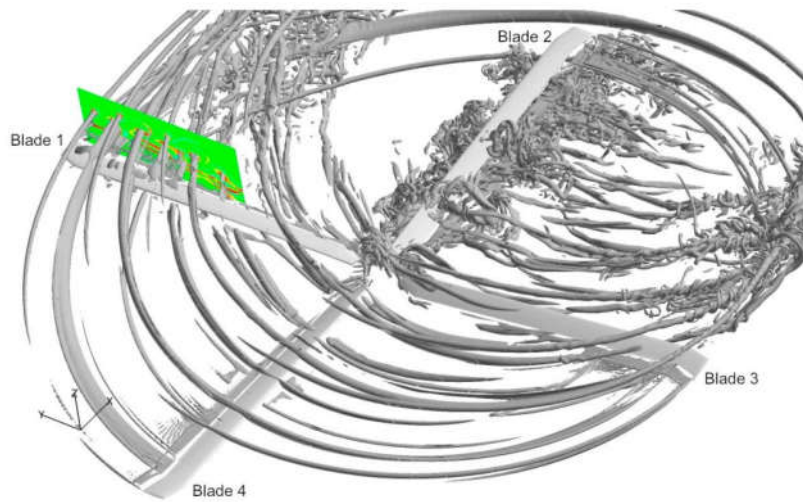


Figure 2.18: Visualization of Q isosurfaces from Potsdam & Jayaraman [74].

Instead, Jain [41] undertook hover simulations, investigating the effect of grid and solver settings on vortex development. The author concluded that the core radius and circulation were insensitive to the approach used, but that the low dissipation of DES appeared to give a critical advantage in the vortex modeling. Consequently, Chaderjian [20] used a delayed detached-eddy simulation (DDES) approach to investigate a UH60-A in forward-flight. In contrast, Richez [85] used a second-order URANS approach to simulate BVI leading to dynamic stall, with considerable success in reproducing wind tunnel data of the test case. He pointed out that with an engineering approach, a grid cell in the refinement area is as big as the expected blade-tip vortex. The computational costs exceed most engineering analysis, restricting a more realistic vortex core size. The coarse wake grid is sufficient for engineering air loads prediction, whereas a finer grid is necessary to model the rotor-wake interactions accurately. However, Jayaraman & Potsdam [42], who used a similar approach to investigate the effects of the fuselage and wind tunnel on the wake, noted that even when the vortex properties are well predicted, a misprediction of the wake trajectory can have

a critical effect on the prediction of the interaction aerodynamics. Therefore, Öhrle et al. [70] used higher-order coupled simulations and adaptive mesh refinement to avoid vortex dissipation reaching with both a periodic and time-dependent approach a comparably preserved vortex.

Schwermer et al. [90] experimentally analyzed dynamic stall at the rotor test facility (RTG) at the DLR in Göttingen [91]. The RTG rotor has been computed using stiff blades with prescribed motion in a simple far field boundary condition by Letzgus et al. [59], resulting in good agreement with the experiment performed by Schwermer et al. [90]. Uluocak et al. [108] analyzed different tip geometries and observed varying swirl-velocity and circulation levels due to different tip geometries. An anhedral blade gave the minimum circulation. Most recently, Lietzau et al. [61] compared numerical simulations with dual-plane PIV measurements of a single-bladed hovering rotor. They reported difficulties in finding a grid-independent solution. The core radii of vortices at a young wake age ($\Psi_V < 15^\circ$) were consistently overpredicted by all investigated grids, grid stencils, and turbulent models. The peak swirl-velocity showed a better agreement with the PIV measurements leading to good agreement of the circulation of the vortex.

2.7 Scope of this work

The literature lacks an analysis combining both experiments and simulations to study the blade-tip vortex of a full pitching cycle in a rotating setup. This study, therefore, uses a setup to measure and simulate any azimuthal position of a pitching and rotating blade. The RTG uses a rotating outer swashplate, which allows moving any point in the pitching cycle to any azimuth. The drawback of this method is that no real forward flight situation with the typical Reynolds and Mach number variation is modeled. Instead, the incoming flow parallel to the rotor axis simulates a climbing flight. However, the effect of the pitching motion can be analyzed with this configuration. The stiff blades ensure that no deformation solver needs to be coupled with the aerodynamic solver. The existing experimental database is for a full pitching cycle of a rotor blade. A URANS approach is used for the simulations switching to under-resolved LES models in specific areas, thus resulting in a DES approach. A full LES simulation is not feasible with the available computing power. Additionally, the adjacent body area is often computed with RANS simulations, requiring that the first research question be investigated using a plain URANS approach.

Two primary investigations of a two-bladed and four-bladed rotor are conducted. A high cyclic motion with dynamic stall is investigated with a two-bladed configura-

Table 2.2: Root angle Θ_r of investigated CFD cases.

	Two-bladed rotor	Four-bladed rotor
Static (no pitching)	-	$18^\circ ; 21^\circ ; 24^\circ ; 27^\circ ; 30^\circ$
Unsteady (pitching)	$23.7^\circ \pm 6^\circ$	$24^\circ \pm 6^\circ$

tion, whereas non-pitching cases and a pitching case without stall of the four-bladed configuration are compared. Table 2.2 displays the numerical test cases which have been investigated. The left side lists the case of the two-bladed configuration. The pitching case of $\Theta_r = 23.7^\circ \pm 6^\circ$ extends into the dynamic stall region. Static test cases are done for the four-bladed configuration (right side) next to a corresponding pitching case, which is in attached flow despite the higher nominal angles of incidence. At the same angle of incidence, the four-bladed configuration produces more thrust, which reduces the effective angle of attack.

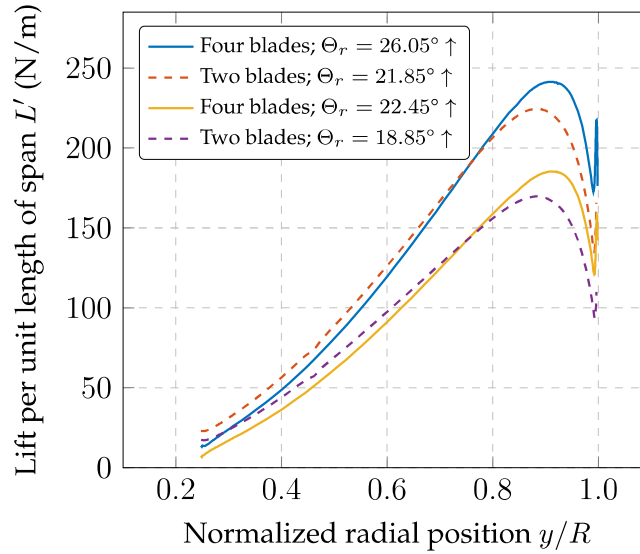


Figure 2.19: Radial lift distribution on the blade for different pitch angles during the upstroke motion for two and four-bladed configuration with similar thrust.

A comparison of cases providing the same amount of thrust F_z is displayed in Fig. 2.19, which shows four different lift distributions on the blade. They result by the integration of the surface pressure distribution at each radial station of two different azimuthal positions of both configurations. The enclosed area below the curves corresponds to the total thrust of each blade. Dashed lines represent the two-bladed rotor; solid lines the respective four-bladed rotor. The comparison is drawn between two situations during the upstroke motion that produce the same amount of thrust

per blade. Each blade of the upper lines provides around $F_z \approx 63 \text{ N}$ with a deviation of 0.5%, whereas the two lower lines represent situations with $F_z \approx 48.5 \text{ N}$ with a difference of 0.3%. For the higher thrust case, the four-bladed configuration needs a $\Delta\Theta_r = 4.2^\circ$ higher angle of incidence to match the same thrust. The difference in the lower thrust setting is $\Delta\Theta_r = 3.6$. The higher overall thrust when using more (four) blades generates more downwash, and therefore reduces the effective angle of attack. Besides, the gradient of thrust over the angle of incidence is steeper for the two-bladed rotor. The same spanwise lift is produced at around $y/R \approx 0.75$. Further outboard, the four-bladed configuration provides more lift, which is then compensated by the reduced lift over the longer inboard range. The shape of the lift distribution influences the strength of the blade-tip vortex circulation, which depends on the peak lift per unit length of span.

3 Tools and methods

This chapter presents the numerical tools and analytical methods employed in this thesis. The first section covers the finite-volume solver DLR-TAU code. An introduction of the experimental setup is then given in the subsequent section 3.2. Afterward, the geometric model is presented. Finally, the chapter finishes with the coordinate system and an error analysis of the implemented algorithms.

3.1 Finite-volume solver

The DLR-TAU code [87] solves the compressible Navier-Stokes equations of steady or unsteady flows. The employed method is a finite-volume approach and can solve RANS, URANS, LES, and DES equation systems. The domain can be organized by a hybrid grid with tetrahedra, prisms, pyramids, and hexahedra. The differential equations with boundary conditions are then solved in every cell of this grid. Since DLR-TAU is a node-based solver, it first creates the finite volume around each given grid point. The closure of the equations is done by a chosen turbulence model - either an eddy-viscosity or a Reynolds-stress model (RSM) is chosen for this. These two approaches distinguish how the six unknown components of the Reynolds stress tensor are solved. While the RSM opens up six new differential equations, the eddy-viscosity models are based on the Boussinesq-hypothesis, which adds an eddy viscosity onto the molecular viscosity. Furthermore, the eddy-viscosity models can be classified by the number of additional equations. The aim is always to determine the length- and velocity scales. Pure algebraic models (zero equation) are very specific and only feasible for few cases in which the geometry, velocity gradient, and distance to the wall affect the length- and velocity scales. One-equation models solve an additional transport equation. A possible quantity is, for example, the turbulent kinetic energy k or the eddy viscosity ν_t , which is solved in the model of Spalart-Allmaras [98] of 1992. Two additional equations of the turbulent kinetic energy k , its dissipation rate ϵ , or the turbulence frequency ω form the two-equation models.

Popular are the $k - \epsilon$ and the $k - \omega$ models of Wilcox [116]. A combination of both models results in the Menter [64] shear-stress transport (SST) turbulence model, which uses in different domains either $k - \epsilon$ or $k - \omega$ model depending on their superiority. To simulate unsteady cases, a dual-time stepping approach with physical time steps and inner iterations is used. Any movement happens in the physical time steps, which consist of many inner iterations. These iterations are pseudo time steps as the physical time is held constant. In this study, there is always a fixed number of inner iterations set. Even the static cases of a non-pitching blade are computed with a dual-time stepping approach for robustness reasons.

Levels of fidelity

RANS methods solve the Reynolds-averaged version of the Navier-Stokes equations. The turbulence is modeled to close the mathematical differential equations. However, some high fidelity approaches use direct numerical simulation (DNS) of the Navier-Stokes equations without any models. This section gives an overview of approaches that need less modeling than RANS methods. An LES resolves, in contrast to RANS, the largest eddies in a separated turbulent flow and uses a sub-grid scale (SGS) model to treat smaller structures than the filter size. The requirements towards the grid or solver are more stringent compared to the RANS equations. A higher-order solver is desired, and the grid should be finer than the chosen filter size. Since these requests are still too high for many applications, a combination of LES and RANS, called detached-eddy simulation (DES), can be used. The basic idea behind DES is switching between the LES and RANS approach. In regions with attached flow, a RANS solution is preferred, whereas LES is used for regions with separated flow. Therefore, the switching operates according to the size of the cell and its distance to the wall, see Spalart et al. [100], who propose to replace the distance in the destruction term with the minimum of either a scaled cell size or its distance to the wall. Thus, small cells close to the wall, which occur in the boundary layer, will still be treated with the RANS approach. Yet, thick and refined boundary layers can exhibit fine cells that would be treated with the LES model. Therefore, Spalart et al. [99] developed a new version called Delayed DES (DDES), which preserves RANS behavior in the boundary layer. Later, Shur et al. [93] formulated a new strategy (Improved DDES) which allows wall modeled LES if resolved turbulence enters a well discretized region of the boundary layer. HELIOS, a helicopter overset simulation tool, for example, uses a multi-solver paradigm [73] with the ability to use different grids. The near body grid is a RANS solver. LES capabilities are employed in the background grid. In 1997, Spalart et

al. [100] presented an estimation on the feasibility of LES for wings in an industrial context. They concluded that 10^{11} points are needed under very favorable conditions. Back then, simulations with 10^8 points were impressive. Recently, Slotnick et al. [95] presented their CFD vision. Looking ahead to the year 2030, they draw a picture that even the leadership supercomputer will not be able to compute a wall-modeled LES for higher aspect ratios at the Reynolds numbers of interest.

To resolve even smaller scales, DNS have to be used. This approach does not model eddies with turbulent models anymore as it resolves them in time and space. The requirements on the grid are extraordinarily high, since all scales, down to the Kolmogorow length scale ($\eta = (\nu^3/\epsilon)^{1/4}$, [51, 52]), have to be resolved. Considering this requirement, a grid size of $\text{Re}^{\frac{9}{4}}$ in space is requested. A DNS simulation of a full-scale plane in cruise ($\text{Re} \gg 10^6$) is therefore still beyond the current computer possibilities. Spalart [97] sees this scenario to be feasible by 2080 with a grid of 10^{16} points.

In the course of this study, DES with a zonal LES approach is carried out with up to $8 \cdot 10^7$ grid points in total. The desired region is defined by geometric shapes like cylinders or frustums. Then TAU checks the distance to the wall and decides whether to use RANS or LES models. The purpose of DES is better conservation of the blade-tip vortices. This is achieved because the eddy viscosity, ensuring a rapid dissipation, is decreased in the LES region. Another possibility to increase vortex conservation has been realized by Probst et al. [75] and Löwe et al. [63], who implemented a low-Dissipation low-Dispersion (LD2) method. The specific numerical setups are focused on separately in the following chapters.

3.2 Experimental setup

The experimental setup is presented in order to understand the upcoming results. However, it should be clarified that the experiments were not primarily done by the author. Existing results are obtained and published by Wolf et al. [117] and Braukmann et al. [14].

Figure 3.1 shows the horizontally mounted, four-bladed rotor from the rotor test facility (RTG) in Göttingen [90]. An Eiffel-type wind tunnel produces a slow uniform flow up to $U_\infty = 14 \text{ m/s}$. The rotor is mounted horizontally with the wind tunnel inflow axially from the side. The setup enables the extraction of PIV data for a complete cycle. This is possible due to a rotating outer swash plate which moves any point in the pitching cycle to the measurement plane. The wake is propagated out of the room through open doors, avoiding recirculation. Algorithms detecting

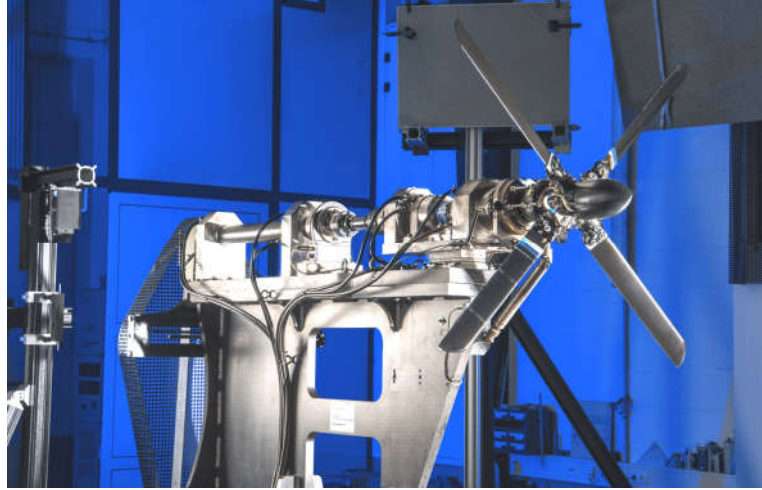


Figure 3.1: Overview of the RTG.

vortex parameters can, therefore, be employed. The stiff rotor can be operated with a high cyclic pitch, allowing the creation of unsteady aerodynamic phenomena that are relevant to helicopters. The stiff blades allow azimuthal averaging in attached flow conditions.

The experimental investigations used the RTG operating with a high cyclic pitch. This generates a highly unsteady and three-dimensional flow, which is periodic in attached flow conditions. The pitch variation is analogous to that for helicopters in forward flight, but without the Mach and Reynolds number variation typical of that flight condition. Therefore, the RTG allows the investigation of the aerodynamical effects of rotating and pitching blades and their vortices without the need for an expensive forward flight wind tunnel experiment. The drawback of this simplified approach is the lack of an advancing or retreating side and realistic BVI, as only one constant incoming velocity can be investigated. A low velocity approximates the flow situation on the retreating side. The modeled inflow ensures that the vortices are pushed downstream.

The RTG, see Fig. 3.2, consists of a rotor ① with a horizontal axis fed by a wind tunnel ② with a square 1.6 m by 1.6 m nozzle producing a slow uniform flow of 2.2 m/s. The distance to the rotor is 0.65 m, and the rotor is approximately 12 m away from the hall exit ③.

All experiments in this study were run with a rotational frequency of 23.6 Hz, a chord length $c = 0.072$ m, and a blade radius $R = 0.65$ m, resulting in a tip Reynolds number of $Re_{tip} = 470\,000$ and tip Mach number of $M_{tip} = 0.28$. Load analysis by Schwermer [89] restricts higher rotational frequencies and therefore higher Mach numbers at the prescribed pitch motions in Tab. 2.2. Accordingly, the test results

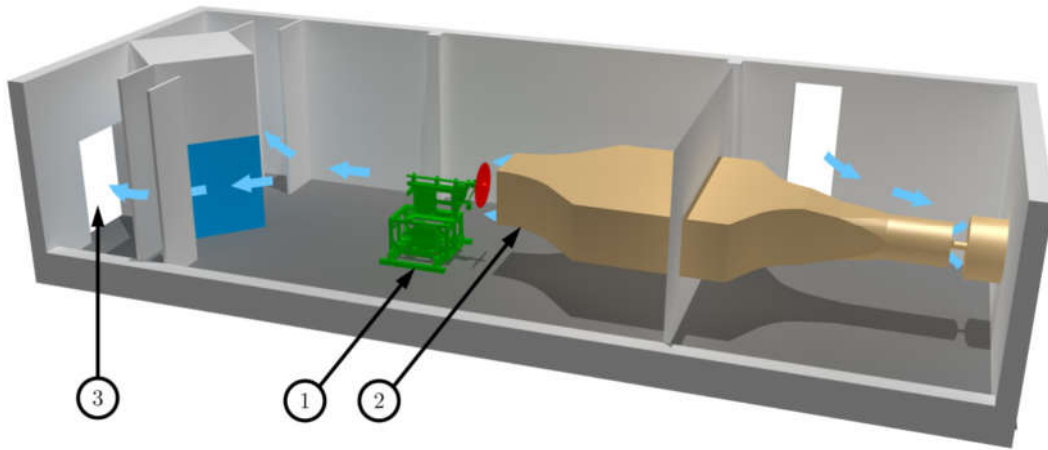


Figure 3.2: The RTG at the DLR in Göttingen (adapted from Schwermer et al. [91]).

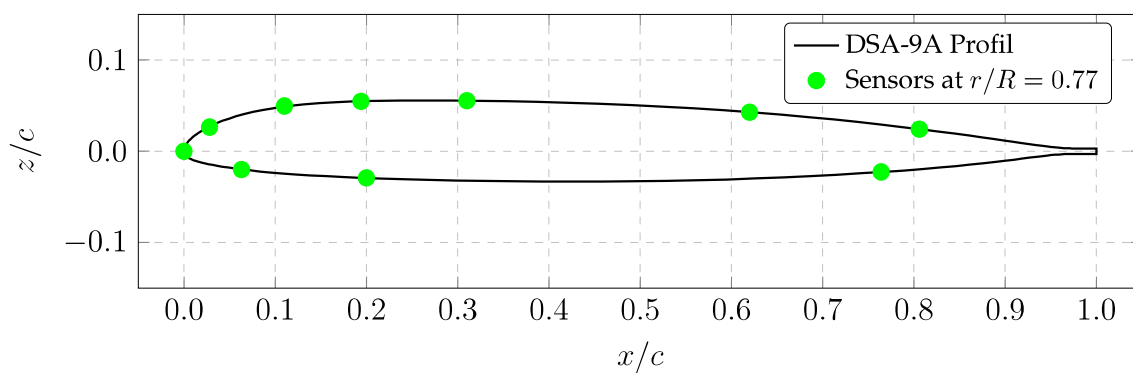


Figure 3.3: DSA-9A airfoil with experimental sensor positions.

are not Mach scaled. The focus, however, is on the numerical and experimental tip vortex in attached and dynamic stall conditions. The numerical settings replicate these experimental flow conditions to allow equal comparisons. Each of the blades is equipped with a DSA-9A airfoil, which is a modern 9% industry relevant helicopter profile; see Fig. 3.3. One of the two or four rotor blades is instrumented with pressure sensors, four sensors at $r/R = 0.53$, and nine sensors at $r/R = 0.77$. These sensors are used to compute sectional coefficients. Since the influence of the numerical error due to the coarse distribution is not negligible, CFD data is also reduced to these positions when comparing them. Parameters of the experiment, which were also used for the simulations, are listed in Tab. 3.1.

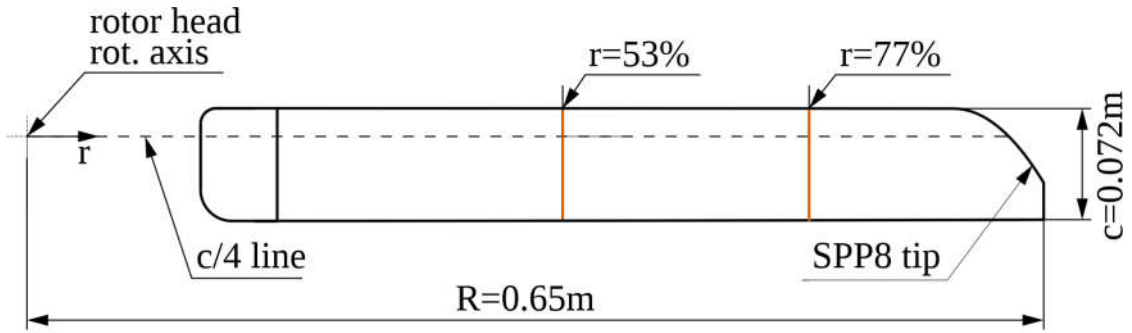


Figure 3.4: Schematic sketch of the rotor-blade geometry.

Similar to real helicopter configurations, the blade tips are parabolic shaped, see Fig. 3.4, reducing the chord length at the blade tip to $c_{\text{tip}} = 0.024$ m. The parabolic tip shape is an SPP8 blade-tip shape without sweep and anhedral; see Refs. [2, 113]. The blade is, as in helicopter related fields common, negatively twisted towards the tip. Figure 3.5 displays the linear twist against the span. The angle at the root is defined as zero. The range from $r/R = 111/650 \approx 0.17$ up to $r/R = 160/650 \approx 0.25$ is not profiled and serves as the clamping area. The first profiled section is already declined by $\Delta\Theta = -2/3^\circ$. The subsequent linear decrease has a gradient of approximately 19°

Table 3.1: Parameters of experiment and simulation.

Parameter	Values
Chord, c	0.072 m
Radius, R	0.65 m
Airfoil	DSA-9A
Tip Mach-number, M_{tip}	0.28
Tip Reynolds-number, Re_{tip}	470 000
Tip speed, U_{tip}	96.4 m/s
Rotational speed, Ω	23.6 Hz

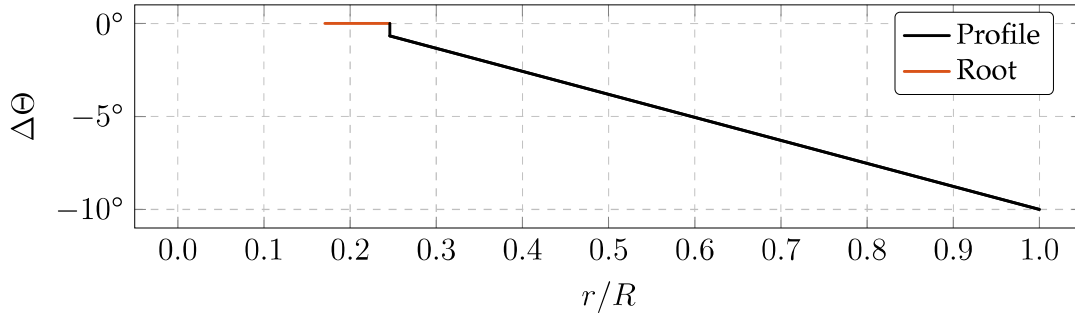


Figure 3.5: Twist distribution of the rotor blade.

per meter, leading to a root tip difference of $\Delta\Theta = 10^\circ$.

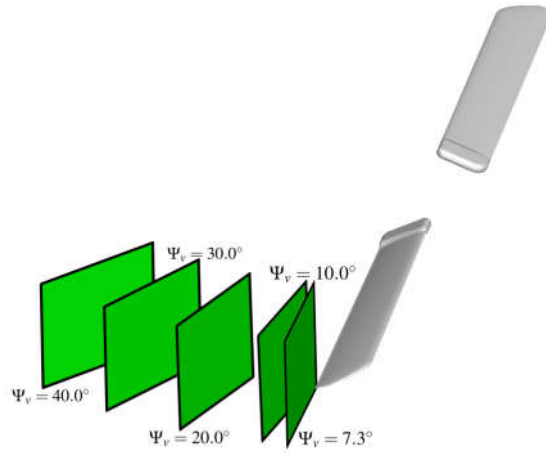


Figure 3.6: PIV planes at the RTG at the DLR in Göttingen.

Low-speed PIV was performed on the wake of the rotor using a stereoscopic setup. Figure 3.6 shows some investigated PIV planes which are marked with the wake age referenced to the $c/4$ line ($\Psi = 0^\circ$). This nonintrusive technique records pictures of uniformly seeded flow. Two cameras in a stereoscopic setup took images; thus, all three velocity components could be extracted. Schwermer et al. [90] give detailed information on the RTG and show experimental results. The PIV results have been analyzed and published by Braukmann et al. [15]. First experimental results at the rotor test facility (RTG) at the DLR in Göttingen were presented by Schwermer et al. [90], who analyzed dynamic stall experimentally. The corresponding numerical investigations of the stiff blades have been carried out by Letzgus et al. [59], resulting in good agreement with the experiment. The PIV setup used in the current study is similar to that described by Wolf et al. [117] and Braukmann et al. [14]. Stereo-PIV provided the three-component velocity vectors in a measurement plane, which is approximately normal to the axes of the blade-tip vortices, enabling a study of both swirl velocity and circulation. The region of interest extends $1.8c$ in the direction of

the rotor axis and $2.1c$ in the spanwise direction. The PIV data was evaluated using iterative cross-correlation algorithms and the commercial software LaVision DaVis 8.4. The resolution of the final grid is about 4.2 data points per mm.

3.3 Coordinate systems

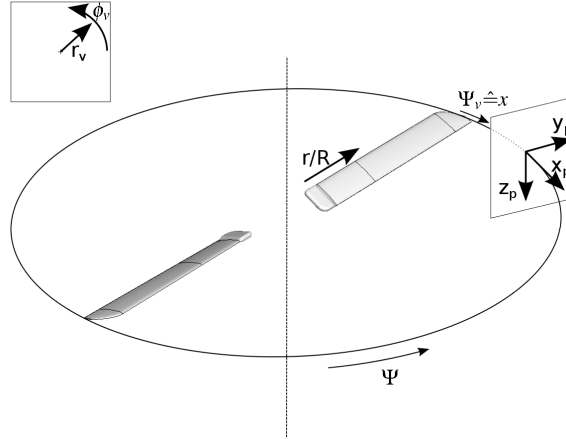


Figure 3.7: Coordinate systems employed in this study.

Two coordinate systems are used in this study and are shown in Fig. 3.7. Some results are expressed in planes captured by the PIV system. They correspond to planes that cut the rotor hub on the $c/4$ line and are rotated around the rotor axis by the wake age, as depicted in Fig. 3.6. The origin of this coordinate system with the subscript p is on the circle, which is described by the rotation of the blade tip. The planes follow the rotor blade and are described by their curved distance x/c or Ψ_V behind the rotor blade. This coordinate system consists of an x_p -, y_p - and z_p -axis. The x_p -axis points away from the blade. The vorticity of the blade-tip vortex is positive in this coordinate system. The y_p -coordinate points outboard. Therefore, a vortex movement towards the root results in negative y_p -values. The z_p -axis complements the right-hand system and points accordingly downward.

The two-dimensional vortex coordinate system is a translated and transformed polar description of the y_p and z_p plane of the p -coordinate system. The origin of this v -coordinate system is the center of the vortex core. The radial axis r_v is pointing outwards. The azimuthal axis ϕ_v is mathematically positive defined and starts on the right-hand side when looking towards younger wake ages. Therefore, a value of $\phi_v = 0^\circ$ corresponds to the y_p -axis.

Table 3.2 shows a conversion chart of the wake age, which is defined in two ways: The first column states the azimuthal distance in degree between the considered

Table 3.2: Conversion of vortex age.

Ψ_V in $^\circ$	x/c
0.0	0.0
2.6	0.41
5.3	0.84
15.3	2.42

measurement plane and the trailing edge of the vortex generating blade. The second column is the curved distance x up to the trailing edge normalized by the chord length c .

Figure 3.8 shows some example slices for vortex analysis. Two variable techniques arise due to different experimental methods. All slices cut the blade-tip path nearly perpendicular, and the alternating effects tend to be negligible. The wake age of each slice corresponds to the angle towards the trailing edge of the blade. Slices that are depicted with solid lines are mainly used in chapter 4. These slices cut the rotational axis at $x/c = 0.25$ and $y/R = 0$. However, the slice with the youngest wake age $\Psi_V = 2.6^\circ$ is created by a plane that is parallel to the trailing edge with a separation of 8 mm and then rotated by 1.8° . The defining process of the dashed slices of the four-bladed configuration in chapter 5 is different, as the original plane was aligned on the trailing edge and then rotated by the wake age.

3.4 Vortex analysis

The vortex models from the literature are covered in section 2.2. A broad range is covered by an algebraic model of Vatistas et al. [110], which fits other models by tuning the parameter n . Ramasamy & Leishman [81] have created a new parametric mathematical formulation to cover an extensive scope of vortex Reynolds-numbers with up to six fit coefficients. Furthermore, vortices can be divided into a wake-like or jet-like appearance depending on the axial velocity of the vortex. A wake-like vortex is defined as a vortex with an axial core velocity lower than the surrounding velocity U_∞ leading to a velocity deficit, whereas a vortex with an axial core velocity higher than U_∞ defines a jet-like behavior. For rotating blades with negligible inflow, as investigated here, the definitions are transformed into the p -coordinate system. If the axial velocity u_p is positive, a jet-like behavior is derived, as the flow pushes in the opposite direction of the blade. A wake-like behavior exists if the axial velocity u_p is negative since the blade accelerates the flow in the direction of the movement of the blades.

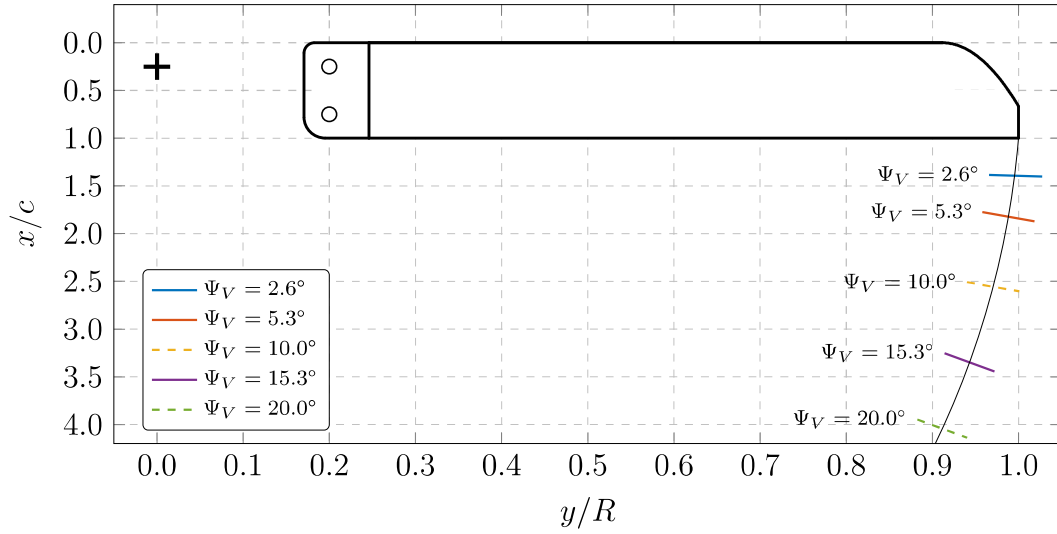


Figure 3.8: Example slices for vortex analysis.

The vortex characteristics can be investigated from the CFD volume solution, analogous to the PIV analysis presented by other authors [14, 118]. The experimental data is derived by planes in the three-dimensional field with in-plane and out-of-plane velocity components, according to Fig. 3.6. To take the aperiodicity of the vortex into consideration, all velocity maps were collocated with the vortex core center before further analysis. The data evaluation of the PIV planes is further described by Braukmann et al. [15]. To ensure a valid comparison between the numerical and experimental data, two-dimensional cuts across the tip vortex in the CFD simulations were extracted.

The density was fitted to the density distribution after Bagai & Leishman [4] of the vortex model ($n = 2$) of Vatisstas et al. [110] to define the position of the vortex center. The fitting of the vortex model allows a new sub-grid accuracy for the vortex position. The alternative, seeking the centroid of the area weighted by the λ_2 value, results in similar values. The numerical results were then interpolated onto a Cartesian grid around the estimated vortex core in the wake plane. Once the position has been defined, all investigated parameters like swirl-velocity distribution, radius, circulation, and the shape of the vortex core can be extracted.

After the collocation of the vortex cores, the swirl velocity is obtained with a binning procedure. The method which is employed in the analysis of the experimental and numerical data is a binning of the already existing grids into annuli of equal thickness. All points which fall into one circular bin are combined to a mean swirl-velocity leading to a distribution over a radial coordinate. Due to noncircular vortices, this method can smear out aerodynamic effects, but the results are comparable. This method is used when the radius between experimental and numerical results

are compared. The radius of the vortex core is defined as the radial position with the highest swirl velocity. The maximum of the azimuthal-averaged swirl-velocity specifies the experimental and numerical radius.

An additional method, which is feasible for CFD data, extracts the shape of the vortex core. Two-dimensional cuts are extracted normal to the path of the blade-tip vortex, similar to PIV planes. The center of the vortex core is defined by the centroid of the lowest λ_2 value. Both methods (λ_2 and density fit) lead to similar results and do not differ significantly. Radial cuts are then extracted radiating star-like from the center with a resolution of $\Delta\Psi = 2^\circ$ (180 cuts). This is similar to an interpolation of the domain onto a polar coordinate system defined by the vortex core. The vortex core radius is then investigated for every radial cut accounting for non-circular vortices by extracting the position of the peak swirl-velocity. The information of all cuts defines the vortex-core shape. The shape is further analyzed by fitting an ellipse onto it. This method could also be used for extracting the mean radius as Ramasamy et al. [78] noted that two orthogonal cuts are sufficient to determine a mean value of the radius if the core seems elliptical. Although both methods show only small differences in the numerical results, to maintain comparability with the experimental data, this method is used for plotting CFD results only, like the shape and the parameters of the ellipse.

The circulation Γ is proportional to the product of the swirl velocity v_ϕ and the radius r since it is the line integral ds around a closed curve of the velocity field v , as already shown in chapter 2. If the mean of a radial bin Σv_{ϕ_i} has already been extracted, the distribution of the circulation can be derived by multiplying the swirl velocity with the corresponding radius:

$$\Gamma = \oint v ds = 2\pi \cdot \Sigma v_{\phi_i} \cdot r \quad (3.1)$$

The bound circulation distribution on the blade is determined by the integration of the surface pressure distribution at each radial station and azimuthal position. The circulation is estimated with the Kutta-Joukowski theorem, which relates the lift of a two-dimensional airfoil to the circulation; see equation (2.2) on page 7. Strictly speaking, this theorem is only correct for steady and inviscid flows, but it still gives a useful approximation of the bound circulation on the blade for the relatively low reduced frequencies considered. The radial distribution of the gradient of the circulation can be integrated to estimate the strength and position of the departing blade-tip vortex. The vortex moves to the location of the spanwise centroid of vorticity; see Refs. [6, 86]. Hoffmann et al. [39] analyze the effects of active twist control on the bound circulation and vortex formulation. They introduce the area outboard of the

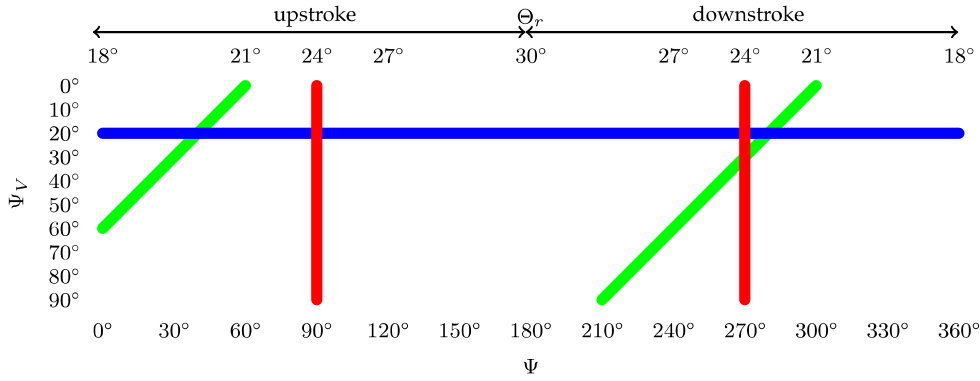


Figure 3.9: Visualization of different vortex analysis methods.

maximum as the radial area of vortex formation. The position of the vortex is defined in the center of gravity of the circulation distribution. Komerath et al. [53] sum up diverse observations and experiments. They see blade-tip vortex circulation values up to 100% of the peak bound circulation at the trailing edge. In addition, they observe a loss of about half the circulation after aging for 48° because of the fluid being pushed inboard due to the axial deficit.

The analysis of the unsteady vortex is rather difficult since the vortex line consists of a vortex-slice combination at each time instant. All of these vortices have varying wake ages and were produced at different blade angles. Similarly, following a single moving vortex slice at a constant distance behind the blade in time will result in a varying vortex. The propagation rate was simplified, assuming that the vortex slice stayed at a constant azimuthal angle in the laboratory frame with propagation downward and towards the rotor axis.

Figure 3.9 shows three comparison methods to analyze the influence of the pitching motion on the wake. On the horizontal axis, there is the wake's azimuthal position, which corresponds to a certain angle of incidence at vortex creation, which is shown on the upper horizontal axis. The vertical axis displays the increasing wake age of 0° - 90° from top to bottom. The three colored lines each represent a different way of looking at the vortex system and will be used when showing unsteady results. The numerical solver supplies solutions of a fixed time instant. The green lines (—) represent this numerical approach. If the vortex at a constant wake age is considered, many instantaneous solutions are required, and the blue line (—), here at $\Psi = 20^\circ$, results. The final approach follows the evolution of a vortex slice produced at a particular instant as it convects downstream of the blade, producing the vertical red line (—) in Fig. 3.9.

3.5 Error analysis

The vortices are detected by extracting two-dimensional cuts normal to the path of the blade-tip vortex. Then the density distribution is fitted, or the centroid of the area weighted by the λ_2 value is looked for. These first steps influence the entire data evaluation. Therefore, the algorithms should be robust without introducing significant errors. Figure 3.10 shows the vortex core resulting from two different vortex-center (VC) positions. The red points will display the situation if the center is detected correctly found. A wrong center with an offset of half the radius ($y_p/c = 50\%$) leads to the blue points. The absolute position of the detected vortex core edge is virtually unchanged since all cuts hit the peak swirl-velocity eventually. The dashed lines comprise a quarter of all cuts and, hence, contain a quarter of all found values. If the center has an offset, those values close to the edge will dominate the computation of the mean value. The other side with higher values is less dense and not as dominating. Therefore, the positional error of the center results in an error of the mean core radius, which depends on the aspect ratio of the long and short axes of the elliptical vortex b/a . The shown case leads to an error of the mean radius above five percent.

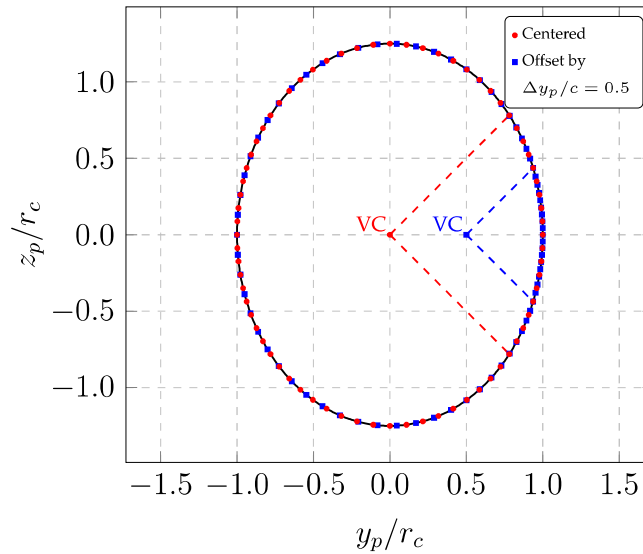


Figure 3.10: Extracted vortex core with two different center positions.

This error analysis is done for three different vortex forms (b/a) and a varying offset of the center position. The resulting error of the averaging is shown in Fig. 3.11. The error of the radius stays below 0.25% with a given offset in any direction of 10%. Even an offset of 20% only leads to an error of approximately 1%. Thereby, the error analysis proves the robustness of the implemented algorithm.

The vortex-core shape is still correctly extracted, even if the center is mistaken in

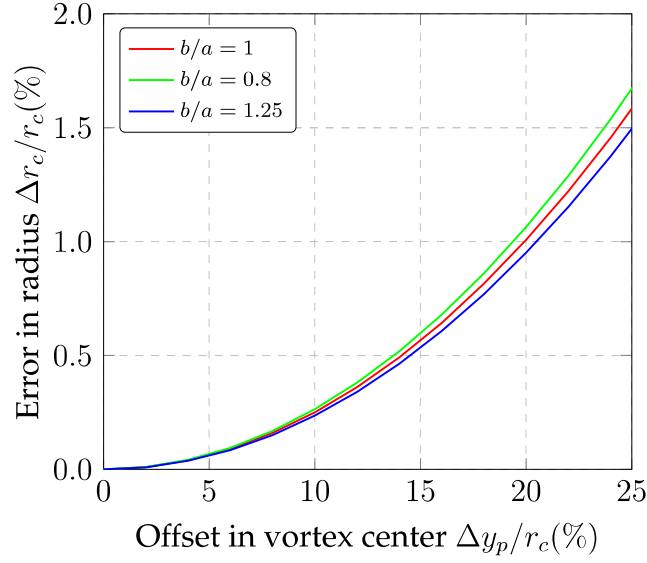


Figure 3.11: Influence of offset in center position on radius.

the first place. Assuming the center has an offset of 10%, as shown with dashed lines in Fig. 3.12, and the radial velocity is negligible ($v_r \ll v_\phi$). The resulting orthogonal angle difference reaches a maximum of $\arctan(0.1) \approx 5^\circ$. This difference leads to a varied swirl velocity by only $\cos(5^\circ) \approx 0.5\%$. The diminution, however, does not change the location of the maximum, which means that the vortex-core shape is not significantly affected by an offset of the center position.

The computation of the swirl velocity requires a correction of the convection velocity due to the vortex movement if only one cut is taken. Figure 3.13 shows the azimuthal variation of the swirl velocity of a blade-tip vortex at $\Psi_V = 10^\circ$ with a constant angle of incidence of $\Theta_r = 24^\circ$. The correction does not influence the mean swirl-velocity since all cuts are evenly distributed, and the correction adds up vectorially. Hence, a correction is not necessary to obtain the mean swirl-velocity. Additionally, a particular problem is the interaction between the vortex and the wake sheet of the blade, seen as a bump in the single cycles between $0.15 < r_V/c < 0.35$ in Fig. 3.13. In this study, 90 through-cuts (180 star-cuts) are used even though Ramasamy et al. [78] suggest that extracting two through-cuts (four star-cuts) and then averaging the four values of the radius core provides a good estimate of the mean radius. However, this study analyzes also the shape of the vortex core, for which those 90 through-cuts are required. Figure 3.14 shows the error in the mean radius due to only taking two cuts for an unsteady case with $\Theta_r = 24^\circ - 6^\circ \cos(2\pi t/T)$. All possible cut directions are analyzed with some cuts over- and some underpredicting the radius. The highest discrepancy above and below the mean are shown in Fig. 3.14.

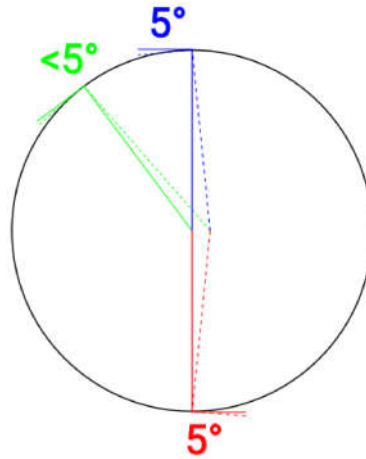


Figure 3.12: Resulting error of swirl velocity due to wrong center position.

It can be seen that the maximum over- or underprediction of the mean radius is less than 3% for wake ages older than $\Psi_V = 20^\circ$. For very young wake ages, the error can exceed 5%.

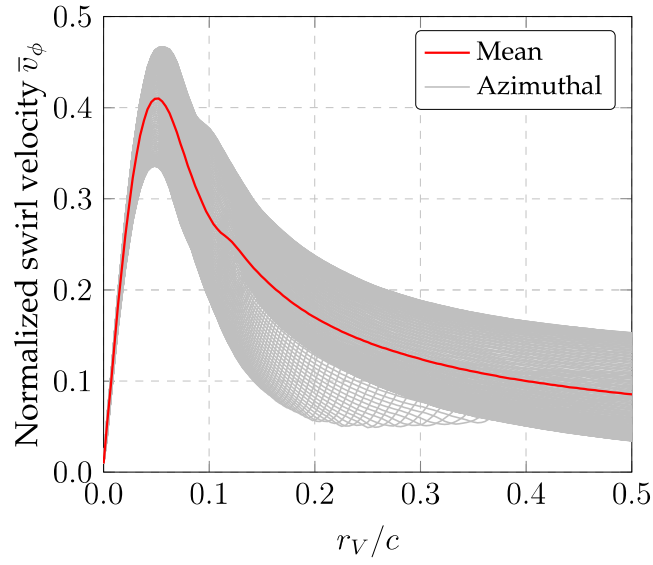


Figure 3.13: Azimuthal variation of swirl velocity ($\Theta_r = 24^\circ$; $\Psi_V = 10^\circ$).

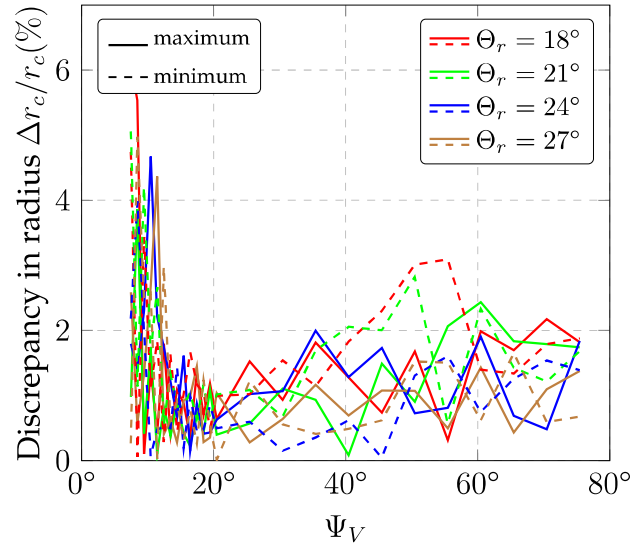


Figure 3.14: Discrepancy due to two orthogonal cuts (— = maximum; --- = minimum)

4 Blade-tip vortices of a two-bladed rotor¹

This chapter focuses on the investigations of a pitching two-bladed rotor. First, the results of a grid and time-step sensitivity-study are shown. Comparisons with the experimental load characteristics follow. The main part is about general aspects and other vortex parameters including, circulation, radius, azimuthal analysis, position, and pressure of the vortex core. The chapter is finished about the effect of rotation by comparing results with nonrotating data from the literature.

4.1 Numerical setup of the two-bladed rotor

The following aspects describe the utilized grid of the two-bladed rotor, which is covered in this chapter. The numerical simulations are performed using the DLR-TAU [87] code. The URANS equations are closed by the Menter-SST turbulence model [65]. The unstructured hybrid grid is generated using CENTAURTM [19] and consists of three grid blocks connected by the grid overset method. The computations are second order in space and time; the inviscid fluxes were solved by a central method. The numerical setup corresponds to a simplified experimental setup. The two rotor blades are modeled as stiff blades, and a far-field free-stream condition is implemented in a spherical computational domain with a radius of 900 blade spans. Figure 4.1 shows a top view of the planform of the utilized blade. Both axes are nondimensionalized with c and R , respectively. The scaling maintains the original axis ratio. The highlighted root part starting from $y/R = 160/650 \approx 0.25$ has no aerodynamic profile but is considered in this chapter. Both blades consist of the same surface and boundary layer grid. The surface grid is refined in the tip area up to

¹Text and illustrations from this chapter appear in: A. Goerttler, J. N. Braukmann, T. Schwermer, A. D. Gardner, and M. Raffel, "Tip-Vortex Investigation on a Rotating and Pitching Rotor Blade", *Journal of Aircraft*, Vol. 55, No. 5, 2018, pp. 1792-1804, DOI: [10.2514/1.C034693](https://doi.org/10.2514/1.C034693), (Ref. [32]).

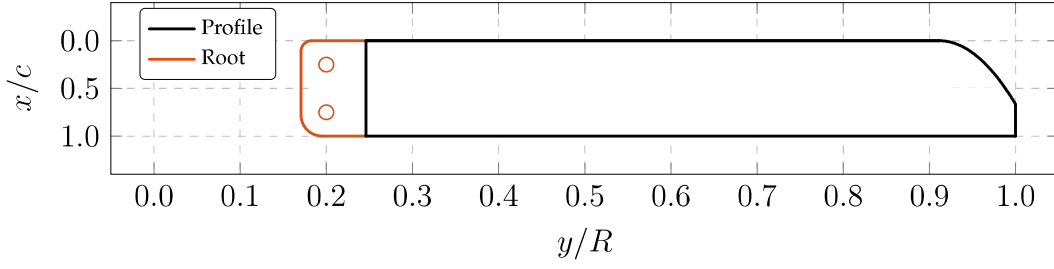


Figure 4.1: Planform of the rotor blade.

$s/c = 0.0034$. The hybrid grid consists of 30 prisms in the direction normal to the surface. The first cell height is set to $y^+ \sim \mathcal{O}(1)$, and a stretching factor of 1.2 is used to resolve the boundary layer. The area behind the trailing edge at the tip of one blade was further refined to resolve the tip vortex. Early models by Landgrebe [55] and experiments by Kim et al. [49] concluded that only the part of the vortex sheet outboard of the maximum lift on the blade is entrained in the blade-tip vortex. Since structured cells have less numerical dissipation, a hexahedral block, see Fig. 4.2(a), fitted to the tip path was constructed like Braun et al. [16] did for their investigations. The edge lengths of the hexahedra are $s/c = 0.0034$, leading to 7.2 million hexahedral cells only in the small structured block. Due to high computational effort, this fine resolution was only maintained up to around $\Psi = 18^\circ$, which corresponds to $x/c \approx 2.7$ behind the trailing edge. In order to smooth the transition to the unstructured area, there is a helical tube with tetrahedral cells, having the same edge length as the hexahedral cells, around the block. The tube is positioned where the blade-tip vortex is expected. If not otherwise stated, the simulations in this chapter were run with a vortical correction like Brandsma et al. [13]. This correction reduces the viscosity and therefore delays dissipation [115]. The top view in Fig. 4.2(b) shows a slice through the $c/4$ -line, and Fig. 4.2(c) shows the surface grid at the blade tip. A test case that causes dynamic stall was investigated, with sinusoidal pitching at $\Theta_r = 23.7^\circ \pm 6^\circ$.

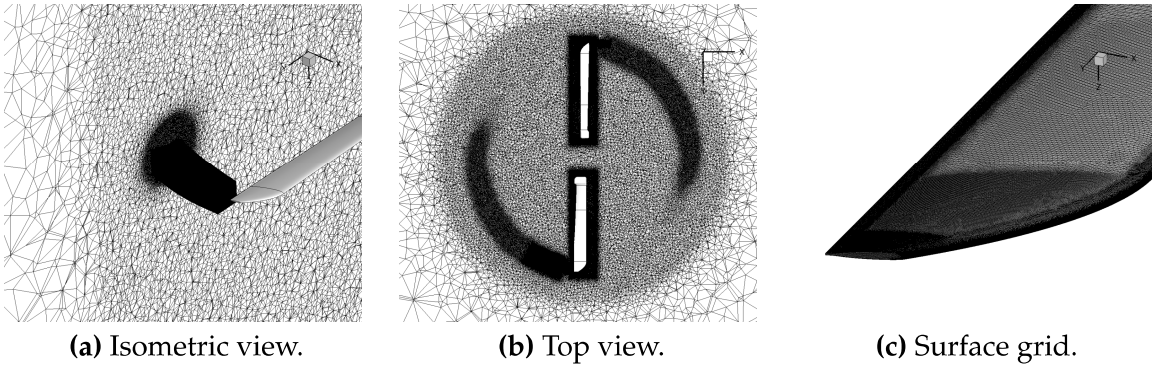


Figure 4.2: Numerical grid of the two-bladed rotor.

4.2 Grid and time-step sensitivity

A grid and time step sensitivity study was carried out numerically. The grid study focused on the behavior of the tip vortex by comparing the experimental data with three simulations of different numerical grids. Table 4.1 lists the edge length of the refined area and the number of nodes of the investigated background grids. One complete unstructured background grid and two grids with a refined block consisting of fine hexahedral cells were compared, focusing on the length of the cells in the blade-tip region.

Table 4.1: Parameters of the background grid.

	$s/c \cdot 10^2$	node no. (million)
CFD unstruct. base	0.69	6.4
CFD struct. base	0.69	4.4
CFD struct. fine	0.34	13.4

Figure 4.3 shows the velocity distribution of the blade-tip vortex at $\Psi_V = 2.6^\circ$ ($x/c = 0.39$) behind the blade for attached flow during the upstroke motion. Table 4.1 list the different grid attributes of the background grid, which are compared with the experiment. The peak swirl-velocity in the experiment at $\Theta_{\text{root}} = 29.55^\circ$ is found at $v_\phi/U_{\text{tip}} \approx 0.77$ at a nondimensional radial distance just below $r_v/c = 0.07$, which corresponds to approximately 5 mm. The corresponding blade-load coefficient amounts to $C_T/\sigma \approx 0.18$ in the numerical simulations. Both solutions with a structured hexahedral block predict a slightly larger radius at $r_v/c = 0.075$, with varying peak swirl-velocities. The fine grid yields the highest swirl velocities and matches the experimental data best. Both “base” grids underestimate the swirl velocity with the same vortex core radius as the fine grid. The unstructured grid yields almost the same swirl velocity even though it has with $6.4 \cdot 10^6$ more nodes than the structured grid with $4.4 \cdot 10^6$ nodes. All simulations match each other outside the vortex core. Although the differences between the simulations at this young wake age are small, all further investigations were performed with the finest grid to assure similar agreement at more advanced wake ages.

Figure 4.4 shows a study of the time discretization. There are still changes in the thrust coefficient after increasing the number of time steps from 360 ($\Delta\Psi = 1.00^\circ$) up to 1440 ($\Delta\Psi = 0.25^\circ$). Kaufmann et al. [45] used up to 3000 time steps for their pitching period, whereas Letzgs et al. [60] concluded a time step study on their rotating blade

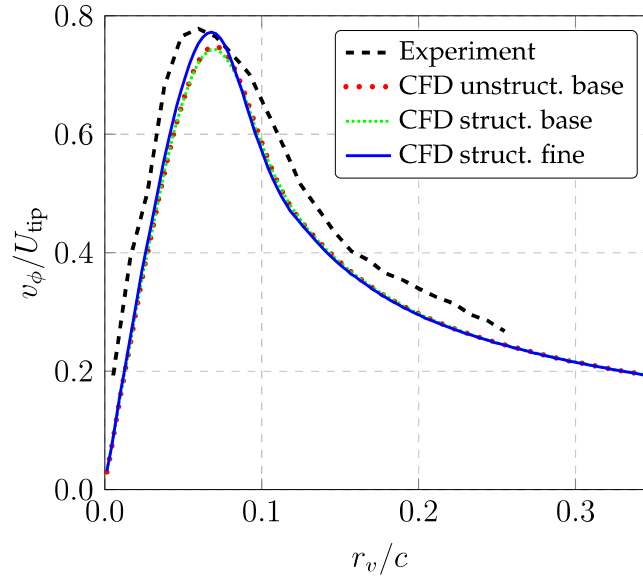


Figure 4.3: Swirl velocity of the blade-tip vortex at $\Psi_V = 2.6^\circ$ ($x/c = 0.39$) behind the blade for different grids, $\Theta_r = 29.55^\circ$.

resulting in 1440 time steps. The solutions with 200 or 400 inner iterations predict both the overshoot at the highest angle of incidence and match sufficiently each other during the upstroke. The time step of $\Delta\Psi = 0.25^\circ$ (1440 time steps per period) with 400 inner iterations is therefore used for all following computations.

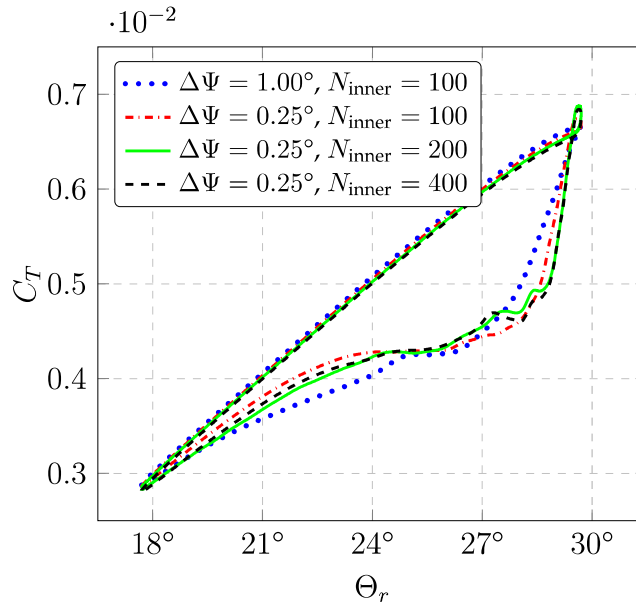


Figure 4.4: Thrust coefficient of CFD simulations with different temporal resolution.

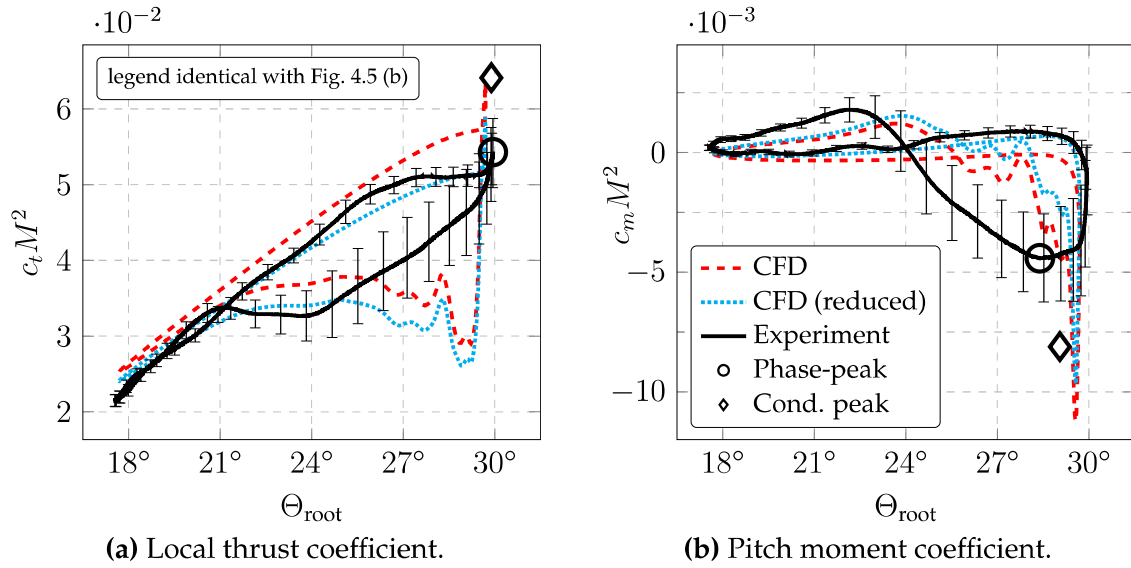


Figure 4.5: Dimensionless coefficients at $r/R = 0.77$.

4.3 Load characteristics

Figure 4.5 shows both the local lift and moment coefficients integrated from pressure sensors at $r/R = 0.77$ over a full period. The CFD data has additionally been integrated with reduced points corresponding to the experimental sensor positions. Particularly at the lowest angle of attack, the effect of the free boundary layer transition in the experiment leads to differences in the lift compared with the fully turbulent CFD. In the CFD results, there is a sudden drop at the highest angle of attack, which results in a sharp moment coefficient minimum. The numerical simulation overpredicts the lift hysteresis, which leads to an overprediction of the moment coefficient minimum since the separation in the experiment is less pronounced. However, averaged unsteady experimental data draws only an incomplete picture, as Ramasamy et al. [82] illustrated. Thus, the peak and its position of the conditional average are shown. The numerical results depict these increased values better. The behavior between the experiment and CFD simulation is similar and should be sufficient to compare the blade-tip vortices during the upstroke.

4.4 General aspects of blade-tip vortices

Figure 4.6 shows instantaneous isosurfaces of the λ_2 -criterion [43], which are colored with the vorticity perpendicular to the wake plane at three different stages during the upstroke motion. Red and green colors represent positive vorticity values; thus, the

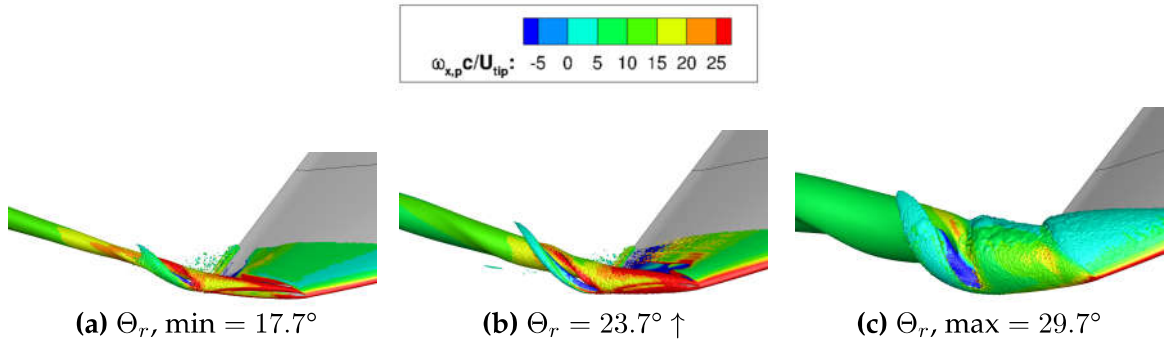


Figure 4.6: Isosurfaces of λ_2 criterion, colored with rotationwise vorticity.

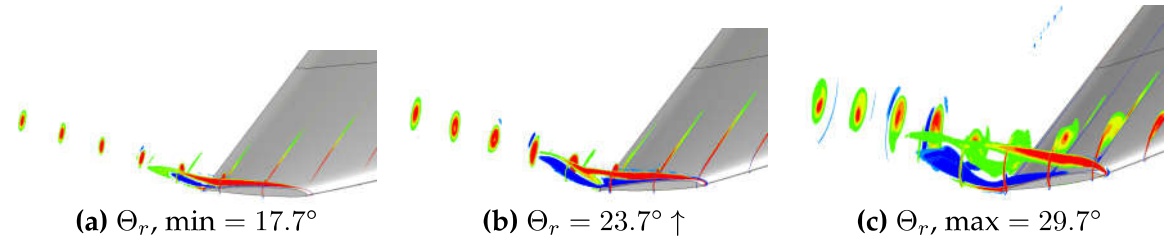


Figure 4.7: Slices at the blade tip, colored with rotationwise vorticity.

expected rotation of the blade-tip vortex due to the pressure difference between the upper and lower surface. Blue colors indicate a counter-rotating vortex with negative vorticity values. Overall the size of the blade-tip vortex increases with increasing angle of incidence. At the highest angle of incidence, see Fig. 4.6(c), the blade-tip vortex moves inboard of the blade tip, as also seen by Kaufmann et al. [47] for a nonrotating case.

Figure 4.7 highlights the formation of both rotational motions by showing vorticity colored slices. At the lowest angle of incidence, see Fig. 4.7(a), a domain of negative vorticity values extends from the position of the trailing edge. This area is then entrained by the primary vortex, and a positive global rotation is imposed on it. At higher angles of incidence, see Fig. 4.7(b) and Fig. 4.7(c), negative vorticity already occurs on the upper surface of the blade. The primary blade-tip vortex evolves at the blade tip and lands on the upper surface further inboard than at a lower angle of incidence. The blade-tip vortex indicated by red and green colors does not follow the blade surface. Instead, it is driven by the inflow due to the rotation of the blade and therefore separates from the blade-tip surface right after the leading edge.

4.5 Circulation

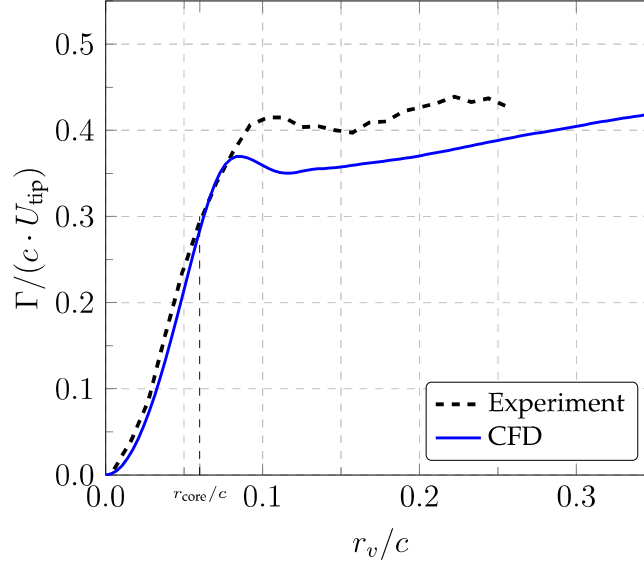


Figure 4.8: Circulation of the blade-tip vortex at $\Psi_V = 2.6^\circ$ ($x/c = 0.39$) behind the blade for CFD simulation and experiment [15], $\Theta_r = 29.55^\circ$.

The circulation is derived, as described in the vortex analysis section on page 39. The amount of circulation correlates to the lift generated since parts of the produced lift merge into the growing blade-tip vortex according to the theorems by Helmholtz and Kutta-Joukowski. The distribution of the circulation of a blade-tip vortex, see Fig. 4.8, starts at zero in the center, and after a short and rapid increase, it approaches the total circulation asymptotically. The closer the integration window size is to the vortex core, the better the match in integrated vorticity between the experiment and the simulation. Figure 4.8 shows good agreement between experiment and CFD up to $r_v/c = 0.08$, after which there is a constant offset between those two methods. The small decay after the local maximum at around $r_v \approx 0.1$ is the result of the counter-rotating vortex, see Fig. 4.6, as already shown by Kaufmann et al. [47]. Wolf et al. [118] identified $r_v = 0.2c$ as a suitable value of a constant radial distance for the evaluation of the circulation. This circulation $\Gamma_{0.2c}$ is a good substitute for the total circulation. The CFD data shows that the circulation is still increasing at that border, but to compare with the experimental data, which is limited by the PIV region, this constant radial distance is chosen for the evaluation of the circulation.

Figure 4.9 shows the circulation of the blade-tip vortex at a constant radial position $r_v = 0.2c$ away from the vortex core over the angle of incidence of the root at the formation time of the vortex. The circulation is normalized by the chord length c and

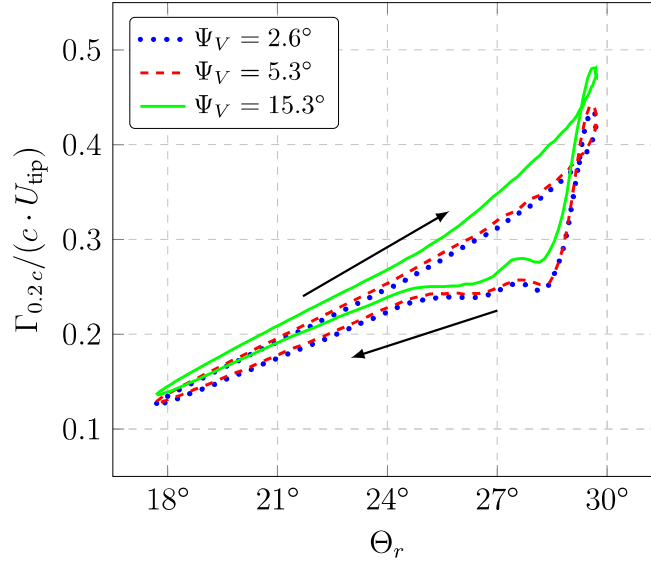


Figure 4.9: Circulation of CFD simulation at constant radial distance $r_v = 0.2c$ for different wake ages.

the blade-tip velocity U_{tip} . It is noticeable that during the upstroke, the gradient is fairly constant up to $\Theta_r \approx 25^\circ$. At larger angles of incidence, the circulation does not increase linearly anymore. The highest gradient is reached by the oldest wake age shown ($\Psi_V = 15.3^\circ$). The shape of these graphs is of a similar shape as the lift coefficient in Fig. 4.5, but with lower hysteresis. Around the highest angle of incidence, the circulation still increases during the downstroke motion until a sudden drop appears. The circulation is higher at more advanced wake ages since the blades wake-vorticity of the part outboard of the maximum in lift is entrained.

Figure 4.10 shows a comparison of the blade-tip vortex circulation and the lift coefficient by plotting the ratio Q , see equation (4.1), of the circulation $\Gamma_{0.2c}$ to the lift coefficient $c_l M^2$ at $r/R = 0.77$ scaled by the ratio $Q_{\Theta_{\min}}$ at $t/T = 0$.

$$Q = \frac{\Gamma_{0.2c}}{c_l M^2} \cdot \frac{c_l M^2(\Theta_{\min})}{\Gamma_{0.2c}(\Theta_{\min})} \quad (4.1)$$

The x -axis shows again the angle of incidence at the formation of the vortex and not the angle of incidence at that time. The scaling sets the ratio $Q = 1$ at $t/T = 0$. Again up to half the upstroke ($\Theta_r \approx 25^\circ$), the ratio Q stays almost constant for all three wake ages. It should be noted that due to different circulation values within the wake ages, all three curves are separately scaled, and the curves, therefore, only state the relation between the lift coefficient and the blade-tip vortex circulation. At angles of incidence larger than $\Theta_r \approx 25^\circ$, the ratio slightly increases to values $Q > 1$. At the maximum angle, the ratio exceeds $Q > 2$ meaning, the ratio between the vortex circulation and lift is twice as high as the ratio at the minimum angle of incidence.

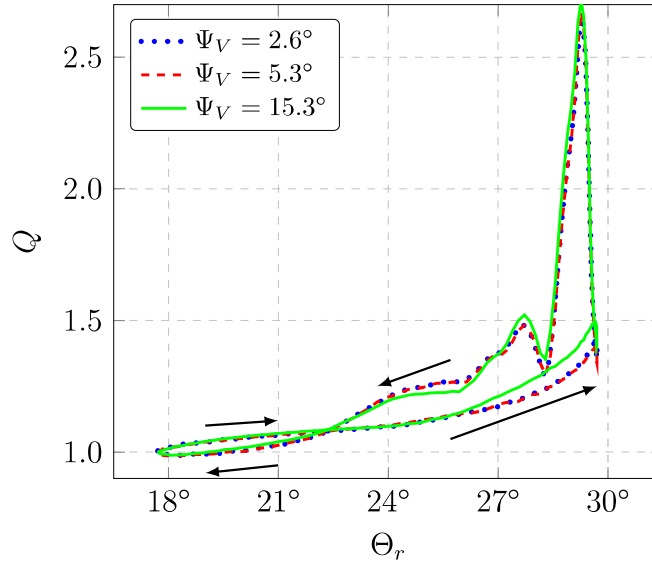


Figure 4.10: Comparison between tip vortex circulation and lift coefficient at $r/R = 0.77$ of CFD simulation.

This value eventually reduces and after reattachment returns to $Q \approx 1$. This was already observed by Wolf et al. [118] in the nonrotating version of this experiment with a pitching blade. The blade-tip vortex has a stabilizing effect on dynamic stall as it delays separation on the blade tip. The lift coefficient drops after the highest angle of incidence resulting in a decreasing denominator of Q and, therefore, an increasing Q . The half width of this peak is the time shift between those two drops and is $\Delta\Theta_r \approx 0.4^\circ$. This corresponds to a delay of almost five percent in the period ($\Delta\Psi \approx 18^\circ$). After the peak of Q , the vortex circulation starts then to decrease, which reduces the counter of Q and, therefore, Q as well.

Figure 4.11 shows the circulation of the blade-tip vortex for the experiment and numerical simulation at the wake age $\Psi_V = 2.6^\circ$. The two upper lines are derived by the line integral at the constant distance of $r_v = 0.2c$. The CFD simulation slightly underestimates the circulation measured in the experiment. Nevertheless, the overall trend is in good agreement, except for the dynamic stall region at $0.5 < t/T < 0.75$, where the numerical and experimental loads do not match well. The underestimation at this constant radial distance can mostly be explained by different vortex radii. If the circulation is integrated out to the edge of the vortex core, the experiment and its simulation agree very well during the attached upstroke ($0.2 < t/T < 0.45$). However, the underestimation at $r_v/c = 0.2$ and the constant offset after $r_v/c = 0.08$ in Fig. 4.8 lead to the conclusion that in addition to the vortex-core size, the swirl-velocity distribution also differs between experiment and CFD. In the domain $t/T < 0.2$, the two methods do not match anymore since the radius could not be predicted very

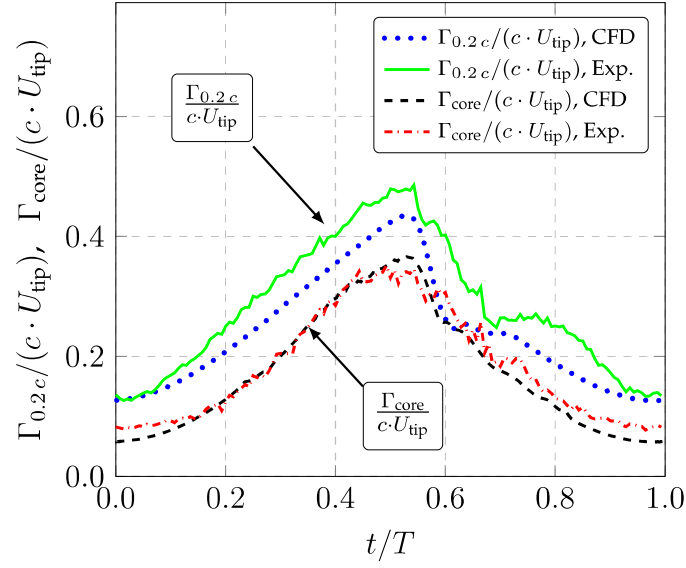


Figure 4.11: Circulation of the experiment [15] and CFD simulation at two different radial stations for $\Psi_V = 2.6^\circ$.

well in the experiment due to a limit in the PIV resolution. Limitations of the PIV technique to measure helicopter blade-tip vortices are described by Raffel et al. [76] and references therein.

4.6 Radius

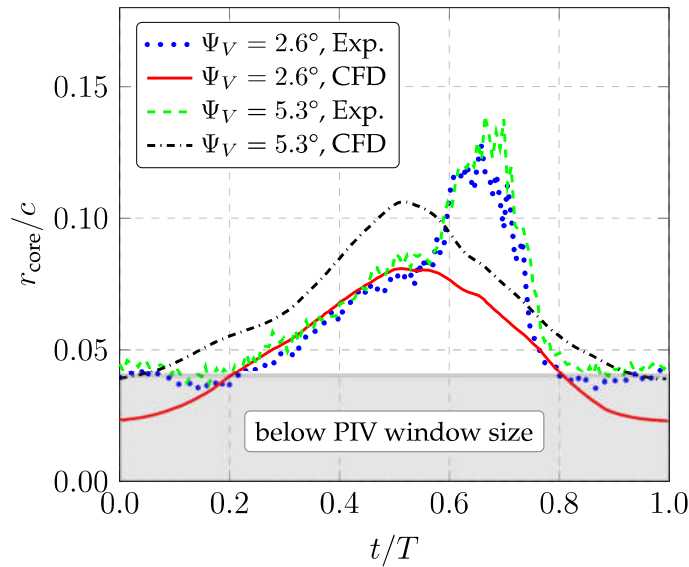


Figure 4.12: Vortex radius for experiment [15] and CFD simulation at two different wake ages.

Figure 4.12 depicts the vortex radius for a full cycle at several planes behind the blade. The radius grows during the upstroke since more generated lift results in a stronger and larger vortex. A small hysteresis is existent since the radius is bigger during downstroke than during upstroke compared at the same angle of incidence. There is almost no increase in the experimental results of the vortex core radius identifiable between the wake ages $\Psi_V = 2.6^\circ$ and $\Psi_V = 5.3^\circ$, whereas due to numerical diffusion, the radius of the vortex in the numerical data increases. With increasing vortex age, the results of the numerical simulation drift away from the experimental data. The numerical data at $\Psi_V = 2.6^\circ$ matches the experimental radius in the upstroke motion up to $t/T \approx 0.5$ well, but during dynamic stall, the results diverge. The experiment shows a sudden increase in the radius, whereas the numerical data shows a smooth decrease. Braukmann et al. [15], however, state that during the stall conditions, high fluctuations and low swirl velocities lead to difficulties in detecting the radius in the experimental data. After reattachment, the two methods approach each other again. The radius in the CFD data underpredicts the experimental data around the lowest angle of incidence ($t/T < 0.2$ and $0.8 < t/T$). In this area, the CFD simulation states the radius to be $r_{\text{core}}/c < 0.05$. This is below the spatial PIV resolution and, therefore, the limit of the experimental detection of the vortex core. Structures smaller than the window size cannot be correctly resolved by PIV.

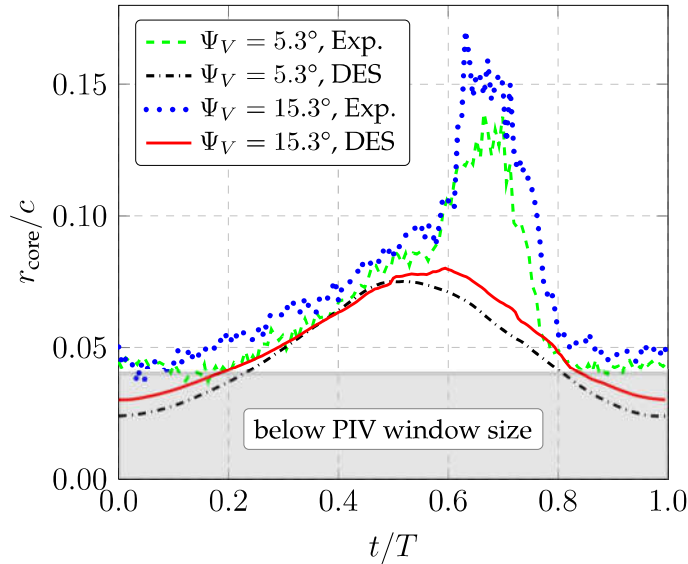


Figure 4.13: Vortex radius for experiment [15] and CFD simulation with a DES approach at two different wake ages.

Figures 4.11 and 4.12 reveal that the grid or turbulence model could not correctly predict the changing strength and radius of the blade-tip vortex with time and position. A grid refinement study concludes that there is still too much numerical dissipation

with a fine grid at this vortex age. Therefore, a simulation with an LES turbulence model in the fine discretized region around the blade tip and 300 inner iterations is investigated. The results of the vortex core radius are shown in Fig. 4.13. The prediction of the radius at $\Psi_V = 5.3^\circ$ is compared to the previous URANS solutions clearly improved. Even for the vortex core at $\Psi_V = 15.3^\circ$, there is no diffusion visible, leading to a slight underprediction compared to the experimental data.

4.7 Azimuthal analysis of the vortex core

The radial cuts through the vortex core are used to identify the shape of the vortex core by analyzing every cut on its own.

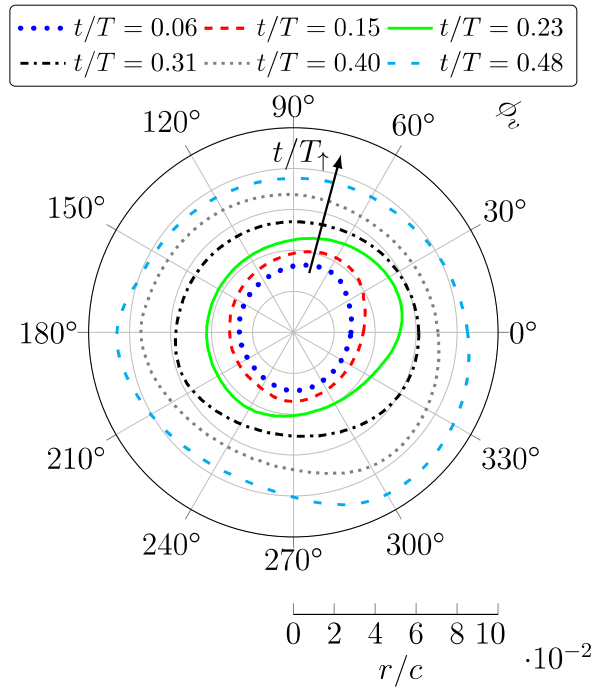


Figure 4.14: Vortex core shape of CFD simulation for several time instants during upstroke at $\Psi_V = 2.6^\circ$.

Figure 4.14 shows the shape of the vortex core obtained with 90 cuts through the vortex core center. The radius is detected at the maximum of the swirl velocity in the respective cut. Ramasamy et al. [78] stated that approximately 60 cuts are suitable to receive a valid result of the shape. Several shapes at constant wake age but at different time steps in the period are shown. It is clearly visible that during the upstroke motion, the vortex-core size increases. Due to the increasing angle of incidence, there is more lift generated, and therefore, a higher pressure difference at the blade tip occurs. The shape of the vortex at $t/T = 0.23$ is not elliptical anymore, as a bulge at

$\phi_v = 30^\circ$ is formed. With increasing time, this bulge is not always as clearly visible. At $\phi_v \approx 135^\circ$ the peak swirl-velocities cover a wider range ($0.4 < v_\phi/U_{\text{tip}} < 0.7$). From this, it can be concluded that both the radius and the maximum swirl velocity increase with increasing angle of incidence.

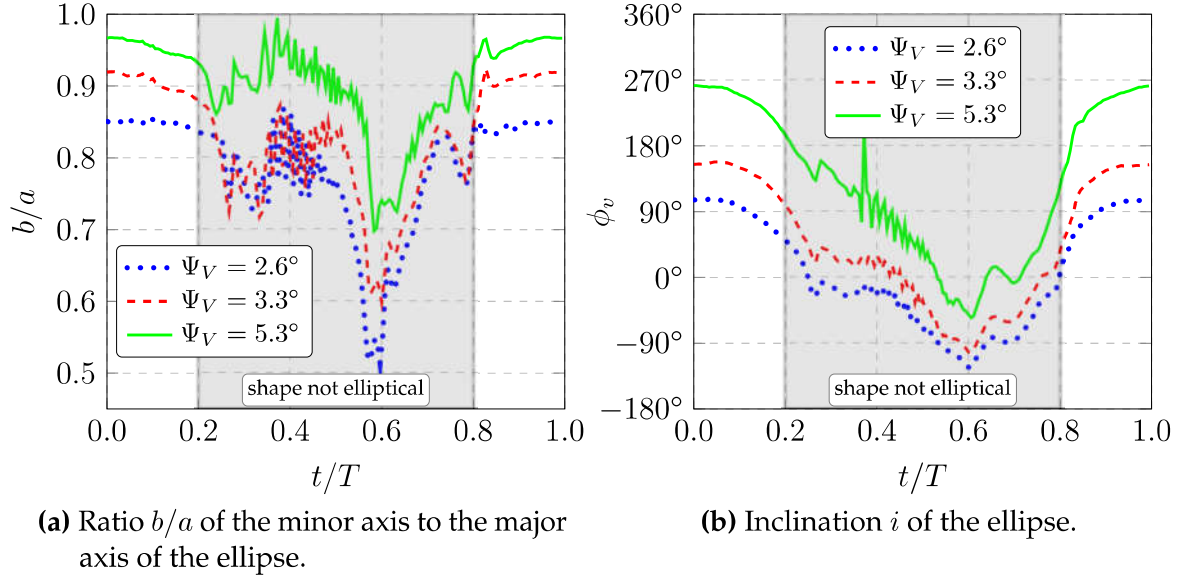


Figure 4.15: Parameters of the ellipse fitted to the vortex core of CFD simulation.

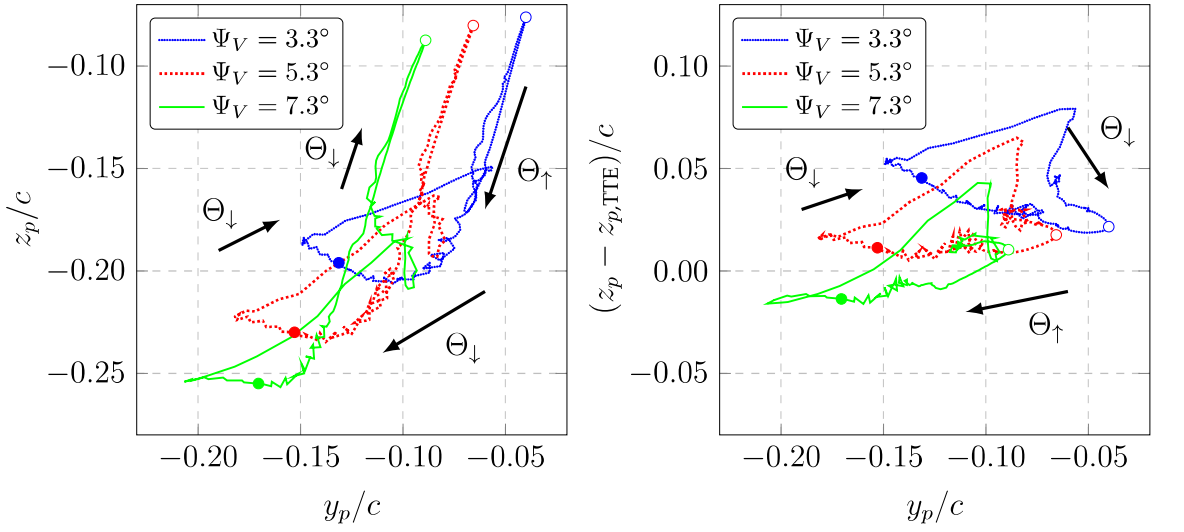
Figure 4.15 shows the parameters b/a and ϕ_v of the ellipse, which has been fitted to the shape of the vortex core. Two parameters define the shape of an ellipse in a two-dimensional plane. The two axes are divided into the major axis a and the minor axis b . Figure 4.15(a) shows the ratio b/a of the two axes over the reduced time for three different wake ages. The smaller the ratio, the more elliptical is the vortex core. At a vortex age of $\Psi_V = 5.3^\circ$, the shape is at the instants of time with low angles of incidence $t/T < 0.2$ and $t/T > 0.8$ nearly a circle with a ratio of $b/a \approx 0.98$. A vortex two degrees younger ($\Psi_V = 3.3^\circ$) shows still an elliptical shape with a ratio of $b/a \approx 0.9$. In all three wake ages, the shape becomes more elliptical with increasing angle of incidence. Values in the middle ($0.2 < t/T < 0.8$) show a high scatter since not all shapes can be fitted with an ellipse. The second parameter is the inclination ϕ_v of the major axis to the y_p -axis, which is shown in Fig. 4.15(b). A value of $\phi_v = 0^\circ$ or $\phi_v = 180^\circ$ means that the ellipse is stretched along the y_p -axis. A positive value stands for an ellipse, which is tilted towards the mathematically positive direction. A fully upright ellipse (along z_p -axis) is denoted by a value of $\phi_v = 90^\circ$ or $\phi_v = -90^\circ$ respectively. Values in the middle ($0.2 < t/T < 0.8$) have to be taken with care since the vortex core shape cannot satisfactorily be fitted to an ellipse anymore. A rotation is already detectable between the three different wake ages. The youngest

vortex at $\Psi_V = 2.6^\circ$ is almost fully upright at the smallest angle of incidence, with an inclination of $\phi_v \approx 90^\circ$. Only $\Delta\Psi_V = 0.7^\circ$ later, the vortex core has turned more than $\Delta\phi_v = 45^\circ$ in counter-clockwise direction and has an inclination of $\phi_v \approx 145^\circ$. Two degrees older, the vortex is again, after turning counter-clockwise, in an almost upright position. In that short distance, the shape of the vortex has therefore rotated half a counter-clockwise rotation, which is in the sense of rotation of the tip vortex. With increasing angle of incidence, the inclination first rises and then drops down doing a clockwise rotation. At the end of the downstroke motion, the vortex does a counter-clockwise rotation.

4.8 Position

Figure 4.16(a) shows the vortex position at different wake ages behind the blade throughout a full cycle. The position is extracted with the methods described in the vortex analysis section on page 39. The position at the lowest angle of incidence is always in the top right corner. At this point, the generated lift is the lowest, leading to the smallest inboard drive. The strong vertical movement is imposed by the prescribed vertical movement of the trailing edge due to the pitching motion. Halfway through the upstroke, the motion starts to get chaotic with a counter-clockwise rotation of the shape setting in. Figure 4.16(b) displays vertical corrected results. The position with respect to the trailing edge exhibits a stronger horizontal than a vertical motion of the vortex core. The highest position $(z_p - z_{p,TTE})/c$ is detected during the downstroke motion. For young vortices up to $\Psi_V = 5.3^\circ$, the vortex always stays above the trailing edge. The timewise motion of the vortex can be drawn by comparing the different graphs yielding a consistent downward and inboard movement. During the upstroke motion, an orbital pattern is revealed in both figures, which occurs at the same time instant when the axial pressure gradient inside the vortex core reaches a maximum, and the vortex breaks down. This leads to an asymmetrical appearance of the vortex. At further increasing angles of incidence, the circle-like vortex core vanishes; the area with the highest negative value of λ_2 is shifted towards one side, and a spiral movement sets in leading to a primary shift inboard superimposed with a rotation of the vortex core itself.

Figure 4.17 shows the tip vortex visualized by the λ_2 criterion for several wake ages and time instants. All plots in a horizontal row are extracted at the same time instant. A value of $t/T = 0$ means that the blade is at its lowest angle of incidence. All plots show situations during the upstroke motion. The upper row shows the earliest



(a) Position of the vortex core with respect to the p-coordinate system (related to the $c/4$ position of the blade).

(b) Position of the vortex core with respect to the blade-tip trailing-edge (TTE).

Figure 4.16: Position of the vortex core of CFD simulation throughout a full cycle, the highest angle of incidence is represented with colored circles, and white filled circles represent the lowest angle of incidence respectively.

situation. Each following row shows the situation $\Delta t/T = 2/360 \approx 5.5 \cdot 10^{-3}$ later, which implies the movement of the blade in that time frame to be exactly $\Delta\Psi = 2^\circ$. Every row shows furthermore three different planes that correspond to an increasing wake age in steps of $\Delta\Psi_V = 2^\circ$. Every plot in one vertical column is extracted at the same wake age. This leads to the ability to follow slices of the vortex in time. The vortex in the upper left plot is $\Delta t/T = 2/360$ later, exactly $\Delta\Psi_V = 2^\circ$ older and, therefore, depicted in the picture diagonal southeast. The black arrows show the evolution of one vortex in time. This applies to all other pictures too. All columns correspond to a plane following the blade under a defined angle. Most data in this study are displayed in this way. In the left column, it can be seen that the area with the highest negative λ_2 value (blue color) is not circularly distributed. This area, which matches the lowest density, has a spin inside the vortex leading to an orbital movement of the vortex core. This is not just a rotation within the period (column-wise perspective) since it is also visible row-wise. A row corresponds to a frozen situation, which is a single solution of the numerical simulation. In the first row, the blue area starts in the upper right area, and $\Delta\Psi_V = 2^\circ$ later, the blue area faces downward. The spin is strongest when following the evolution of a vortex on its fixed geodesic position (indicated by the arrows). The vortices have a spin with offsets dependent on the age, which leads to a timewise spin and a spin along the vortex tube. Gursul et al. [36] describe the vortex breakdown as a dramatic flow disruption accompanied by a spiral winding in an opposite sense of rotation of the vortex.

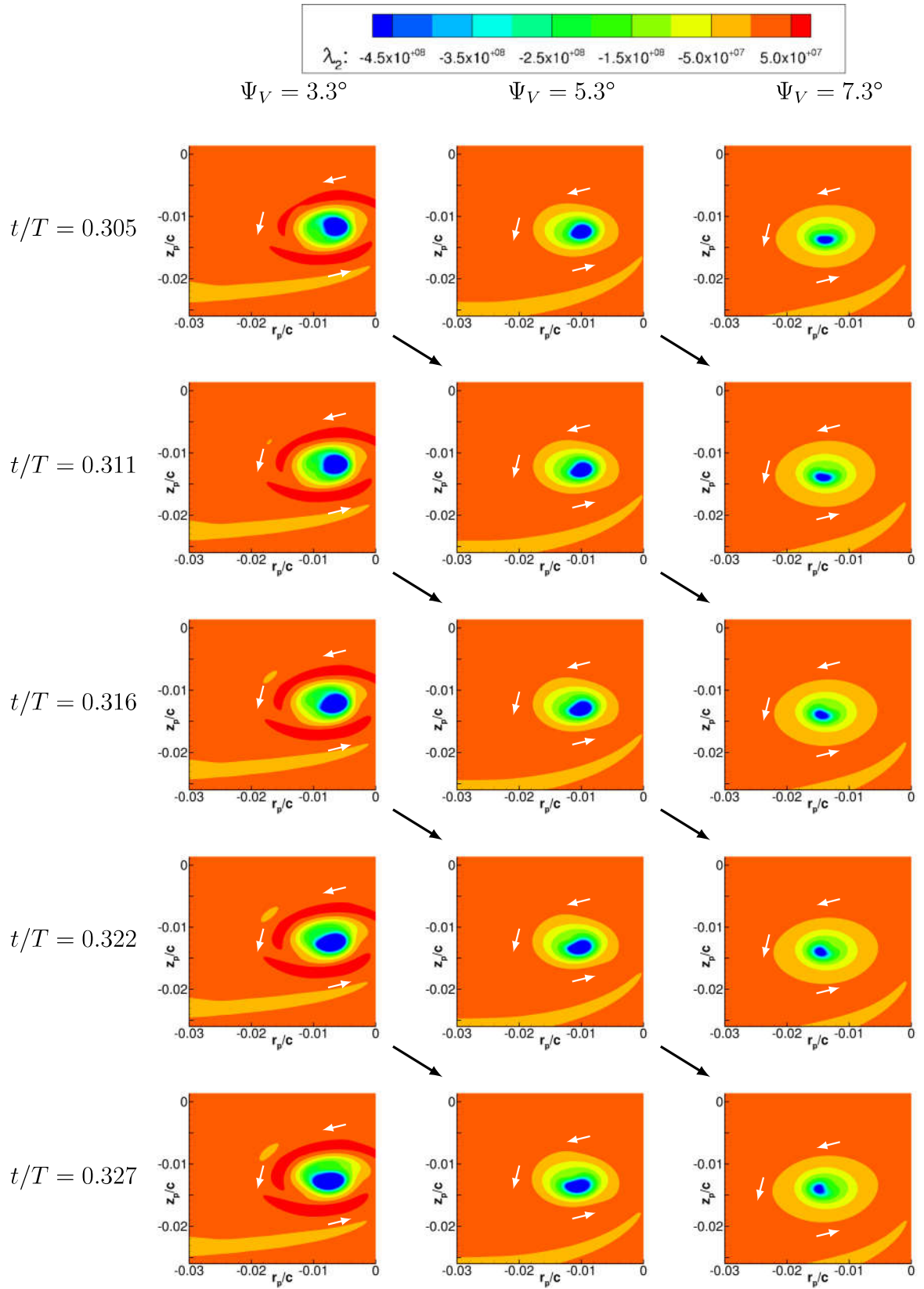


Figure 4.17: Vortex behavior of CFD simulation at different wake ages and time instants during upstroke motion visualized by λ_2 criterion, black arrows show the evolution of one vortex, white unscaled arrows depict the sense of streamlines.

4.9 Pressure inside the vortex core

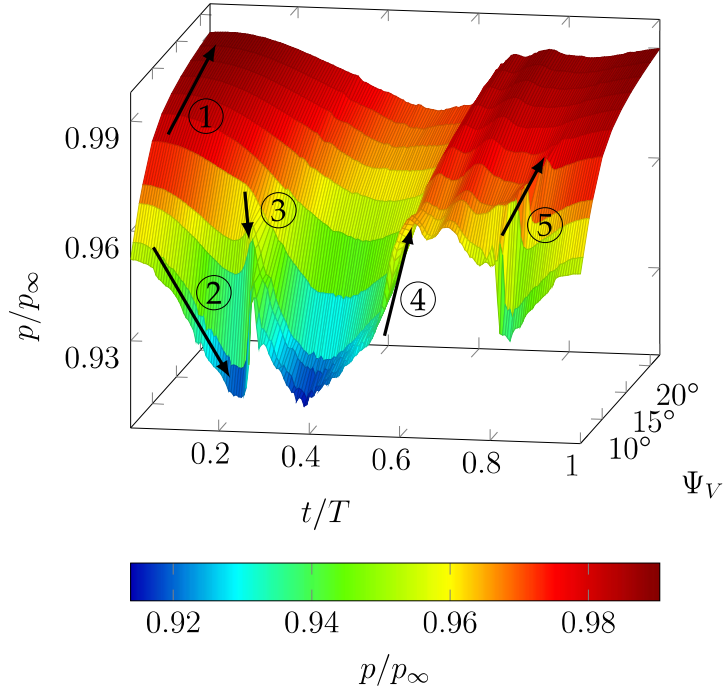


Figure 4.18: Pressure of CFD simulation inside the vortex tube over the period.

All examined vortex cores yield a wake-like appearance that is forced by a positive pressure gradient along the vortex tube. Figure 4.18 shows the pressure along the axis of the vortex for a complete period. The pressure inside a vortex is due to centrifugal forces, lowest on the core axis. The stronger the vortex is, the lower the pressure is. The arrow ① indicates the progress at the lowest angle of incidence pointing towards more advanced wake ages. The pressure increases with increasing vortex age to an asymptotic value, which conforms to the surrounding conditions once the vortex disappears. Due to the pitching motion, a secondary effect is superimposed onto this behavior. During the upstroke motion, the vortex becomes stronger, leading to a timewise decreasing pressure inside the vortex. The arrow ② highlights this effect at a constant young wake age. Both effects work in the same direction; thus, the overall gradient along with the vortex core, which is similar to a total differential, increases. Halfway through the upstroke there is a wave-like appearance of a local pressure maximum visible which moves towards the blade, indicated by the arrow ③. First this hump occurs at $\Psi_V = 3.3^\circ$ and $t/T \approx 0.25$, which is a sign of vortex breakdown, as Visbal [112] states that the pressure gradient, along the vortex axis has a major influence on the initiation of vortex breakdown above a pitching delta wing. Garmann & Visbal [28] observed vortex breakdown with abrupt flow reversal

on revolving wings to be driven by the pressure gradient and not by local Reynolds number. Around $t/T = 0.4$, the pressure reaches its minimum visible in Fig. 4.18. The flow separates at $t/T \approx 0.55$, which corresponds to the arrow ④ in Fig. 4.18, when the pressure at young wake ages rises towards the situation that the pressure is almost constant inside the vortex tube. The arrow ⑤ marks a drop in the pressure, which coincides with the reattachment process. This drop moves downstream like a wave.

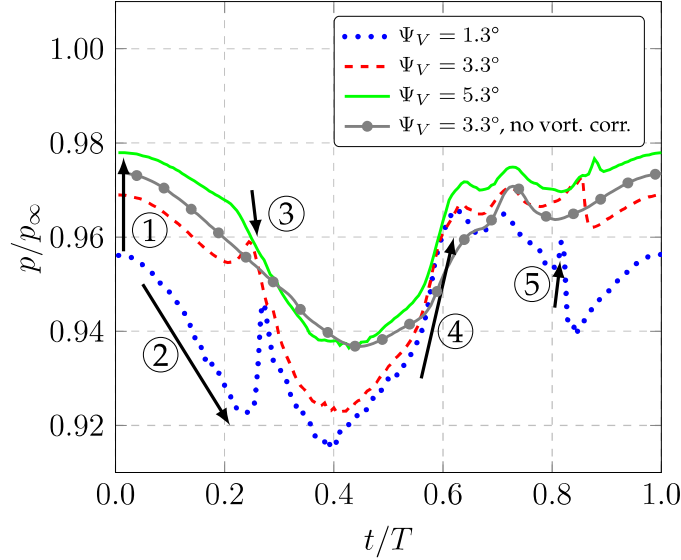


Figure 4.19: Pressure of CFD simulation inside the vortex tube over a complete period at several constant wake ages.

For clarity, three pressure distributions of different wake ages are plotted in Fig. 4.19. They are extracted from the same data, as shown in Fig. 4.18. Additionally, the pressure distribution at $\Psi_V = 3.3^\circ$ of a simulation without vortical correction is shown. The arrows are transferred with the same number. At $t/T \approx 0.2$ there is still a difference between the pressure at $\Psi_V = 3.3^\circ$ and $\Psi_V = 5.3^\circ$. This difference diminishes with increasing time by a reduction in the pressure at $\Psi_V = 5.3^\circ$ and an increase at $\Psi_V = 3.3^\circ$. This timewise maximum moves towards younger wake ages. The pressure at $t/T \approx 0.4$ is almost two percent higher if no vortical correction is implemented.

Figure 4.20 shows the effect of the vortical correction method by additionally showing the axial velocity at the wake age of $\Psi_V = 3.3^\circ$ of a simulation without vortical correction. At $t/T = 0.2$, the absolute value of u_p jumps to values higher than the blade-tip velocity, which coincides with the reduced time when the vortex starts an orbital, rotational, and meandering movement. The vortical correction reduces the viscosity in order to delay the numerical dissipation. The production term is

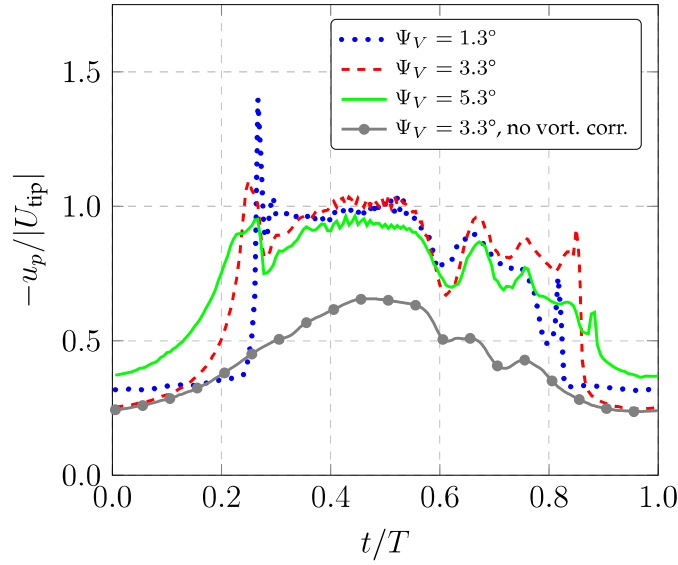


Figure 4.20: Axial velocity of CFD simulation inside the vortex tube over a complete period at several constant wake ages.

varied using the ratio of the strain term to the vorticity term as a sensor [115]. In this study, the ratio is small due to the small free-stream velocity. The increase in the production term of vorticity leads to a decreased turbulent kinetic energy. It is known that without vortical correction, the vortex diffuses too quickly since too much eddy viscosity is produced. The distinct peak at $t/T \approx 0.3$ is not detectable in both the core pressure and axial velocity in the simulations without vortical correction. The axial velocity is smooth and reaches up to 60% of the blade-tip velocity.

4.10 Effect of rotation

Kaufmann et al. [47] showed a comparison between their numerical investigations and experimental data of a pitching rotor blade-tip model. The same airfoil DSA-9A is used along the span with a positive twist towards the blade tip, and the same SPP8 blade-tip shape. The blade-tip model has a chord length of 0.27 m, and the pitching motion leads to dynamic stall on the model. Kaufmann et al. [47] implemented a higher temporal resolution with only half the resolution in the spatial domain. The background grid consisted purely of tetrahedral cells. Since their investigation was without rotation, the effect of rotation on the blade-tip vortex can be analyzed by comparing the results of both investigations. The circulation is normalized using the flow velocity U_{707} at $r/R = \sqrt{2}/2 \approx 0.707$. This point separates the amount of flow on the blade in two equal parts, since the blade experiences in the rotational case a

linearly increasing flow velocity $U_{\text{tip}} \cdot \frac{r}{R}$, see equation (4.2). For the nonrotating case, U_{707} corresponds to U_{tip} .

$$\frac{1}{2} \int_0^R U_{\text{tip}} \cdot \frac{r}{R} dr = \int_{\frac{\sqrt{2}}{2} \cdot R}^R U_{\text{tip}} \cdot \frac{r}{R} dr = \int_0^{\frac{\sqrt{2}}{2} \cdot R} U_{\text{tip}} \cdot \frac{r}{R} dr \quad (4.2)$$

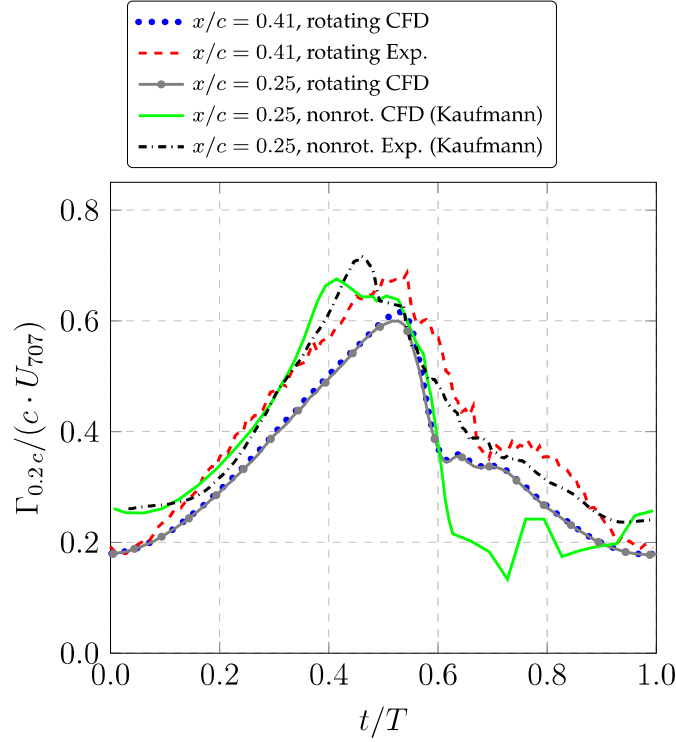


Figure 4.21: Circulation of experiment [15] and CFD simulations, nonrotational data after Kaufmann et al. [47], $\Psi_V = 2.6^\circ (x/c = 0.41)$.

Figure 4.21 shows the circulation in the blade-tip vortex at a constant radial distance of $r_v = 0.2c$ of this study and data taken of Kaufmann et al. [47]. The two experiments were analyzed at different wake ages. Therefore, numerical data of this study is additionally shown at the equivalent wake age ($x/c = 0.25$) of the nonrotating investigation. The wake-age difference is negligible since there is almost no difference between the numerical data. During the upstroke motion ($0 < t/T < 0.5$), the nonrotational results match well. The level of the normalized circulation is in the same order for both cases.

5 Blade-tip vortices of a four-bladed rotor²

In this chapter, a cyclic pitching case (unsteady) and light climb cases (static), as shown in Fig. 5.1, are examined. After introducing the numerical setup, the results of the simulations with five constant pitch angles $\Theta_r = [18^\circ, 21^\circ, 24^\circ, 27^\circ, 30^\circ]$, with a focus on the vortex generation and propagation, are presented. These results are then compared to the corresponding pitching simulation with $\Theta_r = 24^\circ - 6^\circ \cos(2\pi t/T)$. This computed simulation corresponds to a forward flight situation, but without the typical Reynolds number and Mach number variation.

5.1 Numerical setup of the four-bladed rotor

In the following, the numerical grid and setup of the four-bladed rotor are described.

The DLR-TAU code was used for the numerical simulations. This node-based, unstructured finite-volume solver can treat grids with a range of elements, including prisms, pyramids, tetrahedra, and hexahedra. The grid is constructed using CENTAURTM [19] to have rotor blade grids with a prismatic boundary layer region with 30 prisms in the direction normal to the surface. A stretching factor of 1.26 is used, starting with the first cell height of $y^+ \sim \mathcal{O}(1)$. The surface grid is restricted to a maximum of $s/c = 0.02$, reducing to $s/c = 0.004$ at the leading and trailing edges. Outside of the boundary layer region, a tetrahedral grid is implemented up to the far field of the blade grid ($x/c = 1.25$). A refinement of the tetrahedral grid to $s/c = 0.004$ in the blade-tip region captures the blade-tip vortex and correctly propagates it from the surface into the volume grid, as shown in Ref. [32]. Once in the volume flow, a fine tetrahedral grid ($s/c = 0.005$) transports the vortex to the edge of the blade grid.

²Text and illustrations from this chapter appear in:

A. Goerttler, J. N. Braukmann, C. C. Wolf, A. D. Gardner, and M. Raffel, "Blade Tip-Vortices of a Four-Bladed Rotor with Axial Inflow", *VFS 75th Annual Forum*, Philadelphia, Pennsylvania, 13–16 May, 2019, (Ref. [33]).

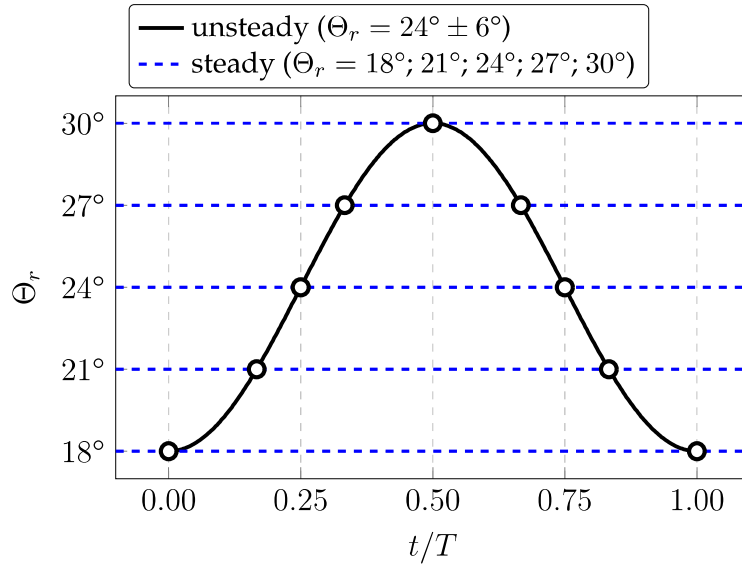


Figure 5.1: Visualization of examined cases.

Each of the four blade grids has 9.5 million points. The blades are moved as rigid bodies with either prescribed static pitch or sinusoidal cyclic pitch, depending on the test case. In this chapter, only the part of the blade with an aerodynamic profile is accounted for. Figure 4.1 on page 48 highlights the root part finishing at $y/R \approx 0.25$, which is not simulated in this chapter.

The four identical blade grids of the four-bladed RTG rotor are embedded in a background grid, which primarily uses tetrahedral cells and has a total size of 48 million points. The background grid has a far-field freestream external boundary implemented as a spherical computational domain with a radius of 900 blade spans. The data exchange between the blade grids and the background grid is carried out using the overset grid (Chimera) method using a three-cell interpolation region, which also transports the second-order flow from the blade grids to the edges of the explicit cut-outs in the background grid. The tetrahedral background grid has edge lengths of $s/c = 0.015$ near the blades, expanding to $s/c = 0.2$ one rotor radius downstream of the rotor. A curved, structured grid is introduced into the background grid following the expected path of the blade-tip vortex; see Fig. 5.2. This grid is a block-structured H-grid, constructed so that the grid axes are normal and tangential to the vortex core trajectory at each point. The grid has a spacing of $s/c = 0.0034$ normal to the vortex core propagation direction near the blade, increasing to $s/c = 0.0091$ at a vortex age of $\Psi_V = 90^\circ$. The grid in the vortex core propagation direction is 6:1 coarser than in the normal direction. The background grid with the explicit cut-out holes is rotated with the blades so that in the frame of the background grid, the blades undergo only a pitching motion.

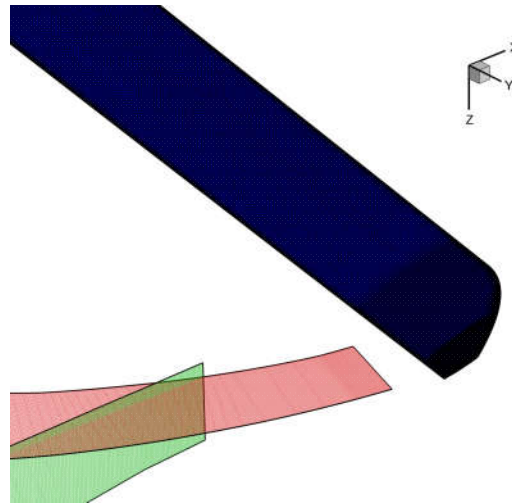


Figure 5.2: Cuts displaying hexahedral cells at $y/R = 0.9$ and $z/c = 0$.

Figure 5.3 gives an overview of the utilized grid. A sphere with a radius of 900 blade spans is used for the far field; see Fig. 5.3(a). The area which is significantly influenced by the rotor is finer discretized, as is depicted in Fig. 5.3(b). The chimera setup is highlighted in Fig. 5.3(c). The blade grid has a cylindrical form that is cut off below the horizontal line. With this approach, some grid cells can be saved, and wakes of the preceding blade have better chances not to interfere with a chimera border again. Figure 5.3(d) shows the same slice in an isometric view.

The computations used 1440 time steps per period, with at least 50 inner iterations per time step, which is sufficient, as shown in Fig. 5.4. All shown static simulations were computed with 60 coarse periods with 36 time steps per period, followed by 2 fine periods. The cyclic simulations were computed with 60 coarse periods, 10 intermediate periods with 360 time steps per period, and 3 fine periods with 100 inner iterations per time step. The periodicity of the final solution was used as the time convergence criterion. The Menter-SST model [65] was utilized to close the URANS equations. In the region of the blade-tip vortex, an LES model [107] is used, whereas, in all other regions, a conventional SST turbulence model is used. If specified, an optional Low-Dissipation Low-Dispersion (LD2) scheme [63] was additionally employed in the LES region. The LES model uses a vorticity-sensitive volume filter to reduce the grey area at the hybrid RANS/LES interface on anisotropic grids by only accounting for the grid spacing in the plane normal to the local vorticity vector. In that plane, the filter reduces to a volume-like formulation. The Smagorinsky sub-grid scale model [96] is used, with a default Smagorinsky coefficient of 0.17. The computations are second-order in space and time; the inviscid fluxes are solved by a central method.

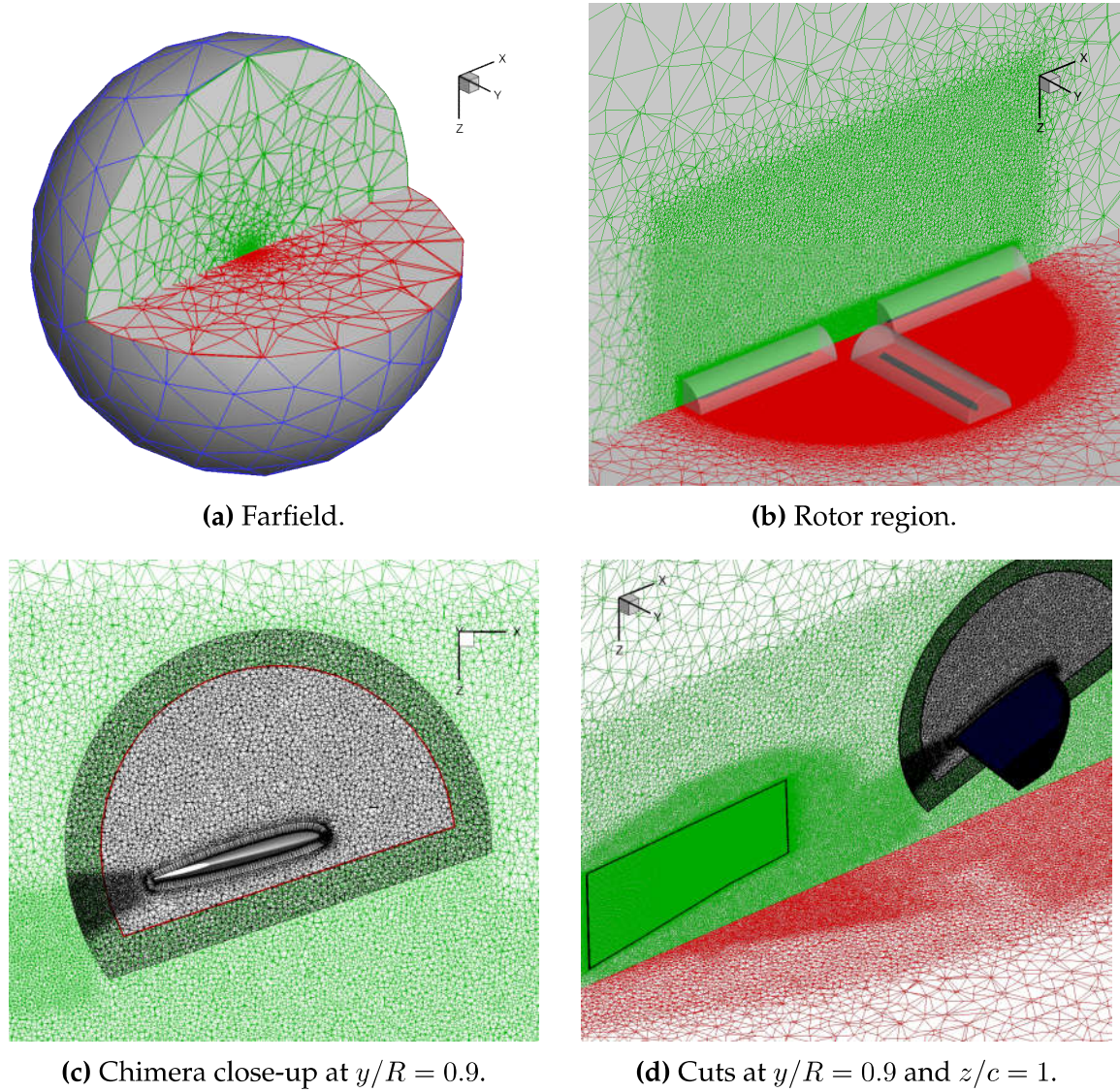


Figure 5.3: Numerical grid of the four-bladed rotor.

Convergence

All simulations were done with a dual-time stepping approach, which uses physical time steps and inner iterations. The blade rotates and changes position from one physical time step to the next time step. However, after the movement of the blade and grid, the flow characteristics are still determined by the old time level. Therefore, several inner iterations are used to compute the instantaneous situation without any movement towards a pseudo-stationary solution.

Table 5.1 shows the density-residual of different cases. The number of steps per period N_Ψ and inner iterations N_{inner} are shown. The residual at the start and end of the inner iterations points out the decrease, which is achieved in one time step. The last column summarizes the difference by displaying the density residual

Table 5.1: Residual values of different cases.

	N_Ψ	N_{inner}	$R_{\rho,\text{start}}$	$R_{\rho,\text{end}}$	Δb
URANS	360	50	$2.8 \cdot 10^{-0}$	$4.5 \cdot 10^{-3}$	2.8
URANS	360	100	$2.8 \cdot 10^{-0}$	$3.5 \cdot 10^{-3}$	2.9
DES	1440	100	$7.0 \cdot 10^{-1}$	$3.5 \cdot 10^{-3}$	2.3
LD2	1440	100	$7.0 \cdot 10^{-1}$	$3.5 \cdot 10^{-3}$	2.3

reduction in orders of magnitude ($\Delta b = \log(R_{\rho,\text{start}}/R_{\rho,\text{end}})$). The finer discretized cases reach a lower residuum after all their inner iterations but have a lower reduction since their start is already on a lower value. Chaderjian & Buning [21] considered a density residual reduction by $\Delta b = 2.2$ as time converged. The above results therefore strongly suggest being time-converged.

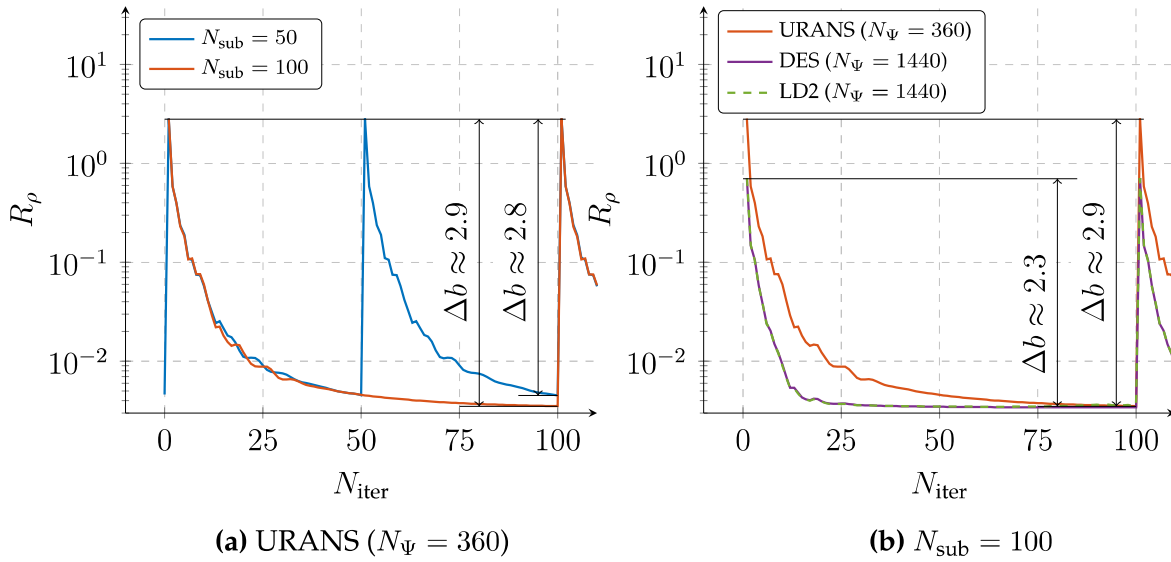
**Figure 5.4:** Density residual of different parameter settings.

Figure 5.4(a) shows the influence of the number of inner iterations for two URANS solutions (first and second row in Tab. 5.1). If 100 inner iterations are used, a density residual reduction of 2.9 orders of magnitude is reached, which slightly exceeds the reduction of 2.8 orders of magnitude when 50 inner iterations are used. Both settings are sufficient time converged. On the other hand, Fig. 5.4(b) shows a variation of the number of physical time steps (second, third, and fourth row in Tab. 5.1). $N_\Psi = 360$ time steps lead to a slightly higher reduction of 2.9 orders of magnitude since the density residual at the start of each time step is higher. A higher number of time steps, $N_\Psi = 1440$, results in a reduction of 2.3 orders of magnitude. The use of DES or LD2 with this finer temporal discretization does not change the time convergence. This study concludes that a sufficiently time converged solution is reached after approximately 30 inner iterations.

5.2 Thrust polar of static cases

Figure 5.5 shows that the thrust of the rotor is underpredicted. Additionally, it shows that the static stall angle of the rotor in the experiments is $\Theta_r = 29^\circ$, such that the computation at $\Theta_r = 30^\circ$ can be expected to show stalled flow.

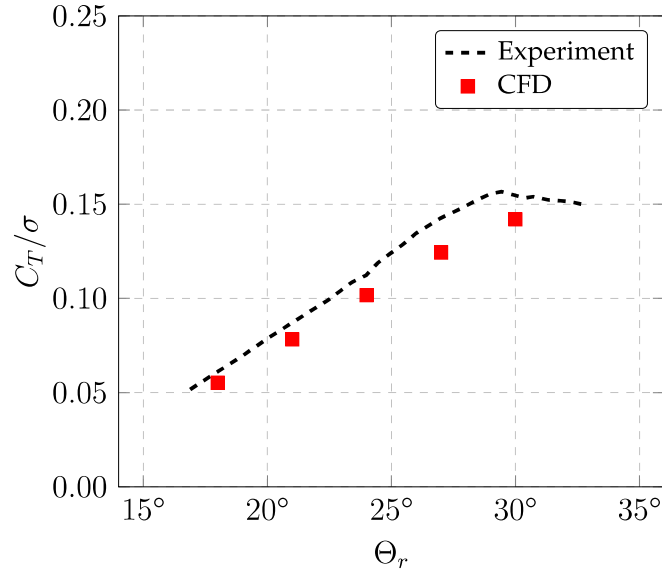


Figure 5.5: Thrust coefficient of experiment and CFD simulations.

The experiments were carried out with a constant velocity in the wind tunnel. The measured results were then used for the constant far field boundary condition in the numerical simulation. This assumption results in slightly different flow fields, as depicted in Fig. 5.6. Here, the downwash velocity w is plotted against the radial position. There is no difference in the inflow (here $1R$ above) if the experimental settings are varied. Both the static ($\Theta_r = 20^\circ$) and the unsteady ($\Theta_r = 20^\circ \pm 6^\circ$) experimental settings experience an incoming flow just below 4 m/s. Therefore, it is feasible to compare the experiment with the numerical data at slightly different incidence angles ($\Theta_r = 18^\circ$ and $\Theta_r = 21^\circ$). In the plane, one rotor radius above the rotor, the incoming flow in the numerical simulations is around 5 m/s. The dashed lines depict the downwash velocity one rotor plane below, showing an agreement along with their steep decrease in the outer quarter of the blade. At around $r/R \approx 1$, the velocities below the rotor approach the velocities above the rotor, which are approximately constant along the full stretch of the rotor. Further outboard, the velocity is lower due to the stream tube of the helicopter rotor. Therefore, the assumption of taking the wind tunnel velocity as far field boundary condition requires a trim according to the thrust level.

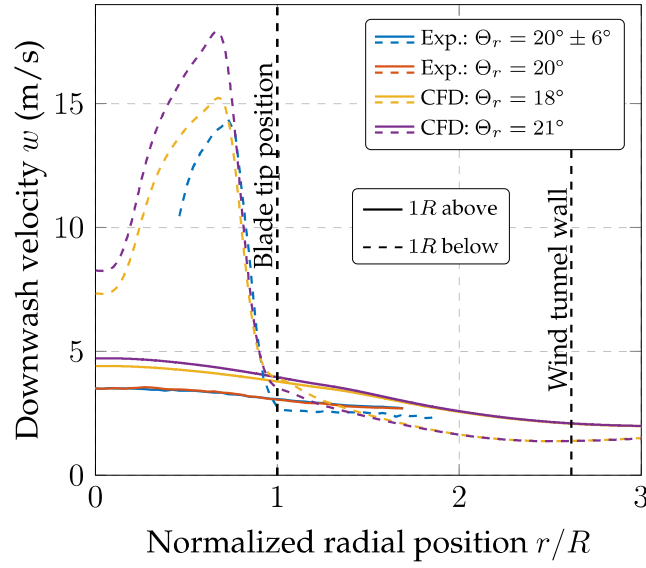


Figure 5.6: Phase-averaged downwash velocity against the radial position in two planes close to the rotor (— = $1R$ above; --- = $1R$ below).

Figure 5.7 displays the λ_2 isosurface of five different light climb (hover with axial inflow) simulations with different collective pitch angles. The creation process of the vortex starts at the leading edge of the tip, forming a slender vortex. The blade-tip vortex grows with an increasing angle of incidence, staying slender except at the highest angle ($\Theta_r = 30^\circ$), which shows a radically expanded vortex covering $\Delta r/R \approx 5\%$. This result has been shown to be associated with separated flow, see Ref. [47], which is in agreement with the expectation from the thrust polar.

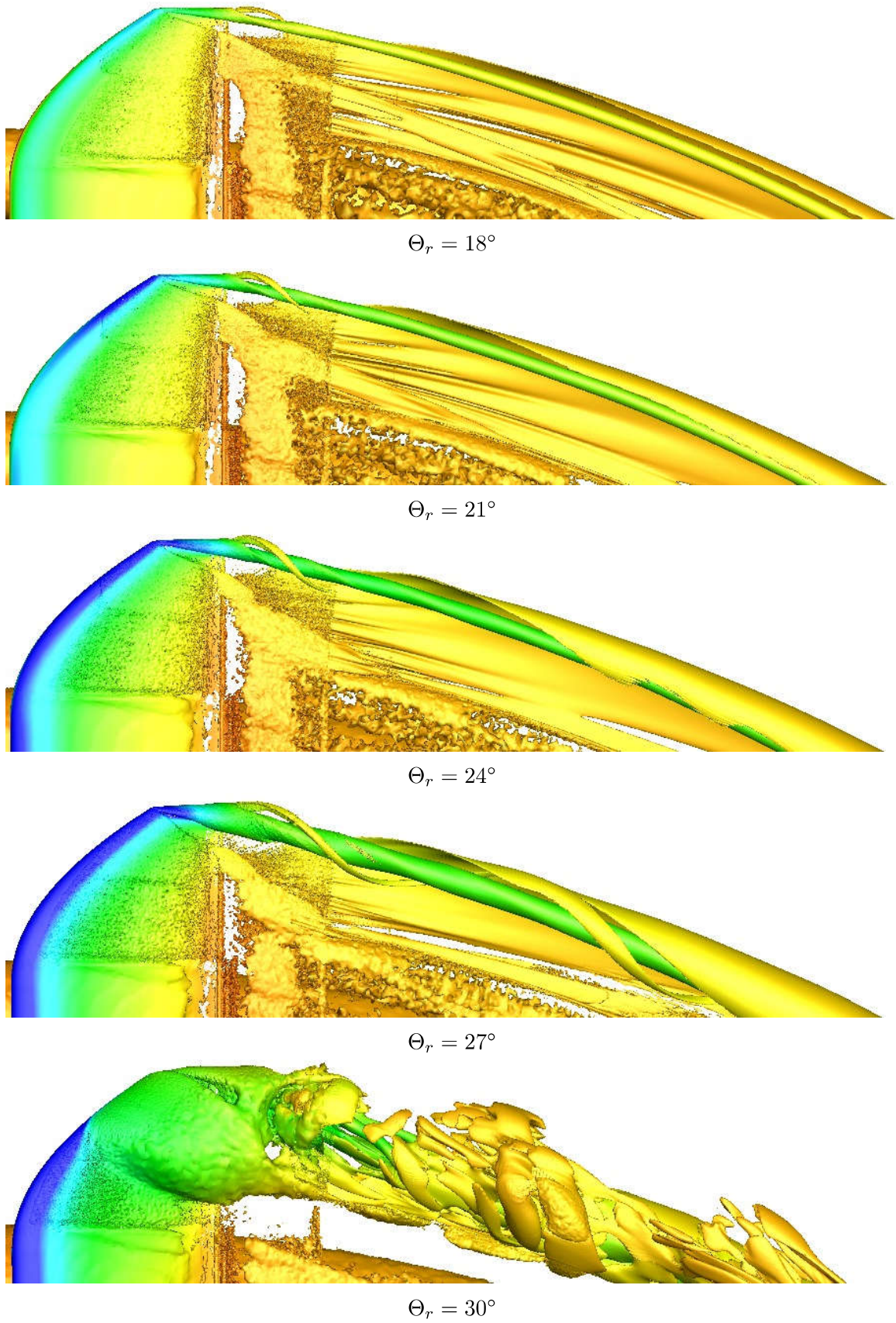


Figure 5.7: Close up view on the blade-tip vortex for five different static cases.

5.3 Effect of DES compared to URANS

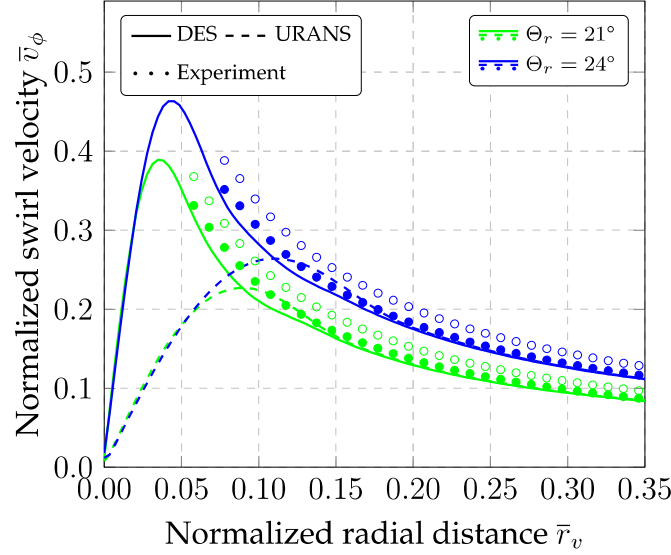


Figure 5.8: Normalized swirl velocity of blade-tip vortex over radial distance for different constant pitch angles at $\Psi_V = 15^\circ$ (— = DES; --- = URANS; $\circ\circ\circ$ = Exp.; $\bullet\bullet\bullet$ = corr. Exp.).

Quantitative results of the tip vortex at a young wake age of $\Psi = 15^\circ$ are shown in Fig. 5.8 for collective pitch angles of $\Theta_r = 21^\circ$ and $\Theta_r = 24^\circ$. The radial distributions of the swirl velocity clearly exhibit the effect of the zonal LES approach, which is shown as solid lines (—). The plain URANS approach, shown as dashed lines (---), exhibits a much smaller peak swirl-velocity appearing at a larger core radius r_c , giving the vortex a smeared-out appearance. This weakening of the vortices is due to the numerical dissipation. This effect increases with wake age, as also seen by other authors [68]. The validity of the DES approach is underlined by the experimental results in Fig. 5.8. The unfilled circles ($\circ\circ\circ$) correspond to the measured values at the same pitch angle Θ_r , yielding slightly larger swirl-velocity levels due to the higher experimental thrust coefficient, as displayed in Fig. 5.5. Multiplying the experimental distributions with a scalar factor derived from the ratio of the corresponding thrust levels yields the distributions marked by filled circles ($\bullet\bullet\bullet$), which are in good agreement with the DES results. It is noted that the experimental results do not cover data close to the vortex center ($\bar{r}_v \rightarrow 0$). This is due to voids in the PIV tracer particle distributions resulting from strong centrifugal forces, which yields unreliable or erroneous data; see Refs. [14, 117]. The voids were mapped in the PIV raw images, and the current results only show valid data outside of the voids.

Figure 5.9 shows the normalized swirl velocity at two wake ages for different

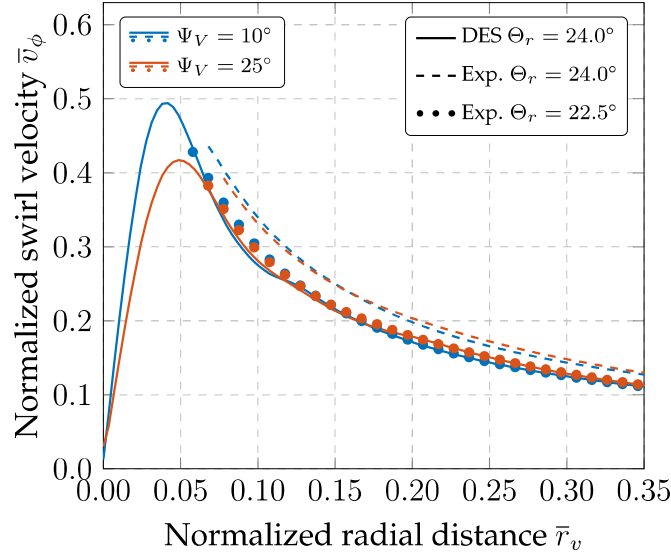


Figure 5.9: Normalized swirl velocity of blade-tip vortex over radial distance with different settings (— = DES; - - - = Exp.; ●●● = trimmed Exp.).

settings. Experimental and numerical data with the same constant angle of incidence (solid and dashed line, respectively) predict different swirl-velocity distributions due to the varying thrust produced; see Fig. 5.5. The filled circles present the swirl-velocity distribution of an experimental run with a reduced angle of incidence ($\Theta_r = 22.5^\circ$). This trimmed case ($F_z = 213$ N) matches the thrust of the numerical simulations ($F_z = 215$ N) with $\Theta_r = 24^\circ$ by less than 1% error. The distributions at both presented wake ages show a strong agreement. The same thrust levels result in the same swirl-velocity distribution. This observation justifies the correction by the scalar factor derived from the thrust levels ratio.

Figure 5.10 summarizes the numerical vortex structures for different collective pitch angles between $\Theta_r = 18^\circ$ and $\Theta_r = 30^\circ$. As in Fig. 5.8, the lesser concentration of the vortex core region of the URANS simulations is visible. Nevertheless, both URANS and DES agree on an identical or at least very similar swirl velocity towards larger radial distances, which is due to the prescribed thrust level and, therefore, the prescribed vortex circulation. The vortex strength (peak swirl strength) and core radius increase with collective pitch angle Θ_r , as could be seen in Fig. 5.7. The result at $\Theta_r = 30^\circ$ is qualitatively different due to flow separation at this collective pitch angle.

Figure 5.11 shows the swirl-velocity profiles normalized to their values at the vortex core. The lines show self-similar behavior. Vatisstas et al. [111] extended the vortex model due to turbulent effects by introducing a new parameter β . Table 5.2 shows the fitting factor β for a constraint peak value and different weighting parameters.

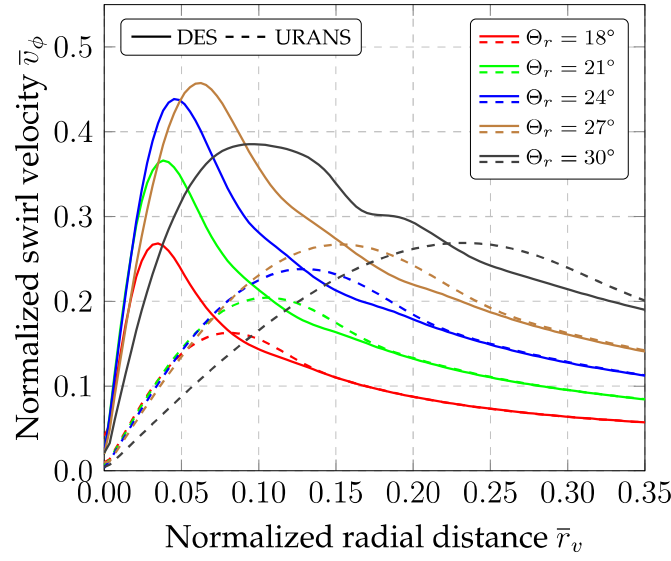


Figure 5.10: Normalized swirl velocity of blade-tip vortex over radial distance for different constant pitch angles at $\Psi_V = 20^\circ$ (— = DES; --- = URANS).

Table 5.2: Fitting factor β for static cases with different weighting parameters.

Θ_r ($^\circ$)	$\beta(w = 0)$	$\beta(w = r/R)$	$\beta(w = (r/R)^2)$
18	1.265	1.284	1.290
21	1.281	1.290	1.291
24	1.255	1.266	1.266
27	1.161	1.182	1.188
30	1.344	1.313	1.300

These options differ in how much they favor the outer part since the numerical errors are smaller there than in the inner part close to the radius. The β values depend on the case and weighting option, but they are all situated between $\beta = 1.2$ and $\beta = 1.3$. The colored lines in Fig. 5.11 back up the mentioned values. According to Ramasamy & Leishman [81], this corresponds to a vortex Reynolds-number of $\text{Re}_v = 3.5 \cdot 10^4$.

The circulation of the blade-tip vortex can be estimated by the path integral of the velocity at a given radius, which is $\Gamma = 2\pi r \bar{v}_\phi$ for a circular vortex. Figure 5.12 shows the circulation of the blade-tip vortex over the radial coordinate. The circulation approaches a saturated value after a first quick rise in the vicinity of the vortex core, and the URANS circulation is equal to the DES circulation for $r_v/c > 0.4$. For the sake of comparability with PIV experiments the single value at $r_v/c = 0.5$ is taken as the circulation of the blade-tip vortex.

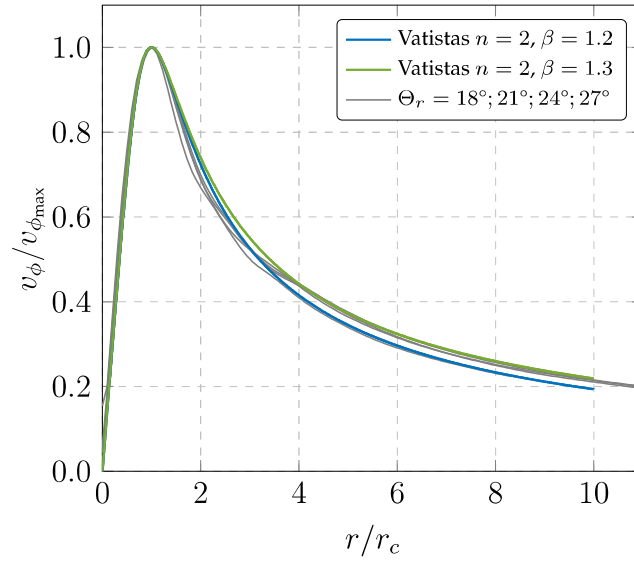


Figure 5.11: Normalized swirl velocity of the blade-tip vortex over radial distance for five different constant pitch angles at $\Psi_V = 20^\circ$ and two fits after Vatistas et al. [111].

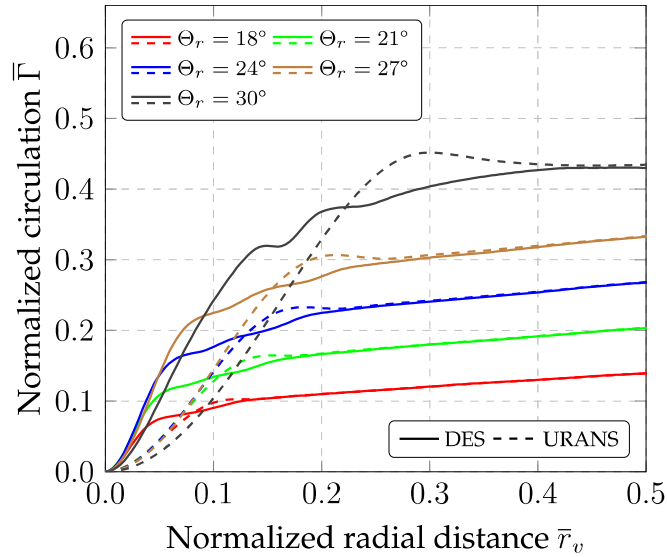


Figure 5.12: Normalized circulation of blade-tip vortex over radial distance for different constant pitch angles at $\Psi_V = 20^\circ$ (— = DES; --- = URANS).

The change of the vortex core radius with increasing wake age is plotted in Fig. 5.13. Again, the dashed curves show the significant numerical dissipation of the plain URANS approach, leading to a rapid expansion of the core size and a rapid linear increase in the core size after $\Psi_V = 45^\circ$. The trend of the DES approach is a slow linear increase in core size with vortex age. The plot starts at the end of the URANS region in the DES computation, needed to ensure sufficient wall distance for the correct operation of the Smagorinsky sub-grid scale model. The grid in the URANS region is constructed with very fine tetrahedral cells to keep the dissipation to a minimum.

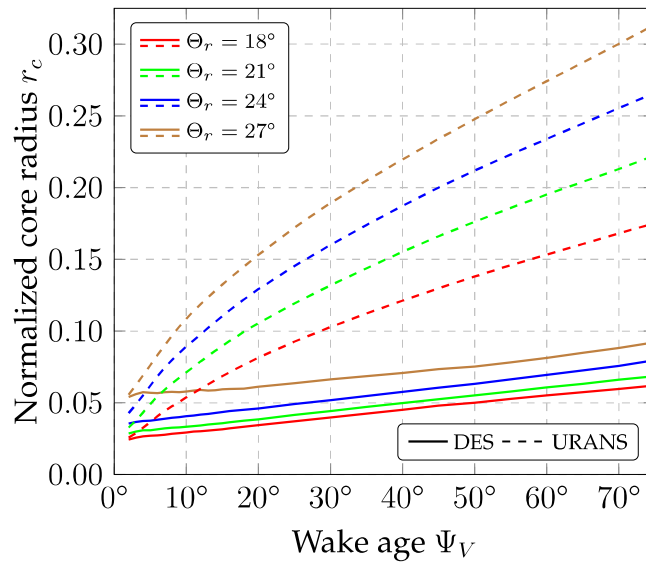


Figure 5.13: Normalized radius of blade-tip vortex for different constant pitch angles over the wake age (— = DES; --- = URANS).

5.4 Vortex generation

Figure 5.14 shows the circulation distribution on the blade, from a path integration of the surface pressure at each radial station, using the Kutta-Joukowski theorem. The circulation increases towards the tip since the increase in velocity is not fully offset by the negative linear twist, reaching a maximum around $r/R \approx 0.9$. At both the inner and outer end, the lift and circulation are zero. All cases except for the highest angle of incidence $\Theta_r = 30^\circ$ have a distinct spike close to the tip, caused by the reattachment line of the blade-tip vortex. The distinctive peak is further inboard for $\Theta_r = 30^\circ$ case, as the separation/vortex region expands to cover nearly the entire blade tip, as also seen in Fig. 5.7(e).

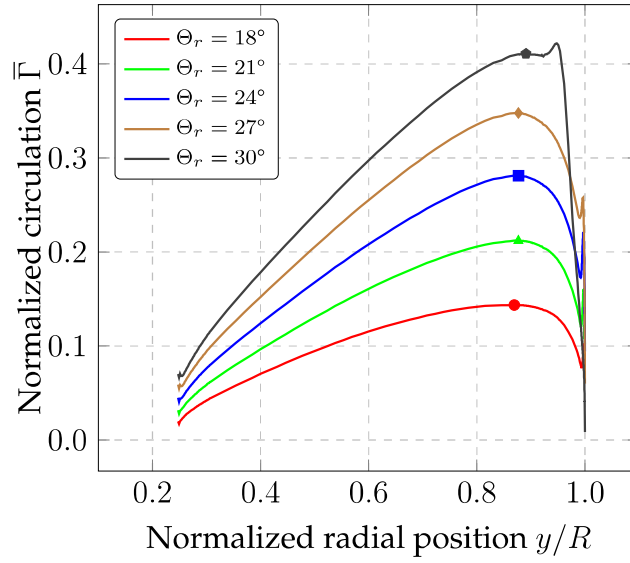


Figure 5.14: Radial circulation distribution on the blade for different constant pitch angles.

In Fig. 5.14, the maximum circulation is marked with a symbol. The roll-up process of a blade-tip vortex depends on the sign of the gradient of the circulation, with a positive gradient inboard of the maximum and a negative gradient outboard of the maximum circulation. All the circulation outboard of the maximum feeds the blade-tip vortex, due to the negative gradient, with the remaining circulation feeding the root vortex. This analysis allows for a comparison of the blade circulation outboard of this maximum and the circulation $\Gamma_{0.5c}$ of the blade-tip vortex at $r_v/c = 0.5$. The ratio of both is shown in Fig. 5.15, showing that about 95% of the blade circulation can be identified as present in the tip vortex. The analysis of the blade circulation allows for differentiation between the near field and far field of a vortex, where 100% of the blade circulation is present in the “vortex”. Almost, the complete blade circulation is found within $r_v/c = 0.5$. Thus, this area is the near field of the vortex and useful for determining the total circulation.

Figure 5.16 shows a comparison of numerical and corrected experimental blade-tip vortex circulations over the radial coordinate. The trend in the CFD data inboard of $r_v/c = 0.5$ shows a linear increase up to $r_v/c \approx 1.2$. Beyond this distance, there is a rapid increase which is not related to the tip vortex, but to an artifact of the circulation computation stretching to the shear flow between the rotor wake and the external flow. Figure 5.16 also shows a comparison of corrected experimental and numerical normalized swirl velocity, revealing a good agreement between both results.

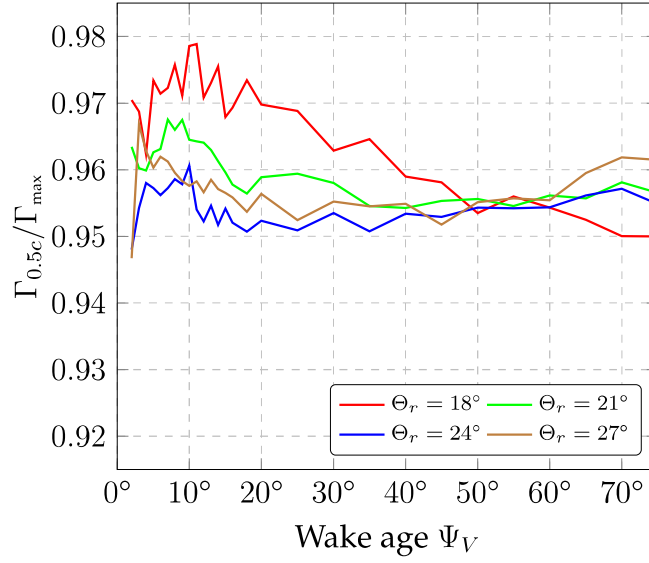


Figure 5.15: Ratio of tip vortex circulation $\Gamma_{0.5c}$ and maximum circulation on the blade Γ_{\max} for different constant pitch angles over the wake age.

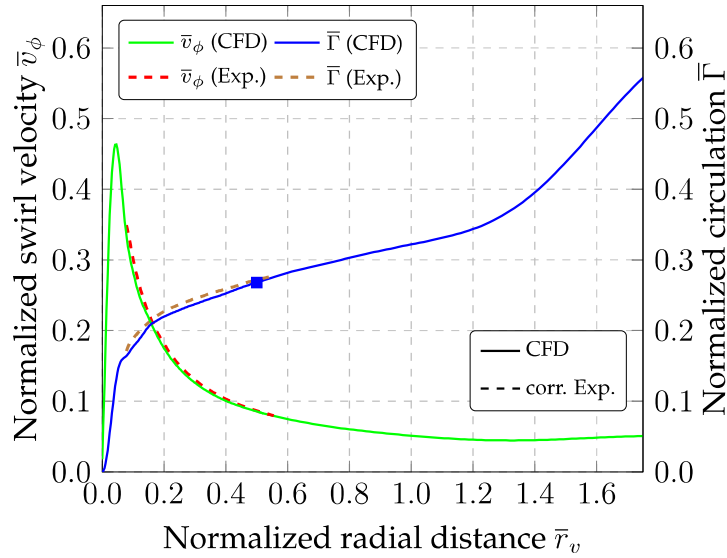


Figure 5.16: Normalized swirl velocity and normalized circulation of blade-tip vortex over radial distance ($\Theta_r = 24^\circ$, $\Psi_V = 15^\circ$).

5.5 Vortex propagation

As indicated in Fig. 3.11, the vortex can be fitted as an ellipse with major and minor axes a and b . After being generated on the blade, the vortex is quite elliptical, as seen in Fig. 5.17, and becomes rounder with time. In the case with the lowest angle of incidence (—), the rounding of the ellipse progresses most quickly, reaching a ratio of $b/a = 0.98$ before $\Psi_V = 10^\circ$, which is 1.5 chord lengths behind the rotor blade, consistent with Refs. [12, 22, 25]. Interestingly, there is a pulsation noticeable in the case with $\Theta_r = 24^\circ$ and $\Theta_r = 27^\circ$, repeating every $\Delta\Psi_V = 4^\circ$ and 5° , which is of the same order as the solid-body rotation speed. Since the radius is fairly constant in this area and a pure rotation results in a constant ratio, the change of the ratio b/a occurs due to an overlaying secondary motion. A complete revolution of the shape is reached after two pulses, as b/a is symmetric after half a revolution. For $\Theta_r = 30^\circ$, the vortex shape is more complex and does not lend itself to an elliptical vortex fit.

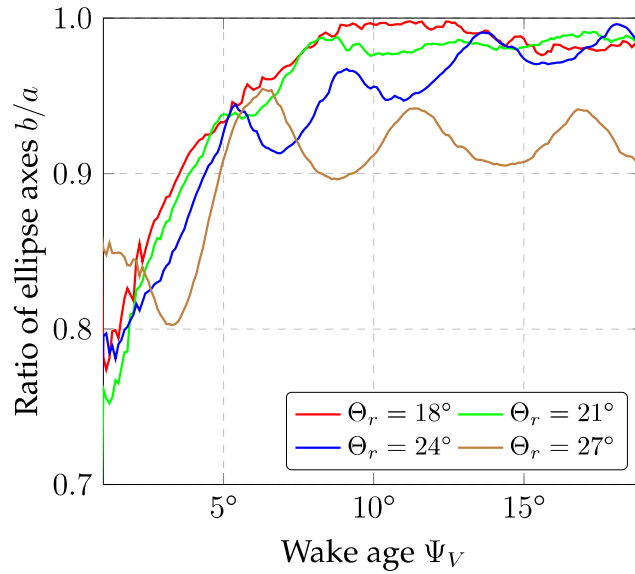


Figure 5.17: Ratio of the axes of the ellipse of the vortex core for different angles of incidence.

Figure 5.18 gives insight into the rotation of the vortex core by displaying the position angle ϕ_v of the fitted ellipse. An increase in ϕ_v implies a counter-clockwise rotation, which is the characteristic rotational direction of the vortex core. With increasing wake, the vortex-core shape approaches a circle, and the angle detection is terminated when an angle can no longer be calculated. Linear fits result in slopes $\delta\phi_v/\delta\Psi_V$, indicating a frequency of the rotation $f \approx 944$ Hz, which is 40 times higher than the rotational frequency of the rotor. The rotational frequency of the vortex core

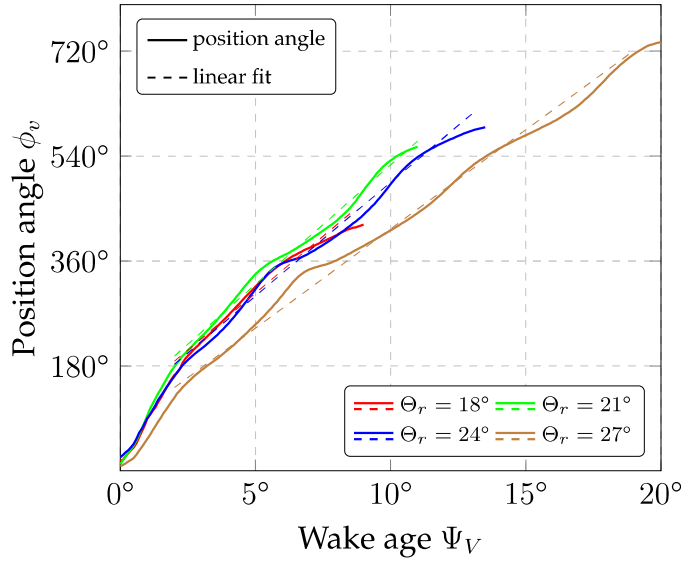


Figure 5.18: Position angle of ellipse.

can be computed from the swirl velocity and core radius and is of the same order as the ellipse rotation. This core rotation frequency, often represented as a solid-body rotation, is on the order of 1500 Hz - 2000 Hz, roughly double the rotation frequency computed from following the elliptical shape of the vortex.

5.6 Vortex-core position

Both following plots separately show the vertical and horizontal displacement over the wake age for different angles of incidence. The vertical vortex-core position is displayed in Fig. 5.19(a), showing that higher collective angles lead to higher lift and faster downward convection of the vortex. Interestingly, the unsteady pitching case for $\Theta_r = 24^\circ - 6^\circ \cos(2\pi t/T)$ is shown to cover the range indicated by the cases with collective pitch only, filling out the region under $\Theta_r = 30^\circ$, since for the dynamic pitching, no stall is seen at this maximum angle of attack. For the pitching rotor, the thrust coefficient is roughly the same as that for $\Theta_r = 24^\circ$, so it can be seen that the vertical position of the blade-tip vortex is a function of the instantaneous blade lift, rather than the rotor thrust. The z -position of the blade-tip vortex for $\Theta_r = 21^\circ$ is one chord length ($\Delta z_p/c \approx 1$) below the rotor disc at $\Psi_V = 80^\circ$. The vertical vortex propagation rate was between three to five chord lengths per revolution.

The opposite is seen for the horizontal blade-tip vortex position, as seen in Fig. 5.19(b). In the cases without a cyclic pitch, the vortex moves more strongly towards the blade root with increasing thrust, corresponding to the stronger contraction of the stream-tube of the rotor wake required by conservation of mass. The

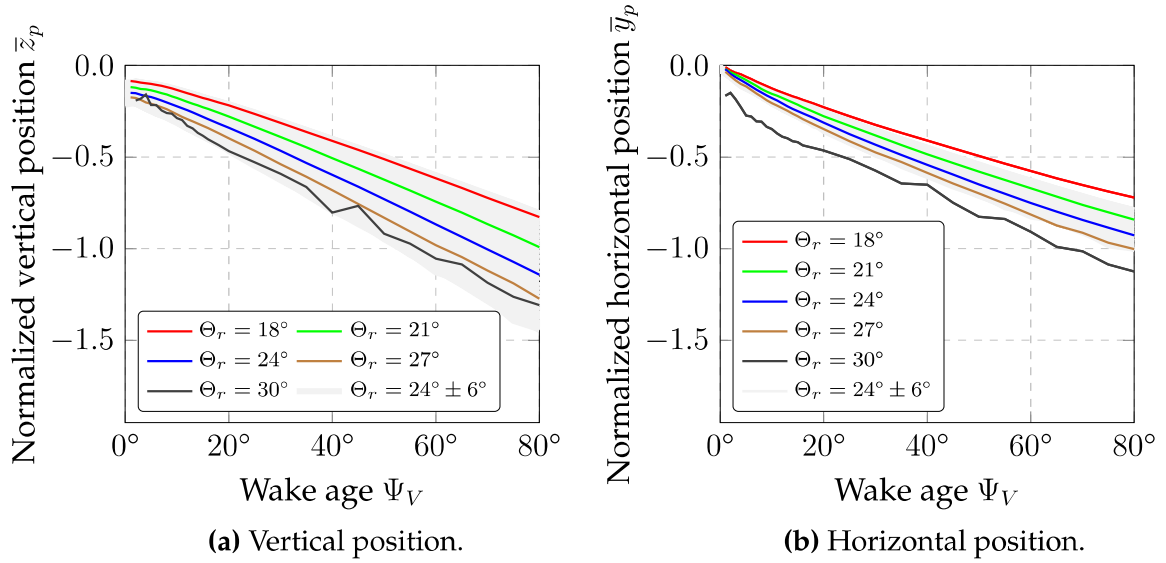


Figure 5.19: Vertical and horizontal position of the blade-tip vortex for different angles of incidence over the wake age (Static and unsteady cases).

blade-tip vortex is at $\Delta y_p/c \approx 0.8$ inboard for $\Theta_r = 21^\circ$ and $\Psi_V = 80^\circ$, and in the first quadrant, the inboard horizontal propagation rates were between two and four chord lengths per revolution. In contrast, the stream tube contraction in the case with cyclic pitch is, on average, the same as for $\Theta_r = 24^\circ$, and clearly, the changes in local thrust do not affect the contraction as much as for constant pitch. The location of the vortices in the dynamic pitching case, thus, occupies a smaller band around $\Theta_r = 24^\circ$.

5.7 Unsteady vortex

The dynamically pitching rotor produces flow, which is qualitatively similar to that seen during the test cases with a constant pitch. Figure 5.20 shows the λ_2 isosurfaces of the flow around the blade tip, analogous to the static results shown in Fig. 5.7. The sole exception to the qualitative similarity is that while there is separated flow on the blade tip for static $\Theta_r = 30^\circ$, the flow remains fully attached for the dynamically pitching case. The dynamic distribution of bound circulation on the blade is shown in Fig. 5.21, including the line of maximum circulation, the circulation outboard of which contributes to the strength of the blade-tip vortex.

Figure 5.22 shows the static vertical position of the blade-tip vortex and the vertical positions of their corresponding counterparts during the unsteady motion. Here the unsteady lines are not connected with the isochronic approach (green line in Fig. 3.9) but with their geodesic position (red line in Fig. 3.9). This means that the vortex position is followed in time after it is produced by the blade tip and convects away. By

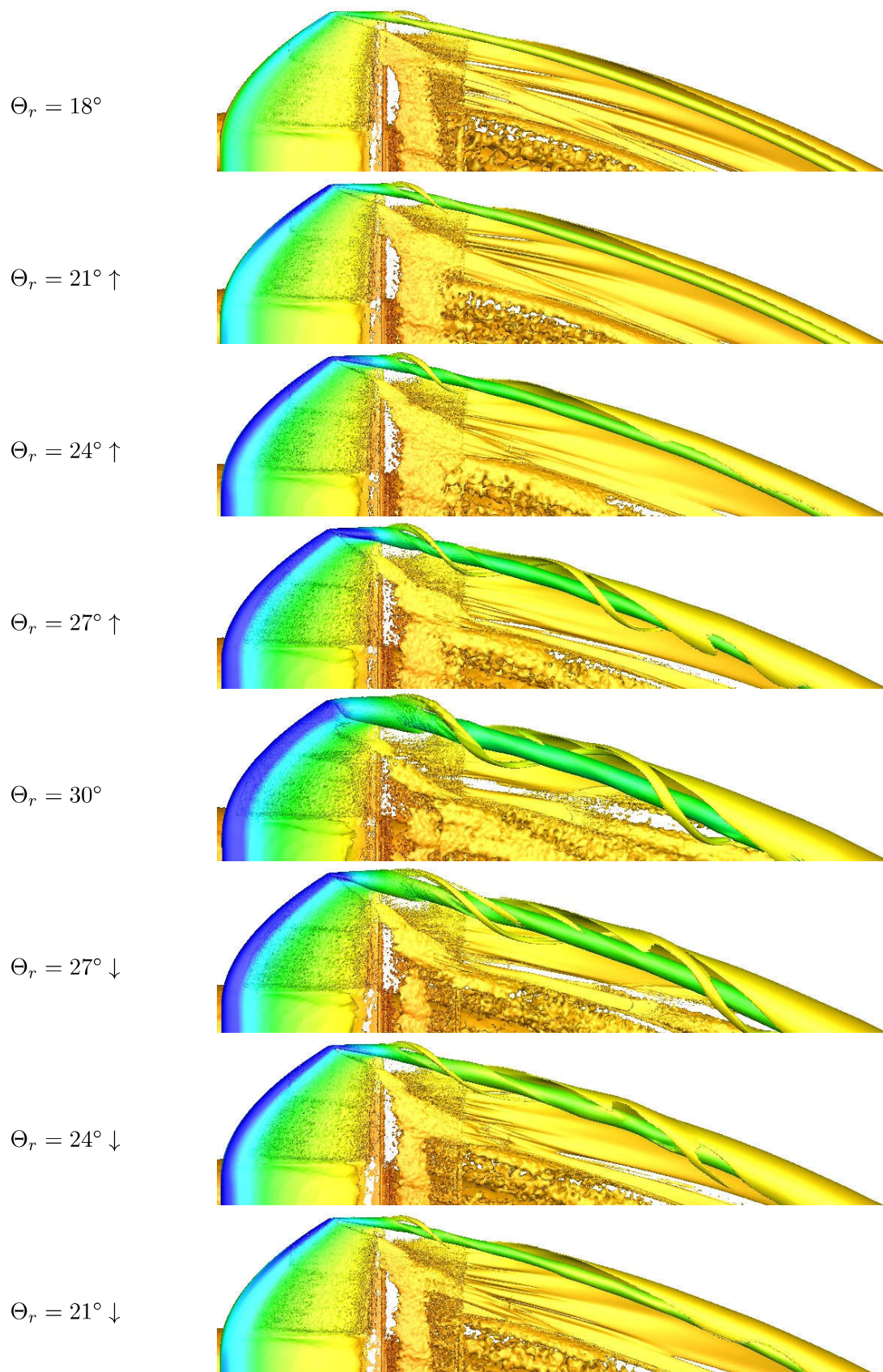


Figure 5.20: Close up view of the blade-tip vortex for eight different cases during an unsteady pitch motion.

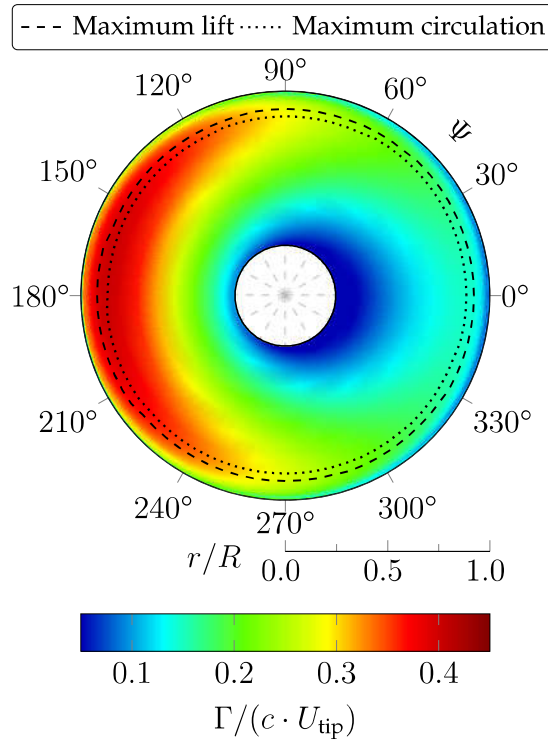


Figure 5.21: Blade circulation throughout a complete period.

assuming that the vortex slice stayed at a constant azimuthal angle in the laboratory frame, the propagation can easily be followed. At the intermediate angles ($\Theta_r = [21^\circ, 24^\circ, 27^\circ]$), the static vortices are surrounded by the unsteady vortices, with a nearly equal offset to each side, and vortices which were created during the upstroke motion have less downward convection than those created during the downstroke motion. At the minimum angle ($\Theta_r = 18^\circ$), the static vortex is roughly equivalent to the dynamic vortex, and at the maximum angle ($\Theta_r = 30^\circ$), the dynamic vortex is propagated further downward due to the higher lift in the unstalled flow. At the extrema, the upstroke/downstroke lines fall on top of each other.

The result above suggests strongly that the unsteady vortex can be modeled as an assembly of the static vortex states. In Fig. 5.23, the different vortex parameters are extracted in the case where the vortex at $\Psi_V = 45^\circ$ in each snapshot was produced when the rotor blade had the instantaneous pitch angle of $\Theta_r = 24^\circ$ and has thereafter been convected to that position, assuming that each slice remains at a constant azimuthal angle in the laboratory frame. The difference in the vertical position (a) and horizontal (b) position are not significantly high. The circulation (c) is constant for the static case and a steep decrease during the upstroke motion. A positive gradient results due to the downstroke motion. The increase of the radius (d) is diminished during the upstroke motion and enlarged during the downstroke motion. It can be seen that within the small errors produced by the lift hysteresis, that the position,

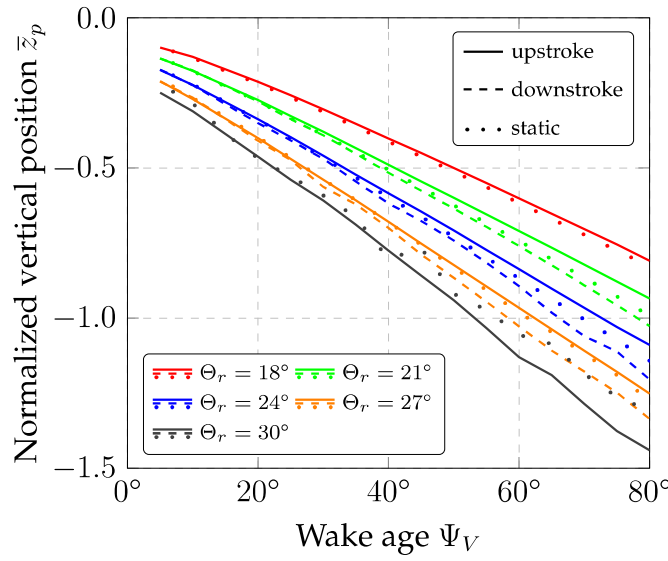


Figure 5.22: Vertical position of blade-tip vortex against wake age (curves display constant position approach, — line in Fig. 3.9).

circulation, and radius of the vortex are very similar for upstroke, downstroke, and static collective pitch at $\Psi_V = 45^\circ$. For the dynamic cases, the vortex changes, moving away from the crossing point associated with the nominal $\Theta_r = 24^\circ$ point at $\Psi_V = 45^\circ$, depending on whether the vortex strength is increasing or decreasing with time. This suggests that an approach that tracks the blade lift distribution at the moment of production and the aging of each slice through the propagating vortex should have a good chance of producing a physically correct vortex.

Figure 5.24 shows the normalized swirl velocity for dynamic and static test cases at a wake age of $\Psi_V = 40^\circ$. The dynamic results have been matched with the static test cases according to the angle of incidence during vortex creation. It can be seen that, disregarding the small hysteresis in the unsteady case, that the dynamic vortex shapes are well predicted by the static vortex shapes associated with the same angle of attack. Similarly, Fig. 5.25 shows the normalized axial velocity u_p/U_{tip} occurring in the center of the blade-tip vortex. Negative values characterize a reduction in flow speed relative to the blade as in a wake velocity deficit region. The axial velocity magnitude increases (in the negative direction) with an increasing angle of incidence, which is equivalent to a higher wake deficit. The downstroke situations have a weaker wake deficit. In contrast with the earlier investigation by Goerttler et al. [32] using URANS with a two-bladed rotor, which noted backward jetting associated with vortex breakdown occurring during high thrust and blade stall, here all axial velocities are negative. This is due to the lack of blade dynamic stall in the test cases investigated in this paper.

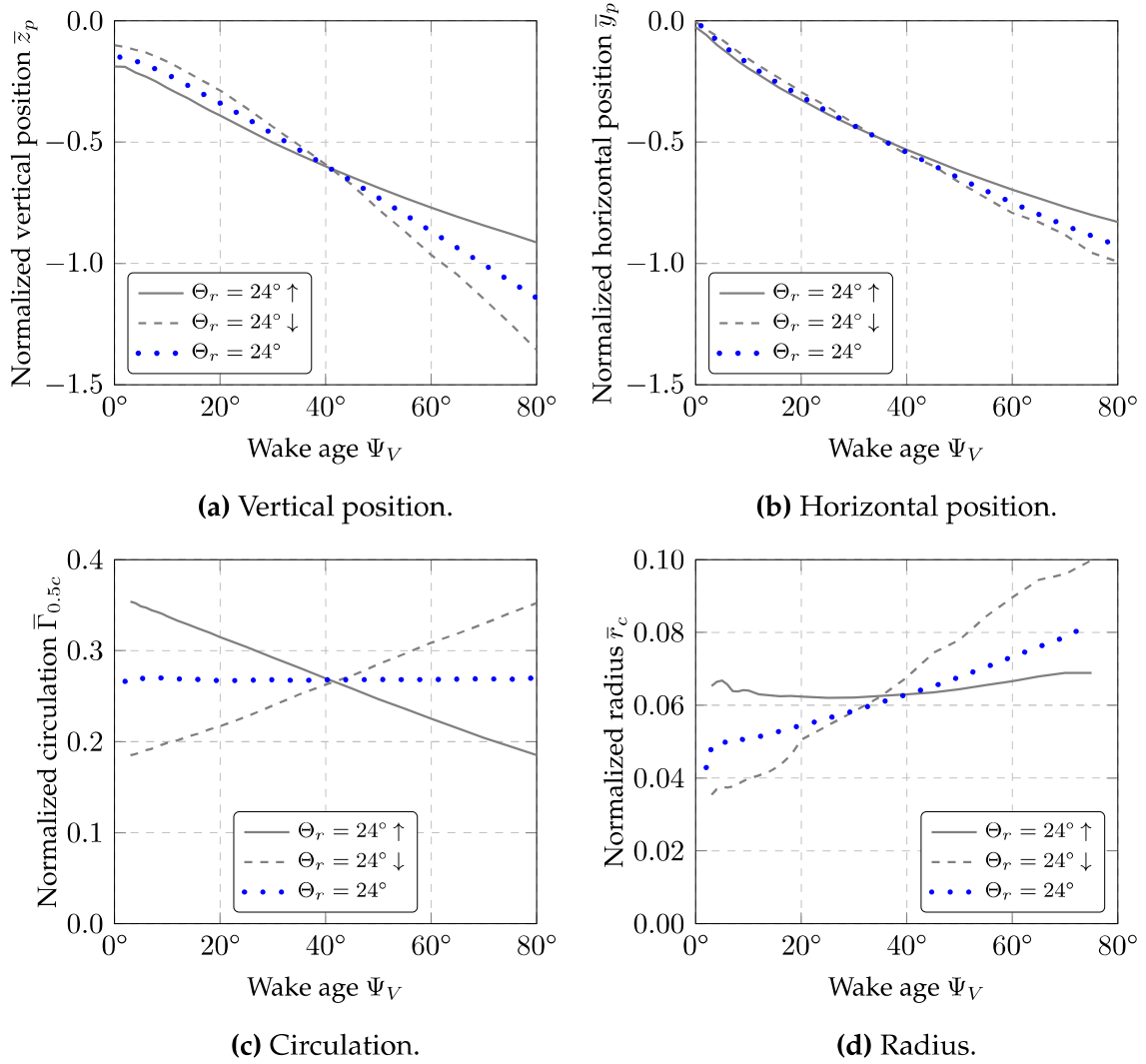


Figure 5.23: Vertical (a), horizontal (b) position, normalized circulation (c) and radius (d) of unsteady blade-tip vortex against wake age (unsteady curves display constant time approach, — line in Fig. 3.9).

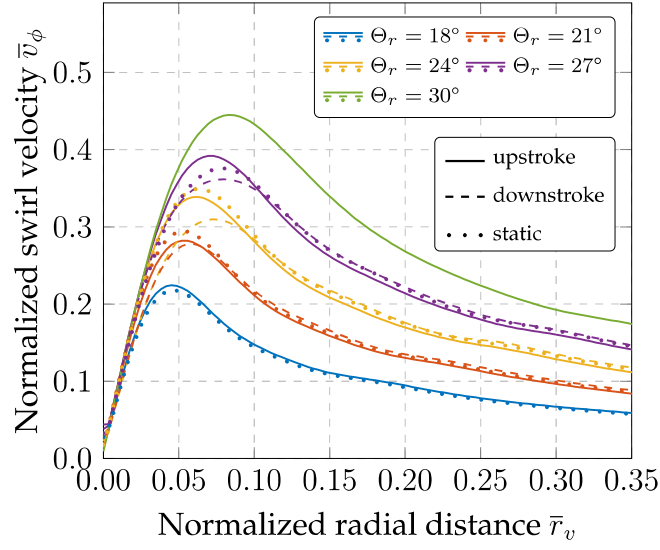


Figure 5.24: Normalized swirl velocity of blade-tip vortex over radial distance for different angles of incidence at $\Psi_V = 40^\circ$ (— = upstroke; --- = downstroke; ... = static).

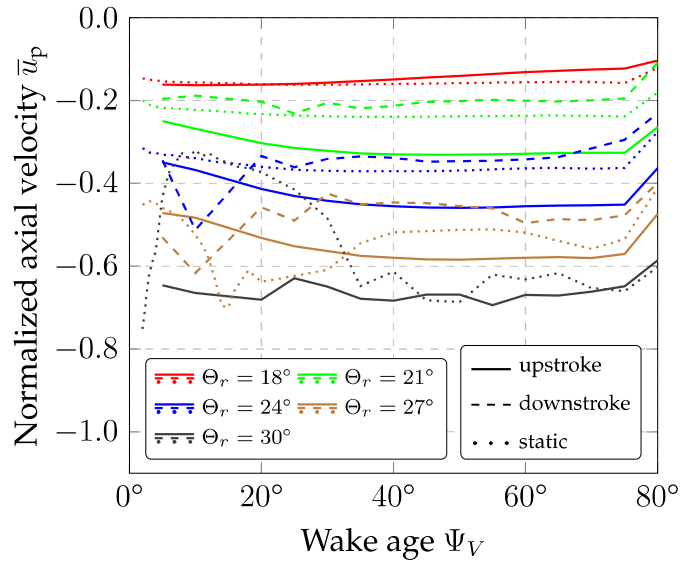


Figure 5.25: Normalized axial velocity inside the blade-tip vortex for different instants of time in the pitching cycle over the wake age (curves display constant position approach, — line in Fig. 3.9, — = upstroke; --- = downstroke).

Figure 5.26 displays the radius of the vortex core throughout an entire pitching cycle for two wake ages. The radius grows with increasing angle of incidence and is bigger, the higher the wake age. The static results are close to the values obtained during the upstroke (—) motion. After the maximum angle of incidence, the radius decreases again but remains at a higher level than on the upstroke, which agrees with the observation by Mohamed et al. [68] for a pitching blade.

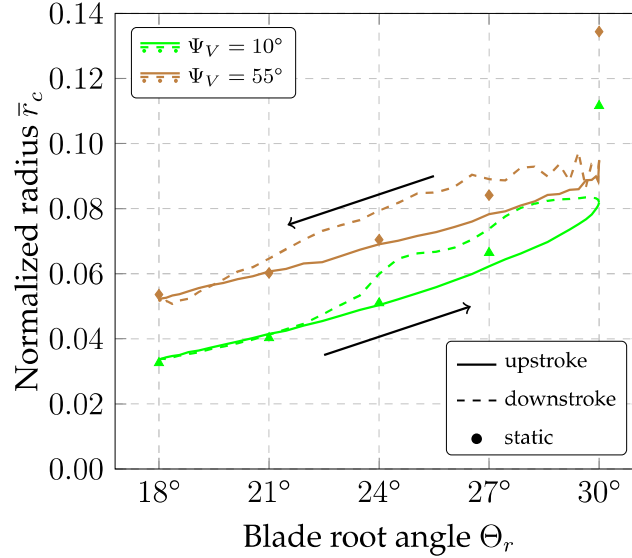


Figure 5.26: Normalized radius of blade-tip vortex throughout an entire pitching cycle for two wake ages (curves display constant wake age, — = upstroke; --- = downstroke; • = static).

5.8 Variation of the Reynolds number

Scaling rotor vortices is a particular problem and relevant since many investigations, for example Ref. [88], are only practicable in model-scale, and the results must be scaled. As a simple test, all parameters of the simulation were held constant, except the freestream pressure/density, which were increased by an order of magnitude. Figure 5.27 shows the results, which are each normalized with the relevant freestream density. Figure 5.27(a) displays a slightly higher circulation (2 – 4%) of the blade-tip vortex for the higher Reynolds number, which appears to be primarily due to the slightly higher thrust coefficient for the same pitching motion due to the change in boundary layer shape. Despite this, the vortex core radius is smaller for the higher Reynolds number, reducing in size by 2 – 5%. These results indicate that the Reynolds number is not a useful scaling parameter for vortices; thus, other values must be found.

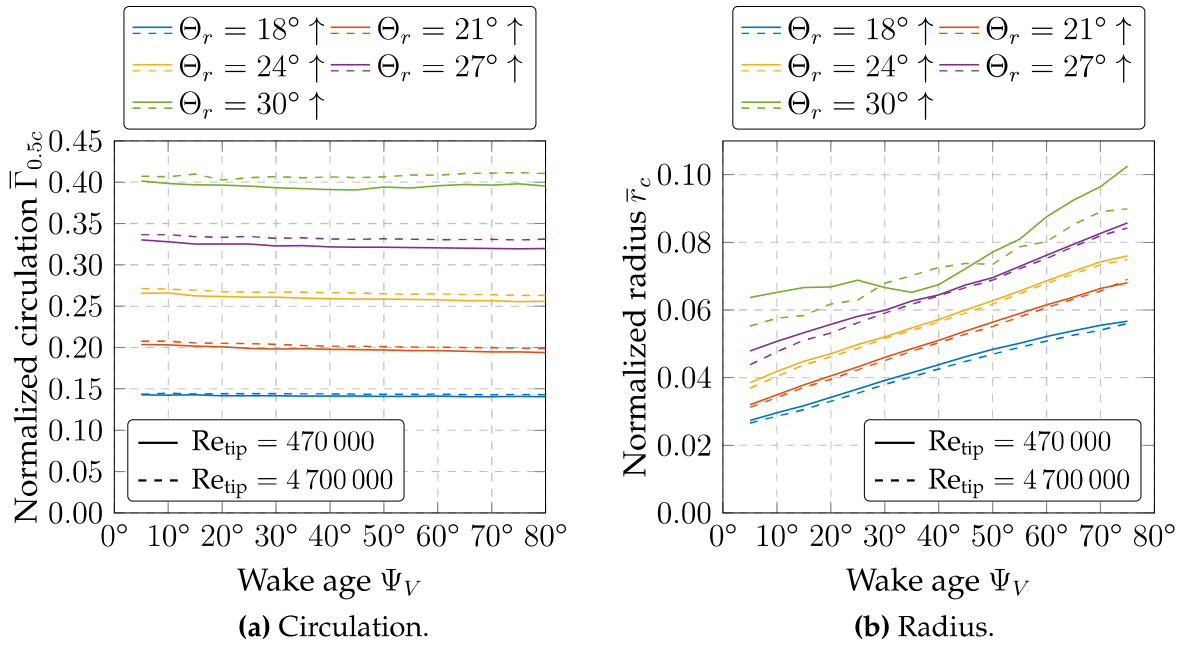


Figure 5.27: Normalized circulation and radius of blade-tip vortex for different instants of time in the pitching cycle over the wake age (curves display constant position approach, ■ line in Fig. 3.9, — = $Re_{tip} = 470\,000$; - - - = $Re_{tip} = 4\,700\,000$).

6 Conclusion

In this thesis, blade-tip vortices of a two-bladed and four-bladed rotor were investigated employing numerical URANS and DES simulations with DLR's finite-volume compressible-flow solver TAU. The static and unsteady pitching cases were simulated in attached as well as separated flow conditions. Grid and time-step studies were performed, leading to a structured block in the expected path of the vortex and a timewise resolution of $\Psi = 0.25^\circ$ in the blade rotation azimuth. The numerical results were compared with experimental data over a complete pitching cycle.

The subsequent analysis of all investigations demonstrates that the CFD simulations are capable of predicting flow structures during the generation and development of the tip-vortex in the near field of the blade. However, both structured and unstructured grids struggle to realistically compute more advanced vortices due to numerical dissipation.

A high cyclic pitch case of the two-bladed DSA-9A rotor was simulated with URANS. Separation around the peak angle and reattachment on the downstroke occur in this dynamic stall case. The experimental values fluctuate at these high angles of incidence and are not met by the simulated values. The numerical investigation of the four-bladed RTG rotor in axial flow with cyclic and collective pitch test cases was performed applying a fine grid using an LES model in the vortex region. These settings result in computed vortices that are comparable to those measured experimentally and do not display the rapid diffusion of vorticity seen in vortices computed with URANS solvers.

Algorithms deriving vortex parameters like radius, circulation, and position were implemented. Then, these parameters were analyzed and compared with experimental data. The main findings for both investigations researching the two-bladed and the four-bladed rotor present as follows:

1. The blade vorticity in the computations is correctly transported to the blade-tip vortex, as the numerical simulations are capable of matching the experimental circulation results at a vortex age of $\Psi_V = 2.6^\circ$ ($x/c = 0.41$). Furthermore, the numerical swirl-velocity distribution and the radius of the blade-tip vortex

match the experimental results. The maximum circulation on the blade predicts the vorticity in the vortex well. Up to 95% of this maximum circulation is contained within $r_v/c = 0.5$ around the vortex center and stays in this region, which, therefore, can be defined as the near field of the vortex.

2. The decay of the fully formed vortex is poorly modeled with the URANS approach. Correctly simulated circulation is found at $\Psi_V = 5.3^\circ$ ($x/c = 0.84$). However, numerical diffusion with a URANS solver leads to unphysically large vortex cores. Numerical diffusion is diminished and the convection of the vortex is more realistically simulated with the use of under-resolved LES models in specific areas. The radius of the vortex core decreases and aligns with the experimental data up to $\Psi_V = 15.3^\circ$.
3. Trimmed computations with similar thrust levels as in the experiment lead to a strong agreement in numerical and experimental data regarding the swirl-velocity distribution. Similarly, thrust ratio corrected results are in good agreement with the circulation and swirl-velocity distribution of the DES computations.
4. The unsteady vortex can be modeled as an assembly of static vortex states. The instantaneous vortex section produced by the rotor blade is comparable in the static and dynamic cases and can be followed as it convects downstream.
5. The position of the rotor-blade trailing-edge mainly drives the vertical location of the vortex core. The movement relative to the trailing edge is less than $0.05 c$. Therefore, the large pitching motion dominates the position of the descending vortex.
6. The wing-tip vortex becomes stronger with an increasing angle of incidence even after stalled flow on the wing. The reduction in the circulation of the blade-tip vortex, due to the blade stall, is delayed by more than $\Psi = 18^\circ$ compared to the lift coefficient.
7. The elliptical shape of the simulated vortex core changes into a circular shape with increasing wake age. The ratio of the two major axes increases from 0.85 to 0.96 within $\Delta\Psi_V = 2.7^\circ$ in attached flow conditions. The elliptical vortex shape rotates at approximately half the solid-body rotation speed of the core.

8. An error analysis quantifies the influence of misidentifying the vortex center position on the shape, radius, and swirl velocity to be small. A discrepancy in the location of up to a tenth of the vortex core reduces the radius by less than 0.5% and the swirl velocity by less than 1%. Furthermore, two orthogonal cuts are sufficient to determine the average radius by an error of less than 3%.

Research questions and outlook

This investigation compared several test cases with experimental data covering a complete pitching cycle. The analyzing possibilities of CFD can explain situations such as vortex breakdown, which are otherwise difficult to interpret using experimental data alone. Nevertheless, experimental runs support numerical solutions by validating specific cases. This symbiosis confidently answers the research questions of this thesis:

In summary, the results of the two major investigations indicate that the vorticity, which is required by the lift distribution, is contained in the near field of the vortex within $r_v/c = 0.5$. The swirl-velocity distributions of thrust trimmed simulations strongly agree with the experiments and, therefore, verify that the roll-up of the blade-tip vortex is correctly resolved.

Nevertheless, the numerical simulations struggle with vortex conservation. In particular when using URANS equations, the decay leads to significant differences even at relatively young wake ages. However, the use of LES models improves the agreement to the extent that the comparison at more advanced wake ages quantitatively matches the existing experimental data up to the particle void. Lastly, the time-varying vortices of a pitching blade can be modeled as an assembly of vortices of a hovering blade.

The findings of this study further deepen the understanding of blade-tip vortices. Comparisons with experimental results validate the different numerical approaches and demonstrate the areas of application by revealing the drawbacks. A DES solver, here a zonal LES approach, and a fine grid are necessary to get reasonable results. Based on the primary outcomes of this study, further investigations are conceivable. For example, the influence of the blade-tip geometry on the blade-tip vortex is promising. The scaling of results is of substantial interest to the community, and additional insights could be obtained by simulating more cases with different Reynolds numbers. Further investigations of similar nonrotating cases would fill the gap between 2D methods and the complete rotating approach. Finally, a particular focus on matching the incoming flow close to the rotor would lead to more significant comparisons and helpful insights into the strength of the blade-tip vortex.

References

- [1] J. U. Ahmad, G. K. Yamauchi, and D. L. Kao, “Comparison of Computed and Measured Vortex Evolution for a UH-60A Rotor in Forward Flight”, *31st AIAA Applied Aerodynamics Conference*, San Diego, California, 24–27 June 2013.
- [2] M. Allongue and J. P. Drevet, “New Rotor Test Rig in the Large Modane Wind Tunnel”, *15th European Rotorcraft Forum*, Amsterdam, The Netherlands, 12-15 Sept. 1989.
- [3] J. D. Anderson, *Fundamentals of Aerodynamics*, McGraw Hill International, 2007.
- [4] A. Bagai and J. G. Leishman, “Flow Visualization of Compressible Vortex Structures using Density Gradient Techniques”, *Experiments in Fluids*, Vol. **15**, No. 6, 1993, pp. 431–442, DOI: [10.1007/BF00191786](https://doi.org/10.1007/BF00191786).
- [5] A. Bagai and J. G. Leishman, “Rotor Free-Wake Modeling Using a Pseudo-Implicit Technique – Including Comparisons with Experimental Data”, *Journal of the American Helicopter Society*, Vol. **40**, No. 3, 1995, pp. 29–41, DOI: [10.4050/JAHS.40.29](https://doi.org/10.4050/JAHS.40.29).
- [6] A. Betz, “Verhalten von Wirbelsystemen”, *Zeitschrift fuer Angewandte Mathematik und Mechanik*, Vol. **12**, No. 3, see also TM 713, NACA, pp. 164–174.
- [7] M. J. Bhagwat and J. G. Leishman, “Correlation of Helicopter Rotor Tip Vortex Measurements”, *AIAA Journal*, Vol. **38**, No. 2, Feb. 2000, pp. 301–308, DOI: [10.2514/2.957](https://doi.org/10.2514/2.957).
- [8] M. J. Bhagwat and J. G. Leishman, “Generalized Viscous Vortex Model for Application to Free-Vortex Wake and Aeroacoustic Calculations”, *AHS 58th Annual Forum*, Montréal, Canada, 11–13 June 2002.
- [9] D. Birch and T. Lee, “Investigation of the Near-Field Tip Vortex behind an Oscillating Wing”, *Journal of Fluid Mechanics*, Vol. **544**, 2005, pp. 201–241, DOI: [10.1017/S0022112005006804](https://doi.org/10.1017/S0022112005006804).

- [10] D. Birch and T. Lee, "Tip Vortex Behind a Wing Oscillated with Small Amplitude", *Journal of Aircraft*, Vol. **42**, No. 5, 2005, pp. 1200–1208, DOI: [10.2514/1.11239](https://doi.org/10.2514/1.11239).
- [11] D. Birch and T. Lee, "Tip Vortex Behind a Wing Undergoing Deep-Stall Oscillation", *AIAA Journal*, Vol. **43**, No. 10, 2005, pp. 2081–2092, DOI: [10.2514/1.13139](https://doi.org/10.2514/1.13139).
- [12] D. Birch, T. Lee, F. Mokhtarian, and F. Kafyeke, "Structure and Induced Drag of a Tip Vortex", *Journal of Aircraft*, Vol. **41**, No. 5, 2004, pp. 1138–1145, DOI: [10.2514/1.2707](https://doi.org/10.2514/1.2707).
- [13] F. J. Brandsma, J. C. Kok, H. S. Dol, and A. Elsenaar, "Leading Edge Vortex Flow Computations and Comparison with DNW-HST Wind Tunnel Data", *RTO AVT Symposium on "Vortex Flows and High Angle of Attack"*, Loen, Norway, 7–11 May 2001.
- [14] J. N. Braukmann, A. Goerttler, C. C. Wolf, and M. Raffel, "Blade-Tip Vortex Characterization of a Rotor under Static and Cyclic Pitch Conditions Using BOS and PIV", *57th AIAA Aerospace Sciences Meeting*, San Diego, California, 7–11 Jan. 2019.
- [15] J. N. Braukmann, T. Schwermer, and C. C. Wolf, "Investigation of Young Blade-Tip Vortices at a Rotor Test Facility using Stereoscopic PIV", *25. Fachtagung "Experimentelle Strömungsmechanik"*, Karlsruhe, Germany, 5–7 Sept. 2017.
- [16] S. Braun, A. Uhl, B. Einfeld, and E. Stumpf, "Numerical Simulation of Vortex Roll-Up Processes Using the SSG/LRR- ω Model", in: *New Results in Numerical and Experimental Fluid Mechanics X*, Notes on Numerical Fluid Mechanics and Multidisciplinary Design 132, Springer International Publishing Switzerland, 2016, pp. 481–491, DOI: [10.1007/978-3-319-27279-5_42](https://doi.org/10.1007/978-3-319-27279-5_42).
- [17] C. L. Burley, T. F. Brooks, B. G. van der Wall, H. Richard, M. Raffel, P. Beaumier, Y. Delrieux, J. W. Lim, Y. H. Yu, C. Tung, K. Pentel, and E. Mercker, "Rotor Wake Vortex Definition - Initial Evaluation of 3-C PIV Results of the HART-II Study", *28th European Rotorcraft Forum*, Bristol, England, 17–20 Sept. 2002.
- [18] F. X. Caradonna and C. Tung, "Experimental and Analytical Studies of a Model Helicopter Rotor in Hover", *Sixth European Rotorcraft and Powered Lift Aircraft Forum*, 25, Bristol, England, 16–19 Sept. 1980.
- [19] CENTAURTM Software, www.centaurosoft.com, 2019.

- [20] N. M. Chaderjian, "Navier-Stokes Simulation of UH-60A Rotor/Wake Interaction Using Adaptive Mesh Refinement", *AHS 73rd Annual Forum*, Fort Worth, Texas, 9–11 May 2017.
- [21] N. M. Chaderjian and P. G. Buning, "High Resolution Navier-Stokes Simulation of Rotor Wakes", *AHS 67th Annual Forum*, Virginia Beach, Virginia, 3–5 May 2011.
- [22] J. S. Chow, G. G. Zilliac, and P. Bradshaw, "Mean and Turbulence Measurements in the Near Field of a Wingtip Vortex", *AIAA Journal*, Vol. **35**, No. 10, 1997, pp. 1561–1567, DOI: [10.2514/2.1](https://doi.org/10.2514/2.1).
- [23] M. J. Churchfield and G. A. Blaisdell, "Numerical Simulations of a Wingtip Vortex in the Near Field", *Journal of Aircraft*, Vol. **46**, No. 1, 2009, pp. 230–243, DOI: [10.2514/1.38086](https://doi.org/10.2514/1.38086).
- [24] J. Dacles-Mariani, G. G. Zilliac, J. S. Chow, and P. Bradshaw, "Numerical/Experimental Study of a Wingtip Vortex in the Near Field", *AIAA Journal*, Vol. **33**, No. 9, Sept. 1995, pp. 1561–1568, DOI: [10.2514/3.12826](https://doi.org/10.2514/3.12826).
- [25] W. J. Devenport, M. C. Rife, S. I. Liapis, and G. J. Follin, "The Structure and Development of a Wing-Tip Vortex", *Journal of Fluid Mechanics*, Vol. **312**, Apr. 1996, pp. 67–106, DOI: [10.1017/S0022112096001929](https://doi.org/10.1017/S0022112096001929).
- [26] K. Duraisamy, M. Ramasamy, J. D. Baeder, and J. G. Leishman, "High-Resolution Computational and Experimental Study of Rotary-Wing Tip Vortex formation", *AIAA Journal*, Vol. **45**, No. 11, Nov. 2007, pp. 2593–2602, DOI: [10.2514/1.26575](https://doi.org/10.2514/1.26575).
- [27] A. D. Gardner and K. Richter, "Influence of Rotation on Dynamic Stall", *Journal of the American Helicopter Society*, Vol. **58**, No. 032001, 2013, pp. 1–9, DOI: [10.4050/JAHS.58.032001](https://doi.org/10.4050/JAHS.58.032001).
- [28] D. J. Garmann and M. R. Visbal, "Dynamics of Revolving Wings for Various Aspect Ratios", *Journal of Fluid Mechanics*, Vol. **748**, 2014, pp. 932–956, DOI: [10.1017/jfm.2014.212](https://doi.org/10.1017/jfm.2014.212).
- [29] D. J. Garmann and M. R. Visbal, "Further Investigations of the Tip Vortex on an Oscillating NACA0012 Wing", *46th AIAA Fluid Dynamics Conference*, Washington, D.C., 13–18 June 2016, DOI: [10.2514/6.2016-4343](https://doi.org/10.2514/6.2016-4343).
- [30] D. J. Garmann and M. R. Visbal, "Investigation of the Unsteady Tip Vortex Structure on a NACA0012 Wing at Fixed Incidence", *55th AIAA Aerospace Sciences Meeting*, Grapevine, Texas, 9–13 Jan. 2017, DOI: [10.2514/6.2017-1002](https://doi.org/10.2514/6.2017-1002).

- [31] D. J. Garmann and M. R. Visbal, "Unsteady Evolution of the Tip Vortex on a Stationary and Oscillating NACA0012 Wing", *54th AIAA Aerospace Sciences Meeting*, San Diego, California, 4–8 Jan. 2016, DOI: [10.2514/6.2016-0328](https://doi.org/10.2514/6.2016-0328).
- [32] A. Goerttler, J. N. Braukmann, T. Schwermer, A. D. Gardner, and M. Raffel, "Tip-Vortex Investigation on a Rotating and Pitching Rotor Blade", *Journal of Aircraft*, Vol. 55, No. 5, 2018, pp. 1792–1804, DOI: [10.2514/1.C034693](https://doi.org/10.2514/1.C034693).
- [33] A. Goerttler, J. N. Braukmann, C. C. Wolf, A. D. Gardner, and M. Raffel, "Blade Tip-Vortices of a Four-Bladed Rotor in Hover and Unsteady Conditions", *VFS 75th Annual Forum*, Philadelphia, Pennsylvania, 13–16 May 2019.
- [34] R. B. Gray, "An Aerodynamic Analysis of a Single-Bladed Rotor in Hovering and Forward Flight as determined by Smoke Studies on the Vorticity Distribution in the Wake", Princeton University, Aeronautical Engineering Department, Report No. 356, 1956.
- [35] R. B. Gray, H. M. McMahon, K. R. Shenoy, and M. L. Hammer, "Surface Pressure Measurements at Two Tips of a Model Helicopter Rotor in Hover", NASA CR-3281, 1980.
- [36] I. Gursul, R. Gordnier, and M. Visbal, "Unsteady Aerodynamics of Nonslender Delta Wings", *Progress in Aerospace Sciences*, Vol. 41, No. 7, 2005, pp. 515–557, DOI: [10.1016/j.paerosci.2005.09.002](https://doi.org/10.1016/j.paerosci.2005.09.002).
- [37] J. Heineck, G. Yamauchi, A. Wadcock, L. Lourenco, and A. Abrego, "Application of Three-Component PIV to a Hovering Rotor Wake", *American Helicopter Society 56th Annual Forum*, Virginia Beach, Virginia, 2–4 May 2000.
- [38] H. v. Helmholtz, "Über Integrale der Hydrodynamischen Gleichungen, welche der Wirbelbewegung entsprechen, [Engl: On the Integrals of the Hydrodynamical Equations, which Express Vortex Movement]", *J. für die reine und angewandte Mathematik*, Vol. 55, 1858, pp. 22–55.
- [39] F. Hoffmann, B. G. van der Wall, and J. Yin, "The Physics behind BVI Noise Reduction in Descent Flight through the Use of Dynamic Active Twist Control", *AHS 74th Annual Forum*, Phoenix, Arizona, 14–17 May 2018.
- [40] J. D. Iversen, "Correlation of Turbulent Trailing Vortex Decay Data", *Journal of Aircraft*, Vol. 13, No. 5, May 1976, pp. 338–342, DOI: [10.2514/3.44529](https://doi.org/10.2514/3.44529).
- [41] R. Jain, "Hover Predictions on the S-76 Rotor with Tip Shape Variation Using Helios", *Journal of Aircraft*, Vol. 55, No. 1, 2018, DOI: [10.2514/1.C034075](https://doi.org/10.2514/1.C034075).

- [42] B. Jayaraman and M. Potsdam, “Effet of Fuselage and Wind Tunnel Wall on Full-Scale UH-60A Rotor Tip Vortex Prediction”, *34th AIAA Applied Aerodynamics Conference*, Washington, D.C., 13–17 June 2016, DOI: [10.2514/6.2016-3131](https://doi.org/10.2514/6.2016-3131).
- [43] J. Jeong and F. Hussain, “On the Identification of a Vortex”, *Journal of Fluid Mechanics*, Vol. **285**, 1995, pp. 69–94, DOI: [10.1017/S0022112095000462](https://doi.org/10.1017/S0022112095000462).
- [44] A. Joulain, D. Desvigne, D. Alfano, and T. Leweke, “Numerical Investigation of the Vortex Roll-Up from a Helicopter Blade Tip using a Novel Fixed-Wing Adaption Method”, *CEAS Aeronautical Journal*, Vol. **8**, No. 2, 2017, pp. 245–260, DOI: [10.1007/s13272-016-0234-z](https://doi.org/10.1007/s13272-016-0234-z).
- [45] K. Kaufmann, M. Costes, F. Richez, A. D. Gardner, and A. Le Pape, “Numerical Investigation of Three-Dimensional Dynamic Stall on an Oscillating Finite Wing”, *Journal of the American Helicopter Society*, Vol. **60**, No. 3, 2015, pp. 1–12, DOI: [10.4050/JAHS.60.032004](https://doi.org/10.4050/JAHS.60.032004).
- [46] K. Kaufmann, C. B. Merz, and A. D. Gardner, “Dynamic Stall Simulations on a Pitching Finite Wing”, *Journal of Aircraft*, Vol. **54**, No. 4, 2017, pp. 1303–1316, DOI: [10.2514/1.C034020](https://doi.org/10.2514/1.C034020).
- [47] K. Kaufmann, C. C. Wolf, C. B. Merz, and A. D. Gardner, “Numerical Investigation of Blade-Tip-Vortex Dynamics”, *CEAS Aeronautical Journal*, Vol. **9**, No. 1, 2018, pp. 373–386, DOI: [10.1007/s13272-018-0287-2](https://doi.org/10.1007/s13272-018-0287-2).
- [48] W. Kaufmann, “Über die Ausbreitung Kreiszyklindrischer Wirbel in Zähnen (Viskosen) Flüssigkeiten, [Engl: On the Propagation of Cylindrical Vortices in Viscous Fluids]”, *Ingenieur-Archiv*, Vol. **31**, No. 1, 1962, DOI: [10.1007/BF00538235](https://doi.org/10.1007/BF00538235).
- [49] J. M. Kim, N. M. Komerath, and S. G. Liou, “Vorticity Concentration at the Edge of the Inboard Vortex Sheet”, *Journal of the American Helicopter Society*, Vol. **39**, No. 2, 1994, pp. 30–34, DOI: <https://doi.org/10.4050/JAHS.39.30>.
- [50] K. Kindler, K. Mulleners, H. Richard, B. G. van der Wall, and M. Raffel, “Aperiodicity in the Near Field of Full-Scale Rotor Blade Tip Vortices”, *Experiments in Fluids*, Vol. **50**, No. 6, 2011, pp. 1601–1610, DOI: [10.1007/BF00191786](https://doi.org/10.1007/BF00191786).
- [51] A. N. Kolmogorov, “Dissipation of Energy in the Locally Isotropic Turbulence”, *Dokl. Akad. Nauk SSSR*, Vol. **32**, No. 1, 1941, see also *Proc. R. Soc. Lond. A*, Vol. **434**, No. 1890, 1991, pp. 15–17, DOI: [10.1098/rspa.1991.0076](https://doi.org/10.1098/rspa.1991.0076).

- [52] A. N. Kolmogorov, "The Local Structure of Turbulence in Incompressible Viscous Fluid for very large Reynolds Numbers", *Dokl. Akad. Nauk SSSR*, Vol. **30**, No. 4, 1941, see also *Proc. R. Soc. Lond. A*, Vol. **434**, No. 1890, 1991, pp. 9-13, DOI: [10.1098/rspa.1991.0075](https://doi.org/10.1098/rspa.1991.0075).
- [53] N. Komerath, O. Wong, and B. Ganesh, "On the Formation and Decay of Rotor Blade Tip Vortices", *34th AIAA Fluid Dynamics Conference Exhibit*, Portland, Oregon, 28 June – 1 July 2004.
- [54] H. Lamb, *Hydrodynamics*, 6th, Cambridge University Press, Cambridge, UK, 1932.
- [55] A. J. Landgrebe, "The Wake Geometry of a Hovering Helicopter Rotor and Its Influence on Rotor Performance", *Journal of the American Helicopter Society*, Vol. **17**, No. 4, 1972, pp. 3–15, DOI: [10.4050/JAHS.17.3](https://doi.org/10.4050/JAHS.17.3).
- [56] J. G. Leishman, *Principles of Helicopter Aerodynamics*, Second Edition, Cambridge University Press, 2006.
- [57] J. G. Leishman and A. Bagai, "Challenges in Understanding the Vortex Dynamics of Helicopter Rotor Wakes", *AIAA Journal*, Vol. **36**, No. 7, 1998, pp. 1130–1140, DOI: [10.2514/2.510](https://doi.org/10.2514/2.510).
- [58] J. G. Leishman, A. Baker, and A. Coyne, "Measurements of Rotor Tip Vortices Using Three-Component Laser Doppler Velocimetry", *Journal of the American Helicopter Society*, Vol. **41**, No. 4, 1996, pp. 342–353, DOI: [10.4050/JAHS.41.342](https://doi.org/10.4050/JAHS.41.342).
- [59] J. Letzgus, A. D. Gardner, T. Schwermer, M. Keßler, and E. Krämer, "Numerical Investigations of Dynamic Stall on a Rotor with Cyclic Pitch Control", *Journal of the American Helicopter Society*, Vol. **64**, No. 1, 2019, pp. 1–14, DOI: [10.4050/JAHS.64.012007](https://doi.org/10.4050/JAHS.64.012007).
- [60] J. Letzgus, M. Keßler, and E. Krämer, "CFD-Simulation of Three-Dimensional Dynamic Stall on a Rotor with Cyclic Pitch Control", *41st European Rotorcraft Forum*, Munich, 1–4 Sept. 2015.
- [61] Z. Lietzau, M. Ramasamy, R. Jain, J. G. Leishman, and J. Ekaterinas, "Comparison of Advanced RANS Modeling with Dual-Plane PIV Measurements for a Hovering Rotor", *AHS 73rd Annual Forum*, Fort Worth, Texas, 9–11 May 2017.
- [62] J. E. W. Lombard, D. Moxey, and S. J. Sherwin, "Implicit Large-Eddy Simulation of a Wingtip Vortex", *AIAA Journal*, Vol. **54**, No. 2, 2016, pp. 506–518, DOI: [10.2514/1.J054181](https://doi.org/10.2514/1.J054181).

- [63] J. Löwe, A. Probst, T. Knopp, and R. Kessler, “Low-Dissipation Low-Dispersion Second-Order Scheme for Unstructured Finite Volume Flow Solvers”, *AIAA Journal*, Vol. **54**, No. 10, 2016, pp. 2972–2987, DOI: [10.2514/1.J054956](https://doi.org/10.2514/1.J054956).
- [64] F. R. Menter, “Two-Equation Eddy-Viscosity Turbulence Models for Engineering Applications”, *AIAA Journal*, Vol. **32**, No. 8, 1994, pp. 1598–1605, DOI: [10.2514/3.12149](https://doi.org/10.2514/3.12149).
- [65] F. R. Menter, “Zonal Two Equation $k-\omega$ Turbulence Models for Aerodynamic Flows”, *AIAA 93-2906, 23rd AIAA Fluid Dynamics, Plasma Dynamics, and Lasers Conference*, Orlando, Florida, 6–9 July 1993.
- [66] C. B. Merz, C. C. Wolf, R. K., K. Kaufmann, A. Mielke, and M. Raffel, “Spanwise Differences in Static and Dynamic Stall on a Pitching Rotor Blade Tip Model”, *Journal of the American Helicopter Society*, Vol. **62**, No. 1, 2017, pp. 1–11, DOI: [10.4050/JAHS.62.012002](https://doi.org/10.4050/JAHS.62.012002).
- [67] J. Milluzzo and J. G. Leishman, “Development of the Turbulent Vortex Sheet in the Wake of a Hovering Rotor”, *AHS 69th Annual Forum*, Phoenix, Arizona, 21–23 May 2013.
- [68] K. Mohamed, S. Nadarajah, and M. Paraschivoiu, “Detached-Eddy Simulation of a Wing Tip Vortex at Dynamic Stall Conditions”, *Journal of Aircraft*, Vol. **46**, No. 4, 2009, pp. 1302–1313, DOI: [10.2514/1.40685](https://doi.org/10.2514/1.40685).
- [69] R. Nilifard, A. Zanotti, G. Gibertini, A. Guardone, and G. Quaranta, “Numerical Investigation of Three-Dimensional Effects on Deep Dynamic Stall Experiments”, *AHS 71st Annual Forum*, Virginia Beach, Virginia, 5–7 May 2015.
- [70] C. Öhrle, U. Schäferlein, M. Keßler, and E. Krämer, “Higher-Order Simulations of a Compound Helicopter using Adaptive Mesh Refinement”, *AHS 74th Annual Forum*, Phoenix, Arizona, 14–17 May 2018.
- [71] C. W. Oseen, “Über Wirbelbewegung in einer reibenden Flüssigkeit, [Engl: On the Vortex Movement in a Viscous Fluid]”, *Arkiv för matematik, astronomi och fysik*, Vol. **7**, No. 14, 1911, pp. 14–21.
- [72] M. Potsdam, H. Yeo, and W. Johnson, “Rotor Airloads Prediction Using Loose Aerodynamic/Structural Coupling”, *Journal of Aircraft*, Vol. **43**, No. 3, 2006, DOI: [10.2514/1.14006](https://doi.org/10.2514/1.14006).
- [73] M. Potsdam, P. Cross, and M. Hill, “Assessment of CREATE™-AV Helios for Complex Rotating Hub Wakes”, *AHS 73rd Annual Forum*, Fort Worth, Texas, 9–11 May 2017.

- [74] M. Potsdam and B. Jayaraman, "UH-60A Rotor Tip Vortex Prediction and Comparison to Full-Scale Wind Tunnel Measurements", *AHS 70th Annual Forum*, Montréal, Canada, 20–22 May 2014.
- [75] A. Probst, J. Löwe, S. Reuß, T. Knopp, and R. Kessler, "Scale-Resolving Simulations with a Low-Dissipation Low-Dispersion Second-Order Scheme for Unstructured Flow Solvers", *AIAA Journal*, Vol. **54**, No. 10, 2016, pp. 2972–2987, DOI: [10.2514/1.J054957](https://doi.org/10.2514/1.J054957).
- [76] M. Raffel, A. Bauknecht, M. Ramasamy, G. K. Yamauchi, J. T. Heineck, and L. N. Jenkins, "Contributions of Particle Image Velocimetry to Helicopter Aerodynamics", *AIAA Journal*, Vol. **55**, No. 9, 2017, pp. 2859–2874, DOI: [10.2514/1.J055571](https://doi.org/10.2514/1.J055571).
- [77] M. Raffel, U. Seelhorst, and C. Willert, "Vortical Flow Structures at a Helicopter Rotor Model Measured by LDV and PIV", *The Aeronautical Journal*, Vol. **102**, No. 1014, Apr. 1998, pp. 221–227.
- [78] M. Ramasamy, B. Johnson, T. Huismann, and J. G. Leishman, "Digital Particle Image Velocimetry Measurements of Tip Vortex Characteristics Using an Improved Aperiodicity Correction", *Journal of the American Helicopter Society*, Vol. **54**, No. 1, 2009, pp. 1–13, DOI: [10.4050/JAHS.54.012004](https://doi.org/10.4050/JAHS.54.012004).
- [79] M. Ramasamy, B. Johnson, and J. G. Leishman, "Turbulent Tip Vortex Measurements using Dual-Plane Stereoscopic Particle Image Velocimetry", *AIAA Journal*, Vol. **47**, No. 8, 2009, pp. 1826–1840, DOI: [10.2514/1.39202](https://doi.org/10.2514/1.39202).
- [80] M. Ramasamy and J. G. Leishman, "A Generalized Model for Transitional Blade Tip Vortices", *Journal of the American Helicopter Society*, Vol. **51**, No. 1, Jan. 2006, pp. 92–103, DOI: [10.4050/1.3092881](https://doi.org/10.4050/1.3092881).
- [81] M. Ramasamy and J. G. Leishman, "A Reynolds Number-Based Blade Tip Vortex Model", *Journal of the American Helicopter Society*, Vol. **52**, No. 3, July 2007, pp. 214–223, DOI: [10.4050/JAHS.52.214](https://doi.org/10.4050/JAHS.52.214).
- [82] M. Ramasamy, S. Wilson Jacob, W. J. McCroskey, and P. B. Martin, "Measured Characteristics of Cycle-To-Cycle Variations in Dynamic Stall", *AHS Technical Meeting on Aeromechanics Design for Vertical Lift*, San Francisco, California, 20–22 Jan. 2016.
- [83] W. J. M. Rankine, *Manual of Applied Mechanics*, Griffin, 1876.
- [84] H. Richard and B. G. van der Wall, "Detailed Investigation of Rotor Blade Tip Vortex in Hover Condition by 2C and 3C-PIV", *32nd European Rotorcraft Forum*, Maastricht, The Netherlands, 12–14 Sept. 2002.

- [85] F. Richez, “Analysis of Dynamic Stall Mechanisms in Helicopter Rotor Environment”, *Journal of the American Helicopter Society*, Vol. **63**, No. 2, 2018, pp. 1–11, DOI: [10.4050/JAHS.63.022006](https://doi.org/10.4050/JAHS.63.022006).
- [86] V. J. Rossow, “On the Inviscid Rolled-Up Structure of Lift-Generated Vortices”, *Journal of Aircraft*, Vol. **10**, No. 11, 1973, pp. 647–650, DOI: [10.2514/3.60277](https://doi.org/10.2514/3.60277).
- [87] D. Schwamborn, A. D. Gardner, H. von Geyr, A. Krumbein, H. Lüdeke, and A. Stürmer, “Development of the TAU-Code for Aerospace Applications”, *50th International Conference on Aerospace Science and Technology*, 26–28 June 2008.
- [88] C. Schwarz, A. Bauknecht, S. Mailänder, and M. Raffel, “Wake Characterization of a Free-Flying Model Helicopter in Ground Effect”, *Journal of the American Helicopter Society*, Vol. **64**, No. 1, 2019, pp. 1–16, DOI: [10.4050/JAHS.64.012010](https://doi.org/10.4050/JAHS.64.012010).
- [89] T. Schwermer, “Experimentelle Untersuchung des Dynamischen Strömungsabrisses an einem Rotor mit Axialer Zuströmung, [Engl: Dynamic Stall Experiments on a Rotor in Axial Inflow]”, PhD thesis, Dissertation, Gottfried Wilhelm Leibniz Universität Hannover, 2018.
- [90] T. Schwermer, A. D. Gardner, and M. Raffel, “A Novel Experiment to Understand the Dynamic Stall Phenomenon in Rotor Axial Flight”, *Journal of the American Helicopter Society*, Vol. **64**, No. 1, 2019, pp. 1–11, DOI: [10.4050/JAHS.64.012004](https://doi.org/10.4050/JAHS.64.012004).
- [91] T. Schwermer, K. Richter, and M. Raffel, “Development of a Rotor Test Facility for the Investigation of Dynamic Stall”, in: *New Results in Numerical and Experimental Fluid Mechanics X*, Notes on Numerical Fluid Mechanics and Multidisciplinary Design 132, Springer International Publishing Switzerland, 2016, pp. 663–673, DOI: [10.1007/978-3-319-27279-5_58](https://doi.org/10.1007/978-3-319-27279-5_58).
- [92] M. Scully and J. P. Sullivan, “Helicopter Rotor Wake Geometry and Airloads and Development of Laser Doppler Velocimeter for Use in Helicopter Rotor Wakes”, Massachusetts Institute of Technology, Aerophysics Laboratory, Technical Report 179, 1972.
- [93] M. L. Shur, P. R. Spalart, M. K. Strelets, and A. K. Travin, “A Hybrid RANS-LES Approach with Delayed-DES and Wall-Modelled LES Capabilities”, *International Journal of Heat and Fluid Flow*, Vol. **29**, No. 6, 2008, pp. 1638–1649, DOI: [10.1016/j.ijheatfluidflow.2008.07.001](https://doi.org/10.1016/j.ijheatfluidflow.2008.07.001).

- [94] M. L. Shur, M. K. Strelets, A. K. Travin, and P. R. Spalart, "Turbulence Modeling in Rotating and Curved Channels: Assessing the Spalart-Shur Correction", *AIAA Journal*, Vol. **38**, No. 5, 2000, pp. 784–792, DOI: [10.2514/2.1058](https://doi.org/10.2514/2.1058).
- [95] J. P. Slotnick, A. Khodadoust, J. J. Alonso, D. L. Darmofal, W. D. Gropp, E. A. Lurie, and D. J. Mavriplis, "CFD Vision 2030 Study: A Path to Revolutionary Computational Aerosciences", NASA Technical Report, NASA/CR-2014-218178, 2014.
- [96] J. Smagorinsky, "General Circulation Experiments with the Primitive Equations: 1. The Basic Experiment", *Mon. Weather Review*, Vol. **91**, No. 3, 1963, pp. 99–164.
- [97] P. R. Spalart, "Strategies for Turbulence Modelling and Simulations", *International Journal of Heat and Fluid Flow*, Vol. **21**, No. 3, 2000, pp. 252–263, DOI: [10.1016/S0142-727X\(00\)00007-2](https://doi.org/10.1016/S0142-727X(00)00007-2).
- [98] P. R. Spalart and S. R. Allmaras, "A One-Equation Turbulence Model for Aerodynamic Flows", *30th Aerospace Sciences Meeting and Exhibit*, 1992, DOI: [10.2514/6.1992-439](https://doi.org/10.2514/6.1992-439).
- [99] P. R. Spalart, S. Deck, M. L. Shur, K. D. Squires, M. K. Strelets, and A. Travin, "A New Version of Detached-Eddy Simulation, Resistant to Ambiguous Grid Densities", *Theoretical and Computational Fluid Dynamics*, Vol. **20**, No. 3, 2006, pp. 181–195, DOI: [10.1007/s00162-006-0015-0](https://doi.org/10.1007/s00162-006-0015-0).
- [100] P. R. Spalart, J. W-H., M. Strelets, and S. Allmaras, "Comments on the Feasibility of LES for Wings, and on a Hybrid RANS/LES Approach", *First AFOSR International Conference on DNS/LES*, Ruston, Louisiana, 4-8 Aug. 1997.
- [101] A. Spentzos, G. Barakos, K. Badcock, and B. Richards, "CFD Study of 3-D Dynamic Stall", *43rd AIAA Aerospace Sciences Meeting*, Reno, Nevada, 10–13 Jan. 2005, DOI: [10.2514/6.2005-1107](https://doi.org/10.2514/6.2005-1107).
- [102] H. B. Squire, "The Growth of a Vortex in Turbulent Flow", *Aeronautical Quarterly*, Vol. **16**, No. 3, 1965, pp. 302–306, DOI: [10.1017/S0001925900003516](https://doi.org/10.1017/S0001925900003516).
- [103] G. R. Srinivasan and W. J. McCroskey, "Navier-Stokes Calculations of Hovering Rotor Flowfields", *Journal of Aircraft*, Vol. **25**, No. 10, 1988, pp. 865–874, DOI: [10.2514/3.45673](https://doi.org/10.2514/3.45673).
- [104] G. G. Stokes, "On the Theories of the Internal Friction of Fluids in Motion, and of the Equilibrium and Motion of Elastic Solids", *Proceedings - Cambridge Philosophical Society. Mathematical and physical sciences*. 1845.

- [105] P. G. Tait, "Translation of (Helmholtz 1858): On the Integrals of the Hydrodynamical Equations, which Express Vortex-Motion", *Philosophical Magazine* 1867.
- [106] T. L. Thompson, N. M. Komerath, and R. B. Gray, "Visualization and Measurement of the Tip Vortex Core of a Rotor Blade in Hover", *Journal of Aircraft*, Vol. **25**, No. 12, 1988, pp. 1113–1121, DOI: [10.2514/3.45710](https://doi.org/10.2514/3.45710).
- [107] A. Travin, M. Shur, M. Strelets, and P. Spalart, "Physical and Numerical Upgrades in the Detached-Eddy Simulation of Complex Turbulent Flows", in: *Advances in LES of Complex Flows*, Fluid Mechanics and its Applications, Kluwer Academic Publishers, 2002, pp. 239–254, DOI: [10.1007/0-306-48383-1_16](https://doi.org/10.1007/0-306-48383-1_16).
- [108] S. Uluocak, H. A. Hazaveh, M. Perçin, M. T. Akpolat, and O. Uzol, "Experimental Investigation of the Effects of Different Helicopter Rotor Tip Geometries on Aerodynamic Performance and Tip Vortex Characteristics", *44th European Rotorcraft Forum*, Delft, The Netherlands, 19–20 Sept. 2018.
- [109] A. Uzun, M. Y. Hussaini, and C. L. Streett, "Large-Eddy Simulation of a Wing Tip Vortex on Overset Grids", *AIAA Journal*, Vol. **44**, No. 6, 2006, pp. 1229–1242, DOI: [10.2514/1.17999](https://doi.org/10.2514/1.17999).
- [110] G. H. Vatistas, V. Kozel, and W. C. Mih, "A Simpler Model for Concentrated Vortices", *Experiments in Fluids*, Vol. **11**, No. 1, 1991, pp. 73–76, DOI: [10.1007/BF00198434](https://doi.org/10.1007/BF00198434).
- [111] G. H. Vatistas, G. D. Panagiotakakos, and F. I. Manikis, "Extension of the n-Vortex Model to Approximate the Effects of Turbulence", *Journal of Aircraft*, Vol. **52**, No. 15, 2015, pp. 230–243, DOI: [10.2514/1.C033238](https://doi.org/10.2514/1.C033238).
- [112] M. R. Visbal, "Onset of Vortex Breakdown above a Pitching Delta Wing", *AIAA Journal*, Vol. **32**, No. 8, 1994, pp. 1568–1575, DOI: [10.2514/3.12145](https://doi.org/10.2514/3.12145).
- [113] A. Vuillet, M. Allongue, J. J. Philippe, and A. Desopper, "Performance and Aerodynamic Development of the Super Puma MK II Main Rotor with New SPP8 Blade Tip Design", *15th European Rotorcraft Forum*, Amsterdam, The Netherlands, 12–15 Sept. 1989.
- [114] B. G. van der Wall, *Grundlagen der Hubschrauber-Aerodynamik, [Engl: Basics of Helicopter Aerodynamics]*, Springer Vieweg, Berlin, Heidelberg, 2015.

- [115] K. Weinman, "Vortical Correction Modeling in the DLR TAU Code", in: *New Results in Numerical and Experimental Fluid Mechanics VIII*, Notes on Numerical Fluid Mechanics and Multidisciplinary Design 121, Springer-Verlag Berlin Heidelberg, 2013, pp. 439–446, DOI: [10.1007/978-3-642-35680-3_52](https://doi.org/10.1007/978-3-642-35680-3_52).
- [116] D. C. Wilcox, "Reassessment of the Scale-Determining Equation for Advanced Turbulence Models", *AIAA Journal*, Vol. **26**, No. 11, Nov. 1988, pp. 1299–1310, DOI: [10.2514/3.10041](https://doi.org/10.2514/3.10041).
- [117] C. C. Wolf, J. N. Braukmann, W. Stauber, T. Schwermer, and M. Raffel, "The Tip Vortex System of a Four-Bladed Rotor in Dynamic Stall Conditions", *Journal of the American Helicopter Society*, Vol. **64**, No. 2, 2019, pp. 1–14, DOI: [10.4050/JAHS.64.022005](https://doi.org/10.4050/JAHS.64.022005).
- [118] C. C. Wolf, C. B. Merz, K. Richter, and M. Raffel, "Tip-Vortex Dynamics of a Pitching Rotor Blade-Tip Model", *AIAA Journal*, Vol. **54**, No. 10, 2016, pp. 2947–2960, DOI: [10.2514/1.J054656](https://doi.org/10.2514/1.J054656).
- [119] G. K. Yamauchi, A. J. Wadcock, W. Johnson, and M. Ramasamy, "Wind Tunnel Measurements of Full-Scale UH-60A Rotor Tip Vortices", *AHS 68th Annual Forum*, Fort Worth, TX, 1–3 May 2012.
- [120] A. Zanotti and G. Gibertini, "Experimental Investigation of the Dynamic Stall Phenomenon on a NACA 23012 Oscillating Airfoil", *Journal of Aerospace Engineering*, Vol. **227**, No. 9, 2012, pp. 1375–1388, DOI: [10.1177/0954410012454100](https://doi.org/10.1177/0954410012454100).

Curriculum Vitae

Andreas Thabo Goerttler

born on 25th of August 1989 in Heidelberg

andreas.goerttler@dlr.de

Work experience

since 04/2016	German Aerospace Center (DLR), Göttingen <i>Research scientist</i>
10/2015 - 03/2016	German Aerospace Center (DLR), Braunschweig <i>Research stay</i>
07/2015 - 09/2015	German Aerospace Center (DLR), Göttingen <i>Research stay</i>
11/2014 - 04/2015	German Aerospace Center (DLR), Göttingen <i>Master thesis</i>
10/2012 - 02/2013	University of Stuttgart <i>Bachelor thesis</i>

Education

04/2016 - 02/2020	Dissertation at Gottfried Wilhelm Leibniz University Hannover: "Numerical Investigations of the Blade-Tip Vortex of a Rotor with Axial Inflow"
04/2013 - 04/2015	M. Sc. in Aerospace Engineering, University of Stuttgart
08/2013 - 01/2014	Study visit at KTH Royal Institute of Technology, Stockholm
10/2009 - 03/2013	B. Sc. in Aerospace Engineering, University of Stuttgart